TECHNISCHE UNIVERSITÄT WIEN
Vienna University of Technology

Master Thesis

Thermo-mechanical analysis of plasma-based additive manufacturing of Ti-6Al-4V components using Simufact Welding 8.0

Carried out for the purpose of obtaining the degree of Master of Science, submitted at Vienna University of Technology, Faculty of Mechanical and Industrial Engineering, by

Martin Bielik, BSc

Mat.Nr.: 01026611

under the supervision of

Univ.Prof. Dipl.-Ing. Dr.techn. Ernst Kozeschnik

Institute of Material Science and Technology

Vienna, June 2020

Affidavit

I declare in lieu of oath, that I wrote this thesis and performed the associated research myself, using only literature cited in this volume. If text passages from sources are used literally, they are marked as such.

I confirm that this work is original and has not been submitted elsewhere for any examination, nor is it currently under consideration for a thesis elsewhere.

City and Date		Signature

Acknowledgements

First of all, I would like to express my gratitude to my beloved family, without whose support I would not be where I am today. Their never ceasing encouragement and patience are a permanent foundation and source of motivation.

A big thank you goes to RHP-Technology, especially to the CEOs Dr. Erich Neubauer und DI Michael Kitzmantel who gave me the opportunity to write this thesis using current technology and to gain hands-on experience with additive manufacturing. Moreover, I would like to thank my colleagues John, Enrique, Peter, Richard and Johannes who were always there for a thorough discussion and philosophising about new ideas.

I would like to especially thank my supervisor Prof. Ernst Kozeschnik for showing interest in establishing a collaboration between RHP-Technology and Vienna University of Technology which enabled me to pursue the purpose of my thesis and for his excellent guidance. I am very grateful to Ms Edith Asiemo and Ing. Christian Zaruba for helping me with my metallographic examinations and DI Michael Nirtl for performing surface scans on my deposited walls.

Lastly, I want to thank Dr. Ingo Neubauer from Simufact Engineering for enabling me to use Simufact Welding 8.0 and for providing support for the duration of the work.

Abstract

Additive manufacturing is one of the most innovative and revolutionary manufacturing methods. The ability to simulate the thermo-elastic-plastic response of additively manufactured components offers tremendous utility for gaining deeper understanding of the process, while also having significant practical application. This study examines the temperature, distortion and residual stress fields occurring during plasma metal deposition (PMD) of multi-layer Ti-6Al-4V single wall structures using the finite element software Simufact Welding 8.0. The temperature distribution and its gradients are determined by using the Goldak double ellipsoid heat source model. On this basis, coupled thermo-elastic-plastic structural welding simulations are performed. For process mapping, the significance to measure key characteristics for the calibration of the heat source is presented and seen as critical for the quality of the models. Accordingly, the results achieved are used to elaborate an optimal building and clamping strategy for an aerospace bracket to demonstrate the practicability of numerical simulations on a potentially industrial scale.

Kurzfassung

Additive Fertigungsverfahren unterscheiden sich von den traditionellen formenden und subtraktiven Produktionsparadigmen und stellen innovative Fertigungsmethoden dar. Additive Fertigungsverfahren erzeugen die Geometrie auf Basis von digitalen 3D-Konstruktionsdaten durch Hinzufügen, Auftragen und Ablagern von Material entlang bestimmter Bahnen. Die Möglichkeit das thermoelastische-plastische Verhalten von additiv hergestellten Komponenten zu simulieren, bietet einen enormen Nutzen für ein tieferes Verständnis des Prozesses und hat gleichzeitig eine bedeutende praktische Anwendung. In dieser Arbeit werden Temperatur-, Verzerrungs- und Eigenspannungsfelder untersucht, die während der Plasma-Metallabscheidung (PMD) von mehrschichtigen Ti-6Al-4V Komponenten auftreten. Die Modellierung und Berechnung der numerischen Modelle erfolgt in Simufact Welding 8.0. Die Schweißstruktursimulationen verwenden die Finite-Elemente-Methode. Dabei werden die auftretende Temperaturverteilung und deren Gradienten unter Verwendung des doppelellipsoid Wärmequellenmodells nach Goldak berechnet und gekoppelte thermoelastisch-plastische Schweißstruktursimulationen durchgeführt. Für die Prozessabbildung wird die Bedeutung der Messung von Schlüsseleigenschaften für die Kalibrierung der Wärmequellen hervorgehoben und als entscheidend für die Qualität der Modelle angesehen. Die Simulationen sollen helfen optimale Bau- und Einspannstrategien zu finden, um die Praktikabilität der numerischen Simulationen im potentiell industriellen Maßstab zu demonstrieren.

Table of Contents

List of Abbreviations

ALM	Additive Layer Manufacturing
AM	Additive Manufacturing
bcc	body centred cubic
CAD	Computer Aided Design
CMM	Coordinate Measuring Machine
CSA	Cross-sectional area
DDM	Domain Decomposition Method
DED	Direct Energy Deposition
EBF	Electron Beam Fusion
EBM	Electron Beam Melting
EMD	Electron Metal Deposition
FEA	Finite Element Analysis
FEM	Finite Element Method
FZ	Fusion Zone
HAZ	Heat Affected Zone
hcp	hexagonal close packed
LAM	Laser Additive Manufacturing
LENS	Laser Engineered Net Shaping
LMD	Laser Metal Deposition
MIG	Metal Inert Gas (Welding)
MAPE	Mean Absolute Percentage Error
PAW	Plasma Arc Welding
PDE	Partial Differential Equations
PMD	Plasma Metal Deposition
PH	Preheating
RHP	RHP-Technology GmbH
SB	Single Bead
SLM	Selective Laser Melting
SLS	Selective Laser Sintering
SMP	Shared Memory Parallelisation
STL	Surface Tessellation Language
TIG	Tungsten Inert Gas (Welding)
TS	Travel Speed
WAAM	Wire Arc Additive Manufacturing
WEDM	Wire Electric Discharge Machining
WFS	Wire Feed Speed
WLAM	Wire Laser Additive Manufacturing

1 Introduction

Wire arc additive manufacturing (WAAM) is a novel manufacturing technology that permits high deposition rates and enables the production of large near net shape components at low process costs. RHP-Technology has developed a method called Plasma Metal Deposition (PMD®) that uses a plasma transferred arc energy source in combination with wire feeding or blown powder to fabricate 3D parts (see Figure 1).
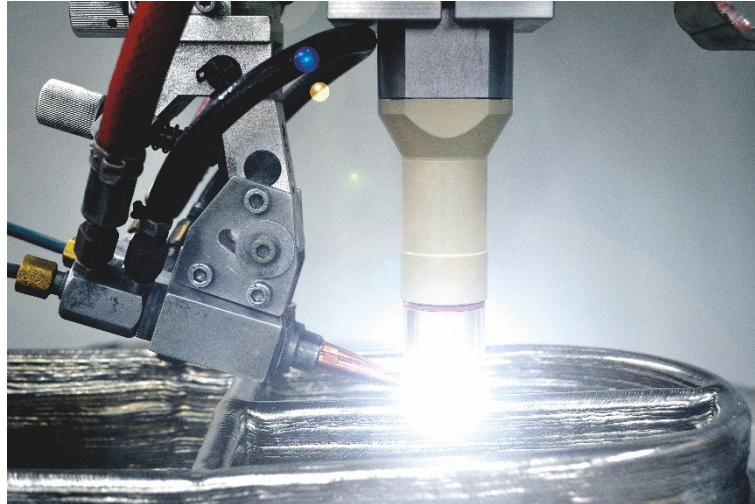
Figure 1: Plasma torch and wire feeder at RHP-Technology

The system at RHP has a building platform of 1.5x1.8 m and allows the manufacturing of large metallic structures made from titanium alloys, steels, aluminum alloys, nickel-based super alloys, and special materials such as Invar. Additionally, composite materials (consisting of a metallic matrix reinforced with ceramic particles) as well as multi-materials have been successfully deposited [1], [2]. Figure 2 shows a mirror support structure made from a titanium alloy using the PMD process. In this picture, the potential of this technology becomes evident - the production of large weld-metal volumes, geometric flexibility, reduction of scrap material and, thus, reduction of production costs.

Figure 2: Mirror support structure for the ESA Athena project

WAAM is becoming increasingly industrialised, with growth in both numbers of end users and equipment suppliers. The aerospace industry, as an early adopter of WAAM, has recognized the potential for the production of large titanium alloy components previously forged and machined. For example, WAAM parts produced by Norsk Titanium, the company providing Rapid Plasma D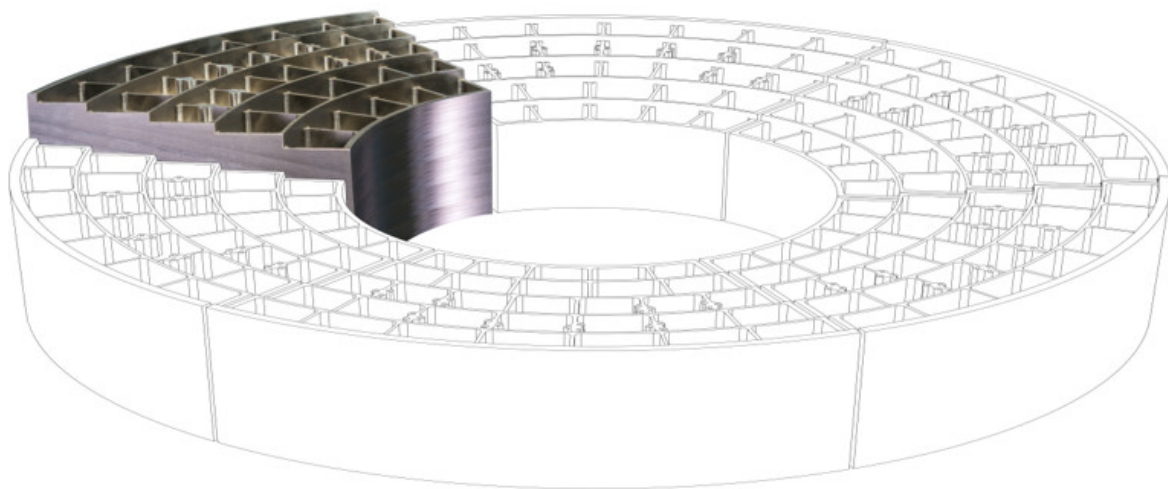eposition (RPD) additive manufacturing, achieved US Federal Aviation Authority certification for production of WAAM parts for the Boeing 787 Dreamliner in 2015 [3].

Figure 3: WAAM part for the Boeing 787 Dreamliner made by Norsk Titanium [3]

Titanium combines high strength with low density and excellent corrosion resistance. This usually favourable combination of characteristics makes titanium, despite its high cost, attractive for a variety of applications. Titanium and its alloys can be found in aircraft parts, jet engines, medical devices, high performance engines, chemical apparatus engineering and electroplating technology. Although titanium has the highest strength to density ratio, compared to other structural metallic materials such as iron, nickel or aluminium, it is only used for certain niche applications [4]. The titanium alloy investigated in the present study is Ti-6Al-4V, the most widely used titanium alloy. More than 50 % of all titanium tonnage worldwide are of this composition [5]. It is used in aerospace, automotive and marine applications, and in medical devices owing it to its high specific strength, high fatigue strength, low modulus of elasticity, low density, stability up to 400 °C, high hardness and good corrosion resistance [4]–[7]. Due to the high costs and waste related to the conventional manufacturing processes, AM represents an attractive method for the fabrication of titanium components. Manufacturing Ti-6Al-4V near-net-shape components with additive manufacturing offers a great potential for components that are machined from costly wrought materials at a low buy-to-fly ratio.

Additive manufacturing is one of the most innovative and revolutionary manufacturing methods. It stands for rapid, innovative change and high dynamics in production technology and the associated value chain. Numerical simulations are an established method for the virtual process simulation to meet the continuously increasing demands on the economic efficiency of production processes. Complex problems can be solved virtually without expensive and time-consuming experiments. Plasma metal deposition as a technology utilised for the production of large-scale components uses a plasma arc to fuse metal powders or wire into complex and high-strength components. A characteristic feature of welding is the localised heat input of a moving heat source with high energy density, which leads to the formation of transient temperature fields in the component. Due to the resulting thermal expansion, an inhomogeneous temperature distribution can locally lead to different mechanical distortion and

stress fields. At high temperatures, these distortion and stress fields can lead to both elastic and plastic deformations. If the component is cooled down to room temperature, the reduction of the distortion and stress fields becomes noticeable when the balance of forces is disturbed. This disturbed equilibrium of forces can lead to distortion or shrinkage in the component at room temperature and to mechanical residual stresses in the component. Thermo-mechanical welding simulations allow the prediction of welding distortions and residual stresses and can thus help to meet product requirements. The computing power available today allows the numerical calculation of elastic-plastic behaviour of materials in the course of structural welding simulations on an industrial scale. Structural welding simulations calculate the effects of heat input of the welding process from a mathematical description of the heat flux during welding. The heat input is simulated via an equivalent heat source moving in the direction of welding. Whereas good, capable simulation tools already exist for the widely used powder bed processes, numerical simulation packages for DED-specific applications are still in their early stage. However, to fully exploit the potential of DED, the use of innovative software solutions is essential. Simufact Welding 8.0 by MSC Software is a powerful simulation package enabling the simulation of the PMD process. Simufact is a FEA based simulation solution for metal forming, welding and heat treatment. With the ability to perform both welding and structural analysis, Simufact Welding can help to optimise the manufacturing process, reduce costs and the time-to-market, while improving product quality.

2 Objectives

The aim of this work is the numerical prediction of residual stresses and distortion of large scale Ti-6Al-4V plasma metal deposited components based on the results of thermo-mechanical welding simulations. Therefore, single wall demonstrators are manufactured at RHP-Technology with defined pre-, online-, and post-processing strategies. Distortion and temperature distribution of the single wall structures are measured experimentally and compared to numerically obtained results by implementing the PMD process into Simufact Welding 8.0. Consequently, one requirement is the accurate prediction of experimental temperature profiles and distortion data. Therefore, a calibration of a mathematical heat source model is conducted to represent the real process within a finite element framework. Additionally, different building strategies and parameters are then compared numerically in order to assess the impact of these aspects on the distortion and residual stress fields of the additive manufactured components. The numerical simulations shall help to develop pre-process, online-process and post-process strategies for the PMD process. The research questions are related to the project map shown in Figure 4.
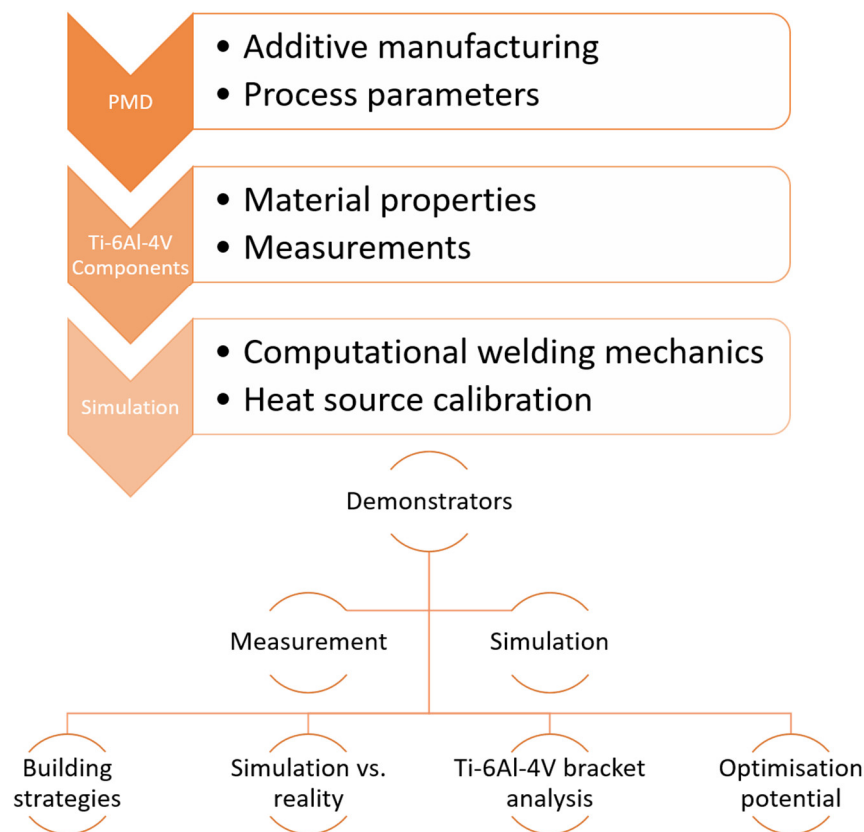
Figure 4: Project map with areas that are investigated

This work aims at giving insight to RHP-Technology into process related phenomena, such as distortion and the build-up of residual stresses, and providing mitigation and optimisation strategies by assessing these phenomena with computer aided calculations based on finite element analysis.

The tasks can be defined as the following:

- Production of demonstrators at RHP-Technology.
- Experimental validation of distortion and temperature distributions.
- Implementation of the PMD process into Simufact Welding 8.0.
- Identification of correlations between building strategies and building parameters and resulting residual stress and distortion fields.
- Numerical study of a representative component with a more complex geometry.

3 Literature review

In this literature review sufficient background information to all the areas involved in the thesis will be provided and the state of the art of each of them will be presented. Starting with direct energy deposition as metal additive manufacturing technology, aspects of additive manufactured Ti-6Al-4V are introduced. Thereafter, residual stresses will be discussed in terms of cause, measurement methods and mitigation strategies with specific attention to additive manufactured parts. Finally, computational welding mechanics within the finite element framework will be reviewed. Information on titanium and its alloys, its material properties, Ti-6Al-4V and its various microstructures and processing routes to achieve them can be found in Appendix A - Titanium and its alloys.

3.1 Plasma metal deposition

Additive manufacturing, as opposed to the subtractive approach, refers to a process by which digital 3D design data are used to build up a component by depositing material layer by layer, i.e. the three-dimensional shape is created by stacking two-dimensional layers. A range of different materials, including metals, but also plastics and ceramics can be used. The term "3D printing" is often used as a synonym for additive manufacturing. According to Knezovic and Topic [8] three constituents are essential for AM, namely a motion system, feedstock material and an energy (heat) source. A combination of different heat sources and raw material forms has led to a creation of a wide spectrum of AM techniques. Depending on application and material, metal additive manufacturing utilizes several methods, such as powder bed processes (ALM, SLM, SLS, EBM), blown powder (Laser Cladding, LMD, LENS), binder jetting and wire based direct energy deposition (EBF, WLAM, WAAM). The combination of an arc welding power source and metal wire as feedstock is referred to as wire and arc additive manufactured (WAAM) [9]. Although investigated since the 1990s, it is a novel manufacturing technology for industrial applications by utilising a plasma or electric arc as heat source and a metal wire as feedstock [10]. Motion can be either provided by robotic systems or computer numerical controlled gantries to follow the paths of the components' geometry. Common technologies currently used in WAAM are metal inert gas welding (MIG), tungsten inert gas (TIG) welding and plasma arc welding (PAW) [11]. In this study, plasma metal deposition is utilised as additive manufacturing technology, in which plasma welding and wire feeding are combined, as schematically shown in Figure 5.
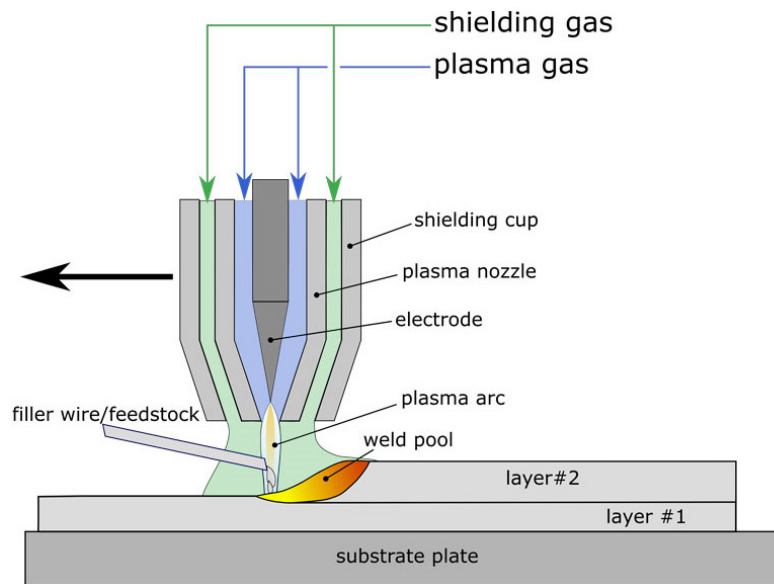
Figure 5: Schematic view of wire and arc additive manufacturing utilising a plasma torch [12]

The process is characterised by a high density plasma arc obtained by the ionisation of an inert plasma gas (usually argon or helium) passing through the electric arc formed between a non-consumable tungsten electrode (cathode) and a constricting water-cooled copper nozzle (anode). This non-transferred arc (pilot arc) is employed to initiate the welding process by forming a pathway of low electrical resistance between the tungsten electrode and the workpiece. When power is added, the main arc, which burns between the electrode and the workpiece (transferred arc) is ignited and provides the energy needed to melt the base material and filler metal. By moving the plasma torch along certain paths during the process and by over-welding of already existing layers, the three-dimensional, near-net-shape component is created. Figure 6 shows the functional principle of the PMD process. The necessary paths can be directly calculated from a 3D CAD model of the component. The feedstock material is fed at a controlled rate to the plasma arc and is melted onto the substrate or previously deposited layers creating a layer of 3D printed structure. In practice, the parameters which control the quality of the weld are the rate at which the feedstock material is added, gas flow rates (shielding gas, pilot gas), the weld current, the nozzle to workpiece distance and the welding speed. A final machining process is needed to achieve a desirable surface finish and dimensional accuracy.
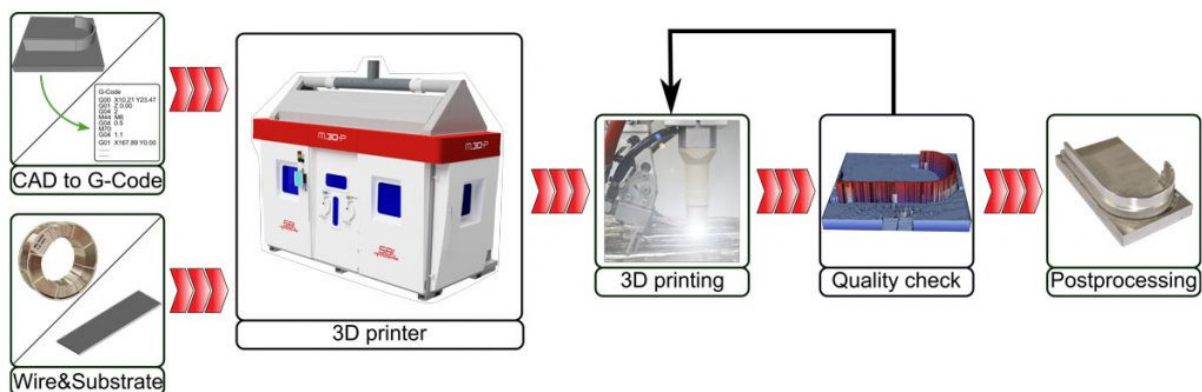

Figure 6: Functional principle of the PMD process [12]

Wire and arc additive manufacturing represents an alternative to conventional, subtractive manufacturing processes, especially in the aerospace industry. Other areas of application are

toolmaking, automotive, oil & gas, shipbuilding, and mechanical engineering. Additive manufacturing is an attractive method for the fabrication of T-6Al-4V parts. The PMD process allows the production of large, fully dense and high quality near-net shape Ti-6Al-4V components with different geometries, as can be seen in Figure 7.
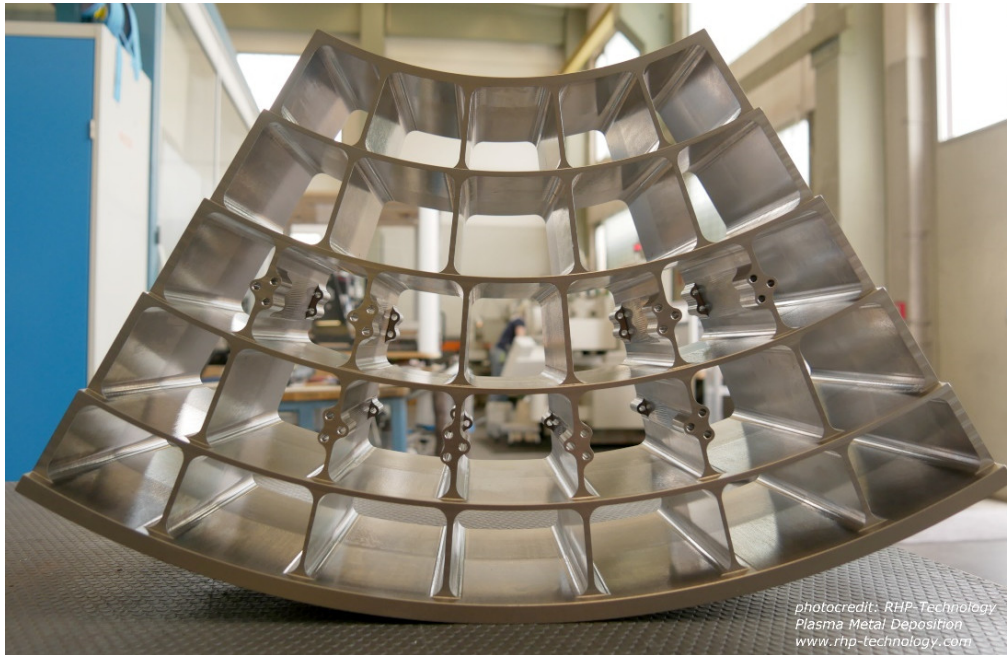

Figure 7: Additively manufactured mirror support structure produced by RHP-Technology

Plasma metal deposition can be related to a multi-layer welding process. Ti-6Al-4V is a weakly beta-stabilised alloy and is considered highly weldable compared to other structural titanium alloys. Weldable, by definition, is used if the weld of an alloy is sound and free of defects [4, p. 102]. In general, as the maximum strength of titanium alloys increases, they become more difficult to weld, due to the presence of low melting eutectics which cause cracking [4, p. 104]. Ti-6Al-4V exhibits a high resistance to solidification- and liquidation-related cracking due to its single-phase mode of solidification. Although cracking and defects, such as the formation of porosity, may occur in Ti-6Al-4V weldments, it can be most often related to the welding process. According to ASM's materials properties handbook [5], the good weldability of Ti-6Al-4V can, firstly, be attributed to the formation of a softer and more ductile α' martensite than more heavily β-stabilised α+β alloys (strongly β-stabilised alloys are embrittled by welding), and, secondly, relatively low hardenability which allows the formation of higher proportions of a more desirable Widmanstätten microstructure. The weldment properties of Ti-6Al-4V in AM depend on the energy input of the welding process, the structural characteristics of each weld region, multiple thermal cycles imposed during welding, the heat flow during solidification, heat treatments or mechanical residual stress mitigation techniques [5].

3.2   Residual stress & distortion

Withers and Bhadeshia [13] identified residual stresses as those "which are not necessary to maintain equilibrium between the body and its surroundings". In other words, if stresses are retained in a body without being subject to external forces, they are referred to as residual stresses. The authors [13] categorised residual stresses by their cause, by their scale, or by their measurement method. In fact, residual stresses result from misfits affecting different regions of a material, component, or assembly (Figure 8). The most common origins of such misfits are non-uniform plastic flow, steep thermal gradients, as experienced during welding,

phase transformations, or even changes in material bonds due to different coefficients of thermal expansion [14]. Thus, residual stresses can arise from mechanical, thermal, plastic, or transformation related origins.
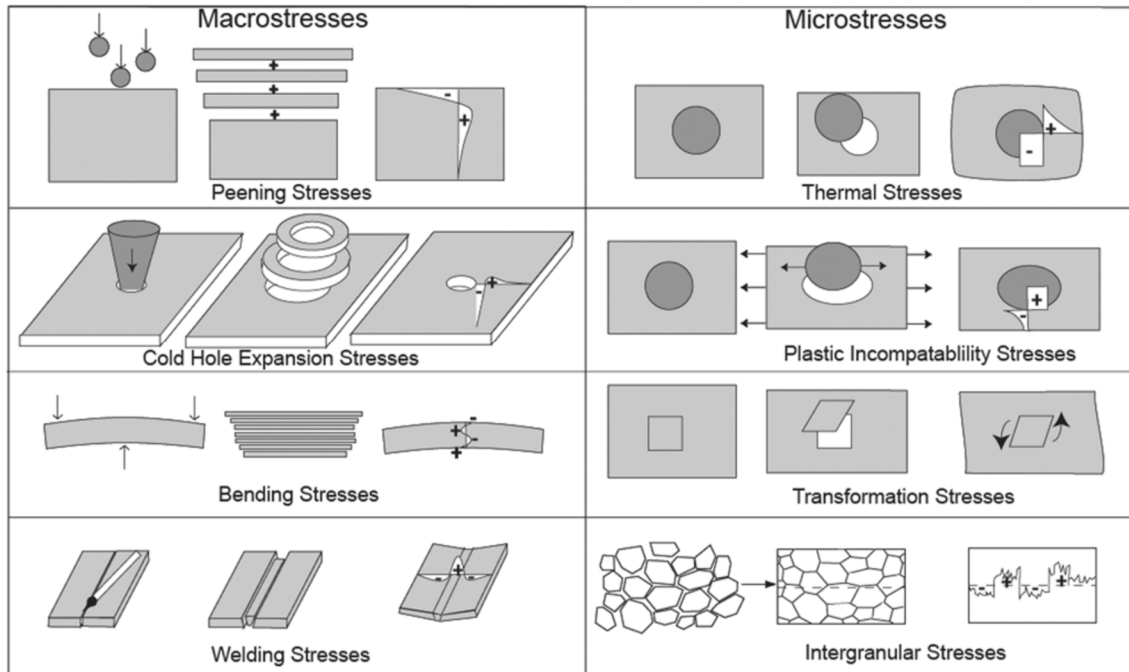

Figure 8: Illustration of different macro and micro residual stresses [14]

Additionally, Withers and Bhadeshia [13] classified different types of residual stresses according to their characteristic length scale l_0 over which they self-equilibrate. Macrostresses varying over large distances are defined as *type I*, while residual stresses varying over the grain size are defined as *type II* (intergranular stresses). Finally, stresses varying over the atomic scale are defined as *type III*. It should be noted that no measurement method is capable of measuring all three types of residual stresses [13]. Hereby, the characteristic length scale l_0 is an important entity for the selection of an appropriate technique.

Measurement techniques can be divided into destructive and non-destructive methods. Destructive methods rely on stress relaxation at a newly formed surface by introducing a cut into the object. The original stress field or eigenstrain distribution is then reconstructed from the observed distortion. Crucial to this assumption is that the relaxation is entirely elastically and does not introduce any further misfits into the specimen [14]. Destructive measurement methods are:

■ Sectioning
■ Hole drilling
■ Slotting methods
■ Contour method

The most important non-destructive method is diffraction, where changes in the interplanar lattice spacing can be used with Bragg's law to detect elastic strain. Here, the crystalline lattice itself is used as an atomic strain gauge. Three main types of radiation are available with wavelengths suitable for measuring atomic lattice spacing:

■ Electron diffraction
■ X-ray diffraction
■ Neutron diffraction

Other measurement techniques rely on different stress-related properties, such as magnetic and electric techniques, thermoelastic methods, or photo-elastic methods [13].

3.2.1 Weld induced residual stresses

A characteristic feature of welding is the localised heat input of a moving heat source with high energy density which leads to the formation of transient temperature fields in the component. Thermal gradients caused by thermal excursions lead to locally different distortion and stress fields. Over a wide range of temperatures, from room temperature to melting temperature, thermal welding stresses are produced by complex mechanisms, involving plastic deformation, phase transformations and the effects of melting and solidification [15]. The temperature excursions and the formation of residual stresses during welding are illustrated in Figure 9. The temperature excursions themselves increase with increasing energy input of the energy source and with decreasing thermal conductivity of the material. During the welding process the welding area is locally heated and melted. Consequently, the heat affected zones want to expand, but the thermal expansion is restrained by the surrounding "cold" base material resulting in compressive stresses near the heat source. These compressive stresses are balanced with tensile stresses in the surrounding material to maintain force equilibrium. The thermal stresses partially exceed the yield limit which decreases with increasing temperature, causing a locally limited plastic flow that relieves a part of the stresses. The maximum magnitude of the compressive stresses is determined by the yield limit of the material at corresponding temperatures. If the component is cooling down to room temperature, the weld metal and base material regions try to shrink which causes tensile stresses in regions close to the weld. Phase transformations can also generate residual stresses which result from volume changes during solidification of the weld pool, as well as from microstructural changes. In general, the microstructure of the base material has been optimised by careful processing, whereas the microstructure in the weld and heat affected zone might be sub-optimal. These aspects can be a potential failure mode of welded structures [14]. The remaining residual stress state in the component after welding is characterised by tensile stresses in regions near the weld and compressive stresses in the surrounding area.
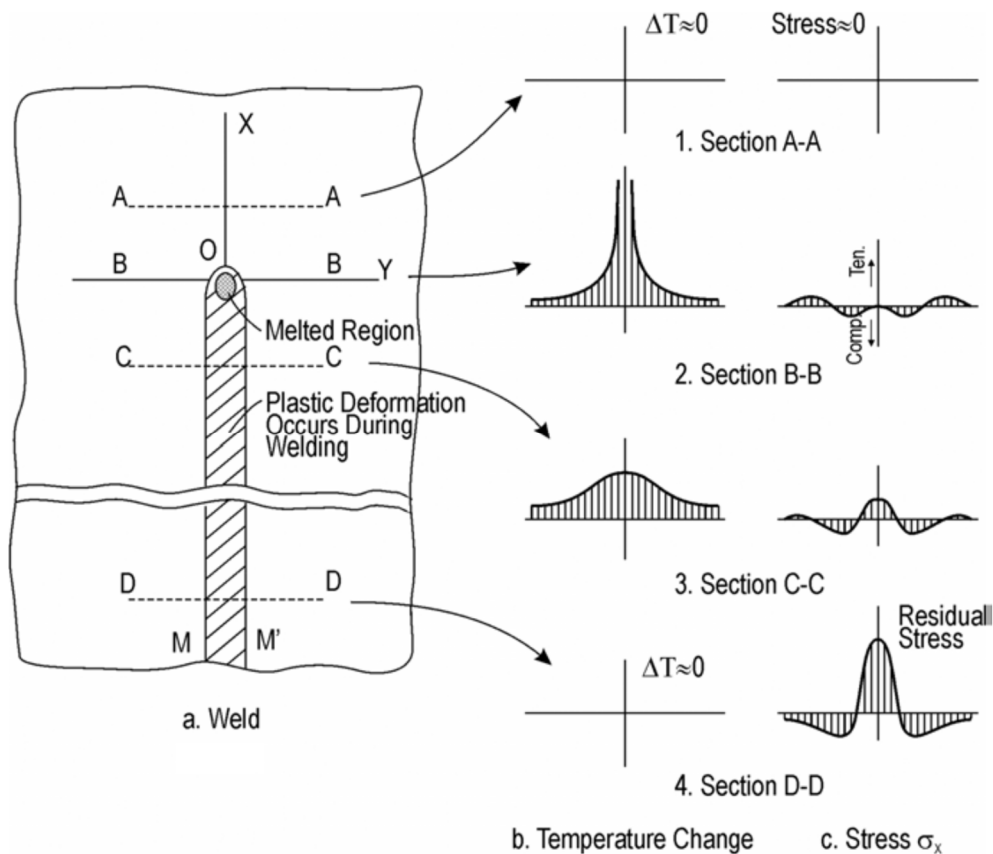
Figure 9: Formation of residual stresses in the workpiece during welding [15]

The exact orientation and magnitude depend on the direction of the steepest thermal gradients and mechanical restraints applied to the component. If materials are heated uniformly, they expand during heating and shrink after cooling back to their original shape without the formation of tensions or deformations. If one of these mechanisms is restrained, shape changes and residual stresses will arise. Residual welding stresses cause temporary or permanent changes in the weld shape, known as shrinkage, distortion, or warping. Stress and deformation act largely opposite. Figure 10 illustrates the interdependence between distortion and residual stress as a function of the degree of restraint. High stresses occur when shape change is hindered, lower stresses occur when shape change is not hindered [16, p. 11].

Figure 10: Counteraction of residual stress and distortion adopted from [17]

Every measure reducing distortion, e.g. a thorough fixation of a component, promotes residual stresses and vice versa. In fact, a welded structure can neither be produced free of residual stresses nor free of distortion.

In practice, however, the task is to simultaneously achieve high dimensional accuracy and low residual welding stresses. The main goal of calculations made by welding simulations is to predict welding distortion and residual stresses and, consequently elaborate strategies to balance welding induced stresses and distortion.
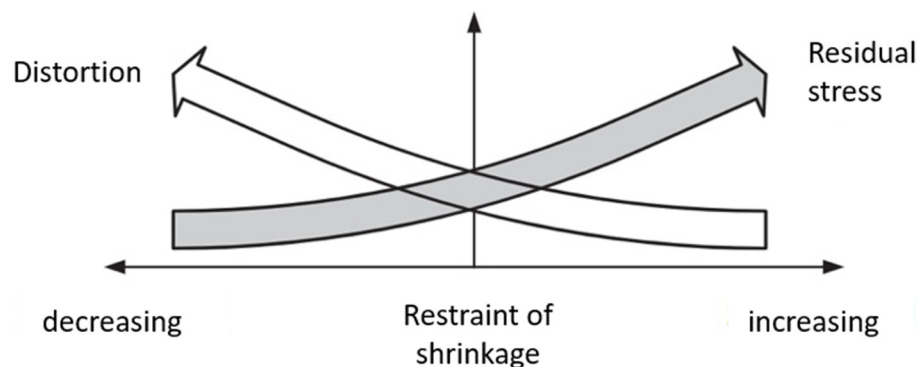
3.2.2 Residual stress of PMD components

PMD components are affected by residual stress and distortion. Residual stresses reduce the mechanical part performance and distortion has a strong impact on achieving required dimensional tolerances. Distortion in AM parts is caused by the build-up of residual stress as a result of the large thermal gradients induced during the repeated melting and solidification of the material. Deformation and residual stresses of WAAM components (unclamped condition after the deposition process) have been studied extensively in [18]–[21] for titanium and steel structures. The longitudinal stresses along the cross section of AMed components, in general, show a substantial level of tensile stresses concentrated in the area adjacent to the interface between the baseplate and the deposited layers. These longitudinal tensile stresses decrease towards the top of the wall becoming compressive in the top region. Transverse and normal stresses show a similar variation at the baseplate-wall-interface, but are considerably smaller than the longitudinal stresses. Figure 11 shows representative principal stresses measured with neutron diffraction of a Ti-6Al-4V wall structure. Similar results were also obtained in other studies.
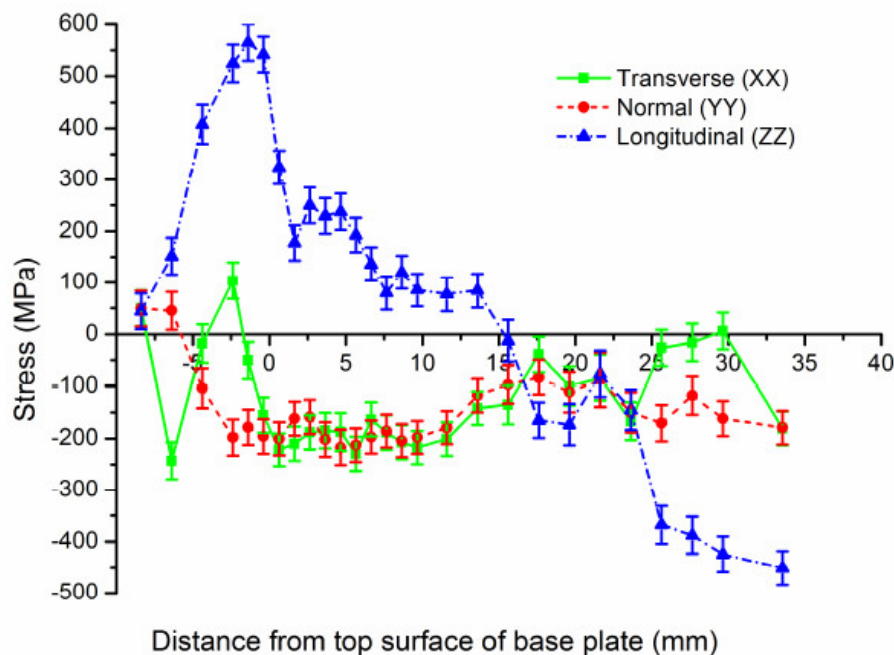
Figure 11: Residual stresses at the weld centreline over the height of the wall [20]

Hoye et al. [20] understood the multi-layer welding process to influence residual stresses in two ways: firstly, stress relief due to local annealing effects, and, secondly, the deposited wall functioning as rib stiffening structure. Previously deposited layers are subsequently remelted and reheated during deposition of a new layer. Thus, local annealing effects can relief stresses generated from preceding welds. The deposited wall constrains the base plate in the longitudinal direction, since it is acting as an integrated rib stiffening structure as the WAAM process progresses. However, the large amount of heat input on the upper built layers gives rise to further stresses. During both stages of solidification and cooling, the plastic strains caused by the thermal expansion and by the constraints of clamping devices lead to residual

stresses. Once the AM process is completed, the clamps are released and the workpiece reaches its final shape. The component is allowed to distort under the influence of residual stresses. Colegrove et al. [19] described bending distortion of WAAM parts as an interplay of tensile and compressive stresses in the deposit and baseplate. During deposition, clamps restrain the substrate and uniform tensile stresses are produced in the wall during deposition. The balancing compressive stresses are contained in the baseplate. The necessary bending moment to keep the substrate flat is provided by the clamps. Upon releasing the clamps, stress relaxation occurs and inherent plastic strains cause the specimen to bend upwards and the net bending moment across the section reduces to zero. The resulting distortion changes the stress field by reducing the tensile stresses in the top of the wall and by increasing tensile stresses in the bottom of the baseplate. The redistribution of stresses and resulting distortion due to unclamping is schematically illustrated in Figure 12.
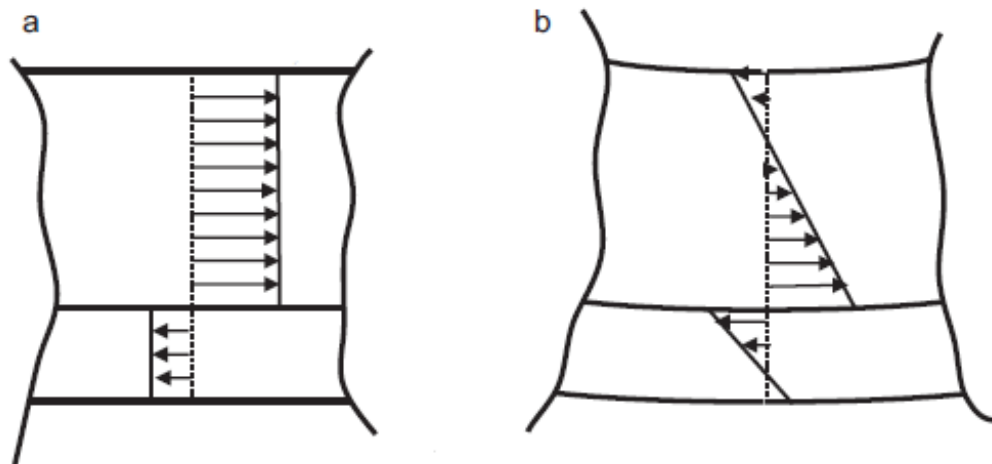

Figure 12: Schematic evolution of stresses in an AMed wall: (a) after deposition while clamps are still applied, (b) after unclamping [19]

Residual stress is affecting several failure mechanisms including fracture and fatigue properties, stress corrosion cracking and distortion [22]. Addressing contemporary approaches to reduce residual stresses, thermal and mechanical treatments are available. Thermal treatments are a common way to relieve residual stresses and can be separated into three categories, namely preheating, online control of heat input during welding, and post-weld heat treatments. Mechanical treatments usually aim at inducing new compressive residual stresses to balance the detrimental effects of existing tensile residual stresses. Mechanical treatments for additive manufactured parts can be categorised into two different processes, such as peening and rolling. In-situ and post-weld rolling have been extensively studied in recent years for the reduction of residual stresses of additive manufactured components [19], [21].

3.3 Computational welding mechanics

Computer simulations are a scientific tool to model physical systems based on mathematical models. The combination of sophisticated software and high-performance computing enables engineers and scientists to solve complex problems virtually without expensive and time-consuming experiments. One of these methods is the so-called finite element analysis (FEA) which allows the simulation of any given physical phenomenon, such as fluid behaviour, thermal transport, wave propagation, structural mechanics, and other specialised applications, using the numerical technique called finite element method (FEM). Most of these processes are described by using partial differential equations (PDEs). One of the most powerful

numerical techniques for obtaining solutions of PDEs is the finite element method. The simulation of the PMD process, from a modelling point of view, can be seen as a multi-pass, multi-layer welding process. Numerical models must take several physical aspects into account, such as heat and mass transfer, phase changes, fluidic dynamics of the molten pool, the evolution of material properties, residual stress, and distortion throughout the entire build time. Additionally, the models must span different length scales, resolving the molten pool, the weld chamber dimensions, and hundreds of meters of heat source trajectories and, of course, different time scales. Depending on the travel speed and wire feed speed, the interaction time of the heat source with the feedstock material is many orders of magnitude smaller than the build time which ranges from several hours to several days, depending on the size of the component. Thus, numerical welding simulations must cover multi-scale and multi-physics processes and solve complex algorithms.

3.3.1 Software vendors

A crucial part of this thesis consisted of screening the market for a suitable software partner for the simulation of a multi-layer welding process. Firstly, existing software solutions are divided into general multi-purpose FEA software and sophisticated welding or AM simulation software. The difference lies in the workflow and in the interpretation of results. General multi-purpose FEA software simulate a generic model of the thermo-mechanical process using a generic heat source, regardless of the welding method. The user has to interpret the results manually according to machine parameters. On the other hand, sophisticated welding or AM software have a predefined graphical interface and workflow according to the process. As such, the user can input actual machine specifications directly and receive the simulation output in a relevant, process-related form. Main simulation attributes that should be considered are:

- Support of direct energy deposition.
- Accuracy and easy interpretation of results.
- Capability of following 3D tool paths and incorporating welding process parameters.
- Capability of implementing time factors in the simulation model (delay time, travel time, cooling time, …)
- Capability of computing large models.
- Meaningful simulation times.
- Easy training and operation, and a user-friendly interface shorten the learning period.

With regard to these aspects, different software providers were screened to evaluate the capabilities of their simulation tools for the numerical implementation of a plasma based WAAM process and are briefly described in the following paragraphs.

ANSYS Additive Suite and Additive Print are present at the market as a stand-alone product. The suite is comprised of Workbench Additive, Additive Science and Additive Print. Additive Print is a practical tool for people who need to build real parts. It can predict the final shape of the printed part, layer-by-layer distortion and stress, optimal support structures, distortion compensated STL files, and potential blade crash. Additive Science is an application for design-stage investigation of materials and optimal machine parameters and for gaining insight into the microscale molten pool phenomena. Finally, Workbench Additive allows the additive process simulation and is specifically designed for this environment. Currently, ANSYS covers only powder bed fusion processes since the demand for WAAM based software solutions has not yet found a great demand on the market. [23]

COMSOL is a multi-physics software capable of coupling several physical phenomena. It is a universally applicable simulation software for modelling designs, devices and processes in all areas of engineering, manufacturing and scientific research. Real systems become multi-physical quite fast. Therefore, the functionality of COMSOL can be extended with add-on modules to simulate electromagnetics, heat transfer, fluid dynamics, structural mechanics and many more. It is capable of very complex simulations covering the physical phenomena of additive manufacturing processes, but the governing equations have to be implemented by the user themselves. [24]

DynaWeld GmbH & Co. KG is a company located in Germany distributing sophisticated solutions for welding, heat treatment and hot forming. Their product portfolio for the simulation of welding processes includes SimWeld and DynaWeld. SimWeld enables the numerical calculation of the bead geometry and temperature field in gas-shielded metal arc welding of aluminium and steel alloys. Obtained results can be further implemented in a structural welding simulation. DynaWeld is a software package for setting up models for welding structure analysis and heat treatment analysis. It simulates distortion, residual stress and local change of material properties for numerous process-types, including arc welding, GMAW, TIG, laser, electron beam, resistance welding and brazing. Multi-pass layer welding is also possible. [25]

ESI SYSWELD offers multiple software packages for virtual manufacturing. Welding and additive manufacturing are also included in their product portfolio, making ESI an interesting partner for the provision of a sophisticated software. ESI Sysweld enables the assessment of chemical, thermal and metallurgical phenomena encountered in the welding heat treatment processes. In the sense of AM, ESI has developed a complete suite of tools for metal additive manufacturing addressing heat source and feed stock interaction to identify manufacturing defects and residual stresses. The solution portfolio for AM is limited to DMLS, SLM, EBM, LENS and EBAM. A WAAM tool is currently being developed. [26]

GeonX released a simulation tool called Virfac (Virtual Factory), enabling engineers to simulate welding, additive manufacturing, machining, heat treatment and damage resistance in various industries. Thus, GeonX offers multiple software packages for virtual manufacturing. Both, LMD and SLM processes can be computed with the AM module. The WAAM process is not included in the product portfolio. [27]

Simufact is a leading FEA based manufacturing process simulation solution for the metalworking industry. It has the ability to simulate the entire manufacturing chain, optimise manufacturing processes, reduce costs and time-to-market, and improve product quality. Two product lines are interesting for the simulation of the WAAM process, namely Simufact Welding and Simufact Additive. Simufact Welding software covers different welding processes and encompasses the modelling of elastic-plastic behaviour of materials and structural welding simulation. Additionally, multi-pass welding processes can be set up in Simufact Welding. Simufact Additive is a process simulation environment for metal additive manufacturing processes, allowing the simulation of both powder bed fusion processes and laser metal deposition. The current release, Simufact Welding 2020, already includes a direct energy deposition tool. [28]

After having assessed the capabilities of the commercially available software packages and considering academic support, **Simufact Welding 8.0** has been chosen to perform the numerical simulations. The simulation of the PMD process is possible in a transient thermo-mechanical analysis. Simufact Additive is using a more simplified approach which is suited only for layer-based AM processes and does not consider individual paths of the heat source. Other software vendors focus on simulating powder bed processes, which means that the

implementation of the PMD process model into already existing tools would require considerable effort.

3.3.2 Computational welding mechanics

Physics-based modelling of the welding process allows to study the impact of welding parameters on the final weld shape, residual stress state and distortion in order to improve welding quality and to save costs. Due to the strong couplings of many physics involved, numerical modelling is quite complex. The physics and mechanics of welding can be separated according to different length- and timescales. Megahed et al. [29] proposed a distinction into micro-, meso-, and macroscale models (Figure 13). Heat source feedstock interaction, heat absorption and phase changes are part of the microscale. The domain is comparable to the size of the molten pool and heat affected zone. Macromodels address molten pool dimensions and the thermal cycle to calculate residual stresses and the final workpiece shape. Numerical models are in the size of the actual component. Clamping conditions and the deposition strategies are applied as boundary conditions. Finally, mesoscale models describe the thermo-mechanical behaviour of the part calculating composition- and temperature-dependent metallurgical properties.
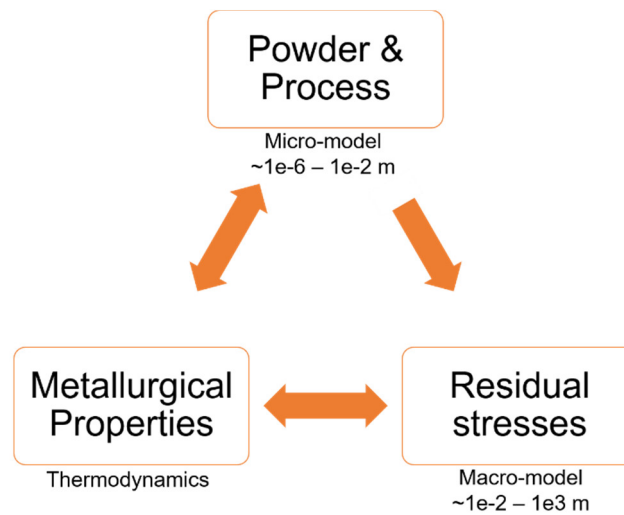

Figure 13: Length scales in AM [29]

3.3.3 Material deposition modelling

Plasma metal deposition can be related to a multi-layer welding process, in which the filler material is melted and deposited layer-by-layer. The deposition of the melted material along the welding path has to be implemented in the physics based finite element framework of the additive manufacturing process. Depending on the finite element activation/deactivation technique, the filler material can be simulated in two ways: the quiet element method or the inactive element method [29], [30]. The quiet element method is based on the initial existence of all elements in the model, i.e. all elements of the mesh defining the baseplate and successive layers to be deposited are included in the initial computational model. These elements are made passive (quiet) by multiplying material properties by scaling factors which do not affect the rest of the model. As material is deposited, the real thermo-physical properties are re-established based on the location of the energy source switching the elements to active. In this thesis, the quiet element method is used. The second approach removes elements representing material to be deposited from the computational analysis up to their activation. According to the metal deposition along the welding path, elements are switched to active and assembled into the model. Thus, only the mesh representing the base material and already

deposited layers are computed and assembled into the global matrix. Michaleris [31] developed a hybrid quiet/inactive element method accelerating computer run times. Hereby, elements corresponding to material deposition are initially inactive and elements of the current deposited layer are switched to quiet. Based on the location of the energy source, quiet elements are switched to active as material is deposited.

3.3.4 Heat source model

Simufact Welding 8.0 is used to analyse the thermo-mechanical performance of the WAAM process on a Ti-6Al-4V multi-layer wall structure. The thermal analysis of the WAAM process involves the solution of a heat transfer problem with a moving heat source. Since 1984, the most widely used model in computational welding mechanics has been the power density distribution function with net weld power and weld pool shape, size and position as a function of time introduced by Goldak et al. [32] for the simulation of welding processes. Within the arc welding module, Simufact Welding 8.0 employs the Goldak double ellipsoid as standard heat source (Figure 14). The moving double ellipsoid model can describe a wide variety of welding techniques, including gas metal arc welding, gas tungsten arc welding, shielded metal arc welding and submerged arc welding [33]. The heat source is a mathematical description of the heat transfer of the arc to the molten pool describing the energy distribution inside the weld pool. The aim is to model the isothermal surface of the real molten pool and the heat flow through this isothermal surface close to reality. Hereby, the effects of the molten pool are considered indirectly.
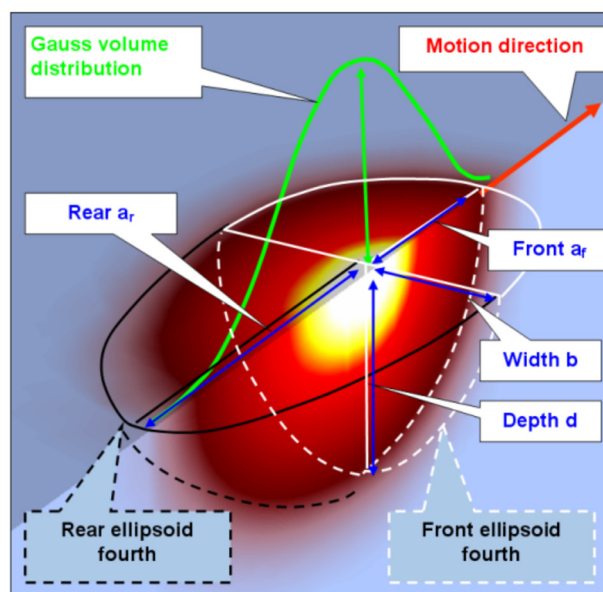
Figure 14: Illustration of Goldak's double ellipsoid heat source model [33]

The Goldak model describes a Gaussian distributed heat generation per unit volume defined in a moving reference frame. A Cartesian coordinate system with local coordinates x, y, z was introduced in the welding point whose x-axis points in the direction of welding and whose z-axis points in the normal direction of the torch. The heat source moves with constant velocity v along the x-axis. Mathematically, two power distribution functions q_f and q_r [W/m³] are defined for the rear and front semi axis in motion direction. The power densities in the region in front of the arc centre and the region behind allow to model asymmetries in the heat distribution of the molten pool [32] given as

$$q(x,y,z,t) = \frac{6\sqrt{3}Q}{\pi\sqrt{\pi}bd} \begin{cases} \frac{f_f}{a_f} \cdot \exp\left[-\frac{3(x-vt)^2}{a_f^2} - \frac{3y^2}{b^2} - \frac{3z^2}{d^2}\right] \, for \, x > vt \\ \frac{f_r}{a_r} \cdot \exp\left[-\frac{3(x-vt)^2}{a_r^2} - \frac{3y^2}{b^2} - \frac{3z^2}{d^2}\right] \, for \, x < vt \, , \end{cases} \tag{3.1}$$

where Q, a_f, a_r, b, d denote the total power [W], the front length [m], the rear length [m], the width [m] and the depth [m] of the ellipsoids. In this model, the fractions f_f and f_r are the portion of the heat deposited in the front and rear ellipsoid, fulfilling the relation $f_f + f_r = 2$. This is done because the temperature gradient in front of the heat source is steeper than in the trailing edge. The heat front scaling factor f_f is determined by imposing an additional constraint that forces continuity of the function q across the $x = vt$ plane at any time t. That is when $x = 0$ [34], [35] resulting in

$$q_f(0,y,z,t) = q_r(0,y,z,t) \, . \tag{3.2}$$

From this condition, another constraint is obtained for f_f and f_r as $f_f/a_f = f_r/a_r$ and the distribution parameters can be expressed in terms of geometric parameters

$$\begin{aligned} f_f &= 2\frac{a_f}{a_f + a_r}, \\ f_r &= 2\frac{a_r}{a_f + a_r}. \end{aligned} \tag{3.3}$$

If not enough experimental data is available, Goldak et al. [32] suggested to set the front scaling factor to $f_f = 0.6$ as default value. The fraction is calculated automatically if the geometrical parameters are known. The heat input during welding can be regarded as a main factor influencing the properties of welds. It influences the time-temperature cycles that take place during welding. For arc welding, the power input Q [J] by the torch is dependent on the current I [A], the voltage U [V] and the efficiency η [-] as follows

$$Q = \eta\, U\, I \, . \tag{3.4}$$

Inputs for Goldak's double ellipsoid heat source model include the calibration of six parameters a_f, a_r, b, d, M and η to calibrate the heat source model. The front length a_f, the rear length a_r, the width b and the depth d are geometrical parameters defining the fusion and heat affected zone. These parameters can be obtained from micro-graphs of cross-sections of the weld pool shape or in-situ measurements of the weld pool. The Gaussian parameter M defines the width of the Gaussian bell curve and therefore the energy per area. The thermal efficiency η links the gross heat input with the net heat input of the welding process. The calibration of the double-ellipsoidal heat source model requires adequately fitting numerical results to experimental data. Therefore, measurements errors can be inherent to Goldak's heat source model.

3.3.5 Governing equations

A thermo-mechanical FE model is developed to determine deformations and residual stress in large-scale Ti-6Al-4V components that are caused by the plasma metal deposition process. Therefore, FE simulations are carried out to calculate temperature fields and, based on the thermal analysis, deformations and residual stresses are determined in a subsequent thermal

elastic-plastic mechanical calculation step. A welding simulation is generally performed as a sequential simulation of the transient temperature field and structural mechanics. Thus, the additive manufacturing process can be divided into two main stages: a heat transfer analysis and a mechanical analysis. Both stages are computed separately, presenting a one way coupling of thermo-mechanical computation, i.e. the transient thermal distributions computed during deposition of a component are stored at certain time steps and used as input data for the mechanical analysis [29].

3.3.5.1 Thermal Model

To simulate the heat effect during the PMD process, the total heat input introduced into the component has to be determined. The heat flow can be determined according to the process parameters used, considering the thermal efficiency and the density distribution function of the plasma arc. The local governing equation for the thermal problem is the balance of energy equation. This equation controls the temperature and the solidification evolution. It describes the distribution of heat over time in a solid medium with temperature dependent materials' properties and can be stated as a function of temperature [16]

$$\frac{\partial T}{\partial t} = \frac{\lambda(T)}{\rho(T)\,c_{\mathrm{p}}(T)}\,\vec{\nabla}^2 T + \frac{1}{\rho(T)\,c_{\mathrm{p}}(T)}\,\frac{\partial Q_V(x,y,z,t)}{\partial t} \text{ with } T = T(x,y,z,t)\,, \qquad (3.5)$$

where $\lambda, \rho, c_{\mathrm{p}}, T, Q_V$ represent the heat conductivity [W/(m·K)], the density [kg/m³], the specific heat capacity [J/(kg·K)], the temperature [K], and the volumetric heat source [J]. The temperature and volumetric heat source are a function of time and spatial coordinates. The general solution of the temperature distribution is obtained by applying the following boundary and initial conditions that can be written as

$$\vec{q}_{\mathrm{S}} = -\lambda(T)\left.\frac{\partial T}{\partial \vec{n}}\right|_{\mathrm{S}} = -\lambda(T)\vec{\nabla}T\big|_{\mathrm{S}}\,,$$

$$T(x,y,z,t=0) = T_0(x,y,z)|_{t=0}\,. \qquad (3.6)$$

The heat flux per unit of surface q_{S} [W/(m²·K)] as a function of temperature gradient is computed through Fourier's law. Fourier's law states that the time rate of heat transfer through a material is proportional to the negative gradient in temperature and to the area through which the heat flows. A heat flow is maintained as long as a temperature gradient exists. The proportionality constant is known as thermal conductivity and is generally dependent on the chemical composition, the microstructure and temperature. In metals, both electrons and lattice vibrations are the main charge carriers for heat conduction and electrical conduction. In general, good thermal conductors are also good electrical conductors. This relation is known as the Wiedemann-Franz law.

Thermal boundary conditions applied on the surface of the computational domain can be described as a Dirichlet (temperature history), Neumann (heat flux history) or Robin boundary condition, which is a combination of both. The main heat transfer mechanisms in plasma metal deposition are conduction and surface heat losses, which are dependent upon location within the build. In the first layers the cold baseplate acts as a heat sink and conduction is the dominant heat transfer mechanism. However, as the deposition proceeds, the underlying substrate temperature and wall height increase, convection and radiation become more important.

Heat radiation is the transfer of internal energy in the form of electromagnetic waves. The Stefan-Boltzmann law relates the heat flow rate emitted or absorbed from an object to its temperature. It is applied to all free surfaces, including those of the newly deposited material, and is the Neumann part of equation ((3.6))

$$\dot{q}_{\mathrm{R}} = \epsilon\sigma\left(T_{\mathrm{S}}^4 - T_\infty^4\right),\tag{3.7}$$

with $\varepsilon, \sigma, T_{\mathrm{S}}, T_\infty$ representing the emissivity [-], the Stefan-Boltzmann constant [W/(m²·K⁴)], the surface temperature and the far field temperature. The emissivity can be determined experimentally and numerically as an inverse problem. If the emissivity is known, the temperature of a body can be determined from the heat radiation emitted by the body. However, the emissivity is not only dependent on the material, but also on the surface condition of the body (e.g. oxidised surface).

Heat convection is a mode of heat transfer by the mass motion of a fluid. The movement of the fluid can be forced (forced convection) and free (natural convection). The governing equation of heat convection is the Newton's law reading

$$\dot{q}_{\mathrm{c}} = h_{\mathrm{c}}\left(T_{\mathrm{S}} - T_\infty\right),\tag{3.8}$$

where h_c is the heat transfer coefficient in [W/(m²·K)]. It depends on the type of media (gas or fluid), flow conditions on the surface, surface properties, and the temperature. The heat transfer coefficient is determined by empirical formulas using dimensionless parameters.

In addition to the effects of radiation and convection, heat transfer between bodies in contact affects the thermal behaviour. Since in many cases components to be joined are in contact with others, heat transfer takes place via the contact surfaces. Contact heat transfer between two bodies depends on their temperatures and the contact heat transfer coefficient a

$$\dot{q}_{\mathrm{a}} = a\left(T_1 - T_2\right).\tag{3.9}$$

Since material surfaces are usually technically processed, they show surface structures that do not correspond to an ideally smooth plane. Due to these manufacturing limitations, two solid surfaces that are brought together never form a perfect contact. Due to the roughness of the surfaces, small gaps (usually filled with air) always occur at the contact points. The heat transfer via the interface of the two contacting surfaces can be achieved with two mechanisms. Firstly, heat can be conducted through points of solid-to-solid contact, and, secondly, heat can be conducted through the gas-filled gaps. The contact heat transfer coefficient a depends on the materials in contact, the surface condition of the contacting partners, contact pressure and the fluid inside the cavities.

Thermal boundary conditions are modelled by adding equation ((3.7)) to ((3.9)) to equation ((3.6)) resulting in

$$\epsilon\sigma\left(T_{\mathrm{S}}^4 - T_\infty^4\right) + h_{\mathrm{c}}\left(T_{\mathrm{S}} - T_\infty\right) + a\left(T_1 - T_2\right) = -\lambda\vec{\nabla}T.\tag{3.10}$$

The heat transfer mechanisms through the boundary govern the cooling behaviour of the model and can, by insufficient accuracy, have a huge impact on the simulation results [36].

3.3.5.2 Mechanical Model

The thermal and structural result fields are not calculated simultaneously, but sequentially in an iterative process where the thermal analysis is followed by a thermal history dependent quasi-static mechanical analysis in a sequentially coupled model [29]. The temperatures calculated in the previous analysis step serve as input for the next structural step and are needed to compute thermal expansion in the whole domain and to define thermo-mechanical properties. The stress state of the structure depends accordingly on the structural constraints and loads, as well as on the thermal expansion under thermal loads. The governing stress equation can be expressed by Cauchy's equation for a static problem

$$\text{div}(\sigma) + \vec{f}_{\text{int}} = 0,\tag{3.11}$$

where σ is the stress tensor and $\vec{f}_{\text{int}}$ are internal body forces. The mechanical constitutive law relates stresses and strains and is written in the form of generalised Hook's law

$$\sigma = C : \varepsilon^{\text{el}},\tag{3.12}$$

$$\varepsilon = \varepsilon_{\text{el}} + \varepsilon_{\text{pl}} + \varepsilon_{\text{th}},\tag{3.13}$$

where C is the fourth order material stiffness tensor. The total strain tensor, assuming small deformations and thermo-elastic-plastic behaviour, can be decomposed into elastic strains, plastic strains and thermal strains.

The elastic strain ε_{el} is computed by means of Hook's law

$$\varepsilon_{\text{el}} = \frac{1+\nu}{E}\sigma - \frac{\nu}{E}tr(\sigma),\tag{3.14}$$

where E is the Young's modulus [MPa] and ν the Poisson's coefficient [-]. Plastic behaviour and the calculation of plastic strain ε_{pl} is described by a yield criterion, a flow rule and hardening law. For a multi-axial stress state, the yield criterion describes the onset of plastic flow, the flow rule links the plastic strain increments with the actual stress state and stress increments. The hardening law specifies how the yield criterion is changed by plastic flow. The plastic strain increment can be derived from a plastic potential g

$$\text{d}\varepsilon_{\text{pl}} = \text{d}\lambda\frac{\partial f}{\partial \sigma} = \text{d}\lambda\nabla g,\tag{3.15}$$

where $\text{d}\lambda$ is a positive scalar of proportionality. The thermal strain ε_{th} is computed as

$$\varepsilon_{\text{th}} = \alpha(T)(T - T_\infty),\tag{3.16}$$

where α is the thermal coefficient of expansion [ppm/K], T the nodal temperature and T_∞ a reference temperature. Thermal strain ensures correct distortion calculation during material deposition as well as thermal shrinkage during global cooling of the workpiece [29]. Transformation induced plasticity and transformation strains and thus the effects of phase changes are neglected in this study.

3.3.5.3 Thermal materials properties

Structural welding simulations require the specification of temperature-dependent thermo-physical and thermo-mechanical material parameters. Thermo-physical parameters include thermodynamic quantities, such as thermal conductivity, density and heat capacity, as well as thermo-metallurgical quantities that characterise the behaviour of solid phase transformations. Material properties, such as thermal expansion, modulus of elasticity, transverse contraction, stress-strain behaviour and transformation plasticity are assigned to the thermo-mechanical properties. These parameters are determined experimentally or can be obtained from literature or libraries, such as JMatPro. Simufact Welding 8.0 comes with its own database providing relevant parameters for the execution of structural welding simulations. Temperature dependent thermal and mechanical properties of Ti-6Al-4V found in literature are listed in Appendix B - Thermo-mechanical properties of Ti-6Al-4V and can be used as an informative basis.

4 Experiment

PMD is a direct energy deposition process that involves the combination of a plasma welding source to deliver the heat input and deposit the wire, a motion system (robot or CNC) to follow the paths of the geometry, a control board to control the machine and a wire feeder to control the deposition of the feedstock material. PMD operators face various challenges, such as the component's geometry, building strategy, bead formation, resulting microstructure, mechanical properties, residual stresses, warpage, costly iteration loops, long lead-times, post-process treatments and final contour milling. These key elements already indicate the complexity of plasma metal deposition. As a research company, RHP-Technology is often faced with new materials and part geometries making the PMD process a challenging endeavour. The aim of this study is to investigate some key aspects of plasma-based wire and arc additive manufacturing and to enhance this technology at RHP-Technology to industrial maturity.

4.1 Methodology

The deposition experiments are performed on a custom made PMD system at RHP-Technology utilising plasma metal deposition. The system is comprised of a Merkle HighPULSE 452 RS power source and a plasma torch (the diameter of the tungsten electrode is 4.8 mm, the tip angle 30°) mounted on a 3-axis CNC gantry. Cold Ti-6Al-4V wire with a diameter of 1.2 mm is fed by an automatic wire feeder. Thin-walled samples (so called demonstrators) are manufactured by depositing a single row of successive weld beads along the centreline of Ti-6Al-4V base plates measuring 200x50x10 mm. Both, baseplates and welding wire are commercially sourced and have been produced according to ASTM B265 and AWS A5.16-07 respectively. Aerospace grade 5 Ti-6Al-4V welding wire and titanium grade 5 hot rolled plates have been supplied by Shaanxi Lasting Titanium Industry CO., LTD. The chemical compositions are shown in Table 1 and Table 2.

Table 1: Chemical composition of Ti-6Al-4V wire (wt.%)

Ti	Al	V	Fe	C	N	H	O	Residuals each	Residuals total
Bal.	6.24	4.16	0.15	0.015	0.008	0.003	0.13	<0.10	<0.40

Table 2: Chemical composition of Ti-6Al-4V base plates (wt.%)

Ti	Al	V	Fe	C	N	H	O	Residuals each	Residuals total
Bal.	6.12	4.07	0.178	0.019	0.011	0.002	0.012	<0.10	<0.40

The initially 200x200x10 mm large substrates are water jet cut to a dimension of 200x50x10 mm and subsequently milled on an OKUMA GENOS M560-V-e CNC vertical machining centre. A 2D drawing of the baseplates is shown in Figure 15.
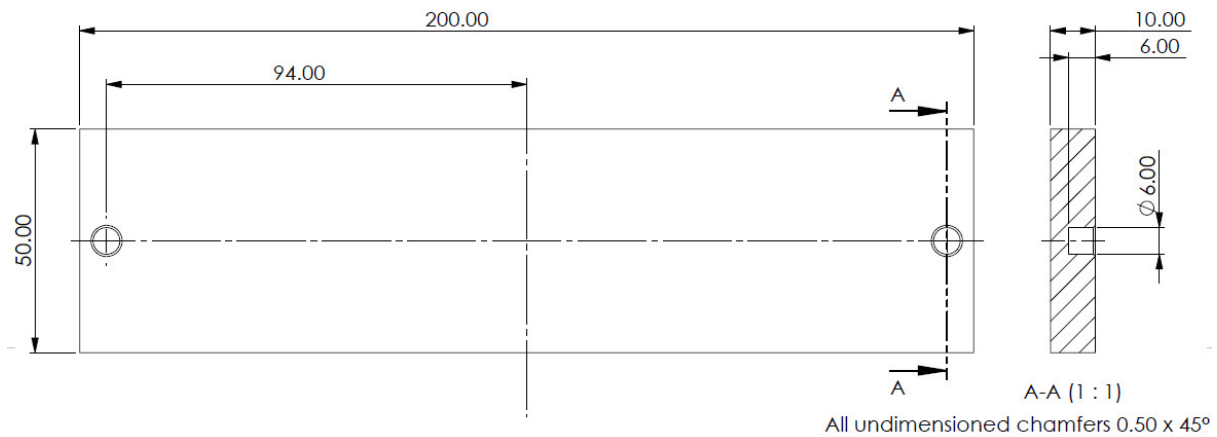
Figure 15: Schematic view of the baseplates

Two blind holes of 6 mm diameter are machined along the centreline of the baseplates. These holes are used to additionally position the plates inside the working space and reference to the tool coordinate system.

4.2 Experimental setup

The deposition process is enclosed in an airtight welding chamber filled with high purity argon (99.99 % purity) with a low moisture content, thus utilising a protective gas atmosphere and giving adequate shielding. A standard reference coordinate system of the single wall is defined, in which x is parallel to the travel direction of the torch, y is the transverse direction, and z is parallel to the building direction of the wall. The experimental set-up is shown in Figure 16.
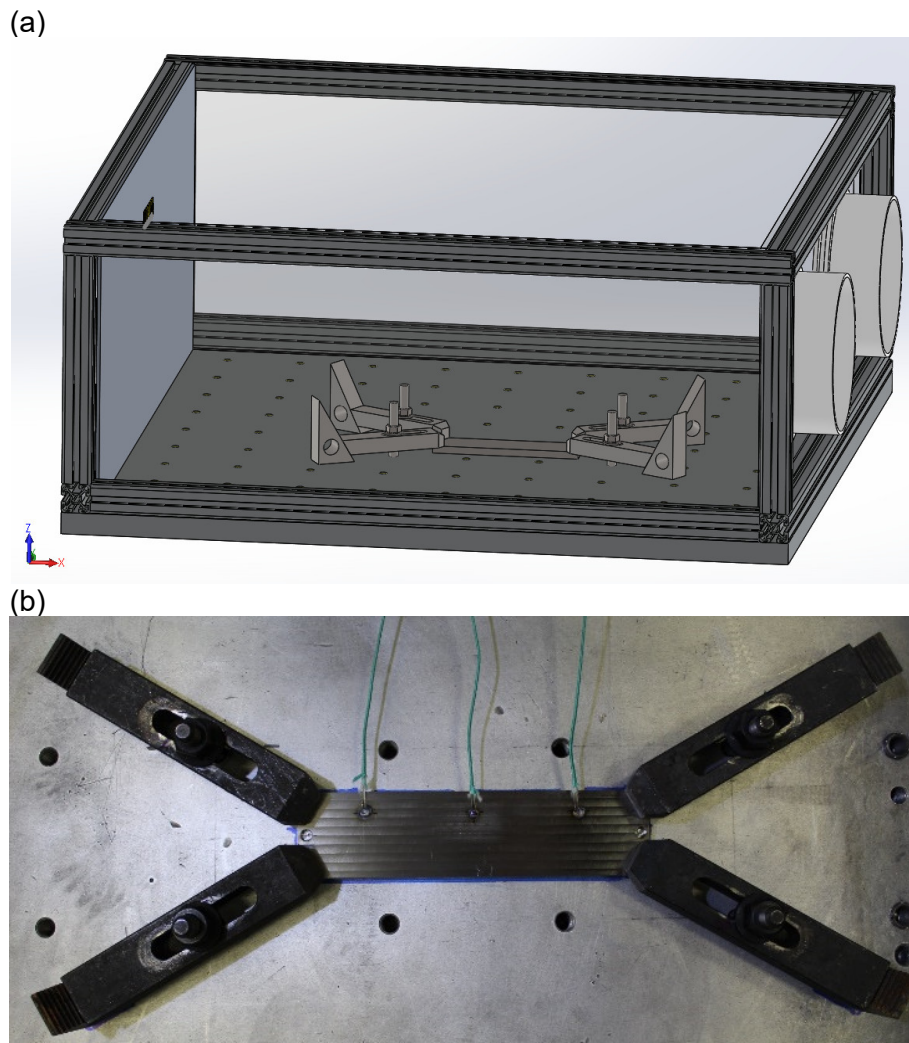
(a)

(b)

Figure 16: (a) Model of the welding chamber; (b) Experimental set-up inside the welding chamber

The baseplates are fixed to the backing plate of the welding chamber using four clamps placed at specified positions to ensure identical clamping conditions for all demonstrators. The studs are tightened crosswise with a torque of 80 Nm. Prior to the AM process the baseplates are degreased and cleaned with acetone to eliminate surface contamination. Deposition is initiated below a residual oxygen content of less than 100 ppm O_2 measured with a residual oxygen analyser OXY 3 by ORBITEC, which has a measuring range from 5ppm to 21 % O_2. A single track wide bidirectional deposition strategy is adopted, i.e. the starting point of the next layer is where the previous layer finished. Cold wire is fed by an automatic wire feeder transversal to the welding direction to avoid rotation of the torch. Although in-house research at RHP-Technology has shown that a feed mode, in which the wire is fed ahead of the arc yields more consistent weld beads, the transversal position is a good compromise for the bidirectional welding strategy. Further automation of the custom-made machine would be required to rotate the torch according to the direction of deposition. The deposition strategy is shown in Figure 17, where the orange lines represent the movement of the torch. When the torch comes to the end of the weld bead, the arc is extinguished, the torch increases its height in z direction and remains in this park position for a defined cooling time. After the dwell time has elapsed, the torch moves in negative z direction towards the end position of the previous layer and starts to deposit a new layer in the reverse direction. Thereby, the distance between

the torch and the deposited layers is kept constant at 10 mm. This process is repeated until a desired number of layers is deposited.
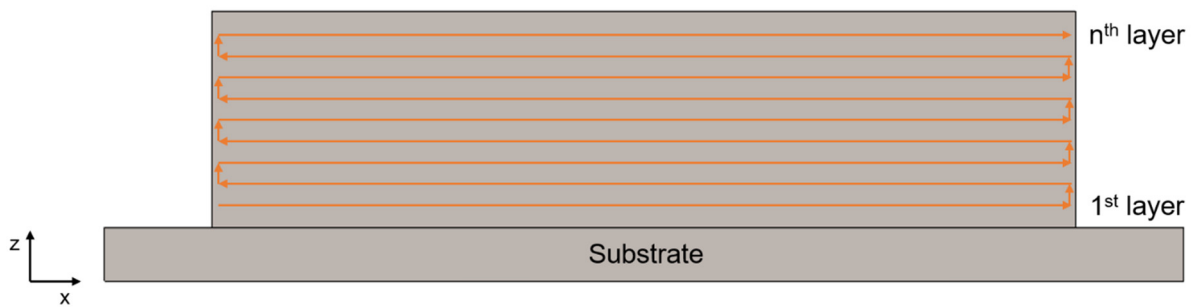

Figure 17: Bidirectional building strategy

The bidirectional strategy aims to mitigate the inconsistency in wall height as reported by Martina et al. [37]. Using a unidirectional welding strategy, i.e. starting each layer at the same point, will cause a hump in the beginning and a depression towards the end of a wall. The same authors [37] attribute the depression at the end to a build-up of heat caused by the lack of heat sink in front of the torch and the hump in the beginning may be caused by thermal effects associated with the deposition on the cold base material.

Ten thin-walled demonstrators are manufactured to investigate post-process distortion and weld induced residual stresses which are generated by the high thermal input of the PMD process. Demonstrators D1 and D2 are fabricated to test and adjust the welding parameters and are excluded from further analysis. Before deposition, all baseplates are preheated with two single passes of the arc without feeding wire to avoid the first single track to become too narrow and prevent separation of the wall from the baseplate.

4.3 Process parameters

The most important welding parameters are the welding current I, the travel speed (TS) of the torch, and the wire feed speed (WFS). To reduce the number of independent variables and therefore reduce the complexity of the experiments, all demonstrators are deposited employing the same set of parameters which are listed in detail in Table 3. High purity argon is used as process and shielding gas.

Table 3: Deposition parameters

Description	Symbol	Preheating	Deposition	Unit
Wire diameter	d	-	1.2	[mm]
Welding current	I	130	140	[A]
Voltage	U	25	25	[V]
Travel speed	v_{TS}	300	200	[mm/min]
Feed rate	f	-	0.9	[kg/h]
Wire feed speed	v_{WFS}	-	2910	[mm/min]
Cooling time	t_{cool}	1	30	[s]
Total dwell time	t_{dwell}	9	38	[s]
Number of layers	N	2	32	[-]
Pilot gas		1.5	1.5	[l/min]
Shielding gas		5	5	[l/min]

In arc welding processes the heat input at the welding point can be quantified by the linear energy density E_l [J/mm] which is a measure for the averaged applied energy per unit length [38], [39]

$$E_l = \frac{P}{v_{TS}} = \eta \frac{UI}{v_{TS}},$$ (4.1)

where P denotes the power [W], U the arc voltage [V], I the welding current [A], v_{TS} the travel speed [mm/min], and η the thermal coefficient of efficiency. The line energy density can be extended to the volumetric energy density E_v [J/mm³] which is a measure for the averaged energy per unit volume of material during the deposition of a layer [38], [40], [41]

$$E_v = \frac{P}{\dot{V}} = \eta \frac{UI}{v_{TS} \cdot A_{MD}} = \eta \frac{UI}{v_{WFS} \cdot A_W},$$ (4.2)

where A_{MD} and A_W denote the cross section of the deposited material and the cross section of the wire, and v_{WFS} [mm/min] is the speed at which the wire is fed into the weld pool. Assuming mass conservation $\dot{V}_{MD} = \dot{V}_W$, i.e. the growth of a layer per unit length and time corresponds to the amount of wire fed into the molten pool per unit length and time, the cross section area of the deposited material can be calculated beforehand. It is given by the diameter of the feed wire d, the wire feed speed v_{WFS} and the travel speed v_{TS} resulting in

$$A_{MD} = \left(\frac{d^2\pi}{4}\right) \cdot \frac{v_{WFS}}{v_{TS}} = WW \cdot LH .$$ (4.3)

Wall width (WW) and layer height (LH) are the most important geometrical parameters. The v_{WFS}/v_{TS} ratio can be used to ensure constant material deposition per unit length and has been introduced by Almeida and Williams [42] as an independent process variable reading

$$\frac{v_{\text{WFS}}}{v_{\text{TS}}} = \frac{A_{\text{MD}}}{A_{\text{W}}} = const. \ . \tag{4.4}$$

Empirical models have been developed in several scientific works [37], [42], [43] to predict a series of responses from the input parameters and allow a systematic approach towards geometrical modelling of plasma deposited components.

4.4 In situ temperature measurement

In situ measurements of the temperature are made at three selected locations on top of the baseplates using 0.81 mm diameter type-K thermocouples provided by OMEGA, as shown in Figure 18. The thermocouples have a glass fibre isolation and an accuracy of ± 2.2 °C or ± 0.75 % in a temperature range from 0 to 1250 °C. The thermocouples are welded on the top surface of the baseplates to ensure a proper thermal contact and are covered with steel sleeves to shield them from the plasma (Figure 18). Test runs have shown that a current can be induced through electro-magnetic effects of the plasma leading to noise in the data. In addition, the steel sleeves prevent the thermocouples from being exposed to the direct heat of the plasma which can lead to a detachment of the joints. The goal is to place the thermocouples as close as possible to the deposited wall, but still gain significant data. A PCE-T 390 multichannel digital thermometer is used to read and store the thermocouple signals. Data are recorded with a sampling frequency of 1 Hz.
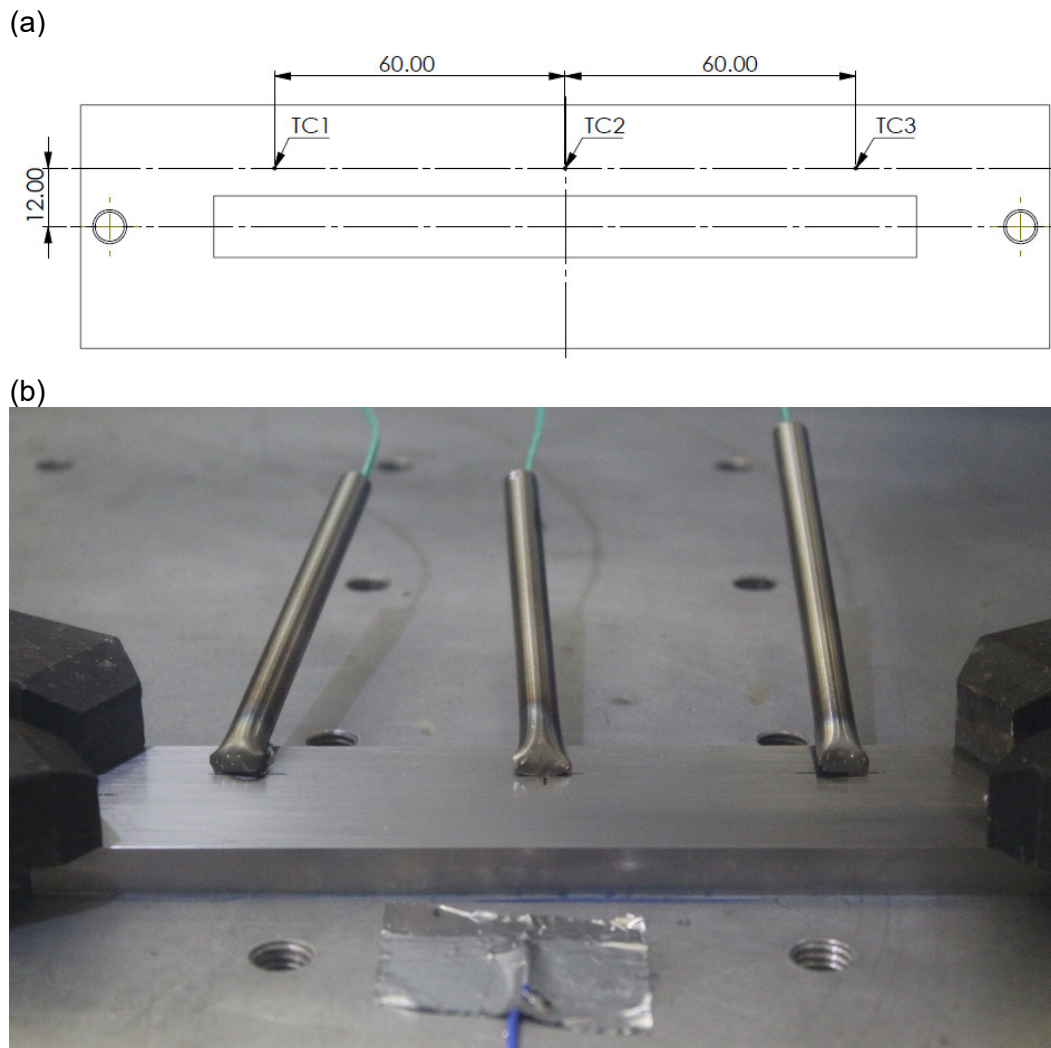
(a)

(b)

Figure 18: (a) Schematic view of the thermocouple locations on the top surface of the baseplate; (b) Steel pipes protecting the thermocouples from the plasma

Additional PCE TF-500 type K thermocouples are installed to capture the temperature of the backing plate, the clamps and the ambient inside the welding chamber. The thermocouple data are processed in MATLAB R2016a to determine temperature profiles of the plasma metal deposition process. The temperature history is further used to validate the numerical model in Simufact Welding 8.0.

4.5 Post-process distortion measurement

Distortion is defined as the changes in the dimensions and the shape of a workpiece. Dimensional and shape changes can occur individually, but are usually superimposed. To obtain distortions imposed by the PMD process the pre- and post-process profiles of the baseplates are scanned utilising a coordinate measuring machine (CMM). Measurements with a HEXAGON m&h IRP40.02 infrared touch probe system with a 1 mm ruby stylus are performed along the top and bottom surfaces of the baseplates. The measurement grid on the top surface consists of 40 points, whereas the measurement grid on the bottom surface consists of 45 points, respectively. The locations at both surfaces are identified in Figure 19.
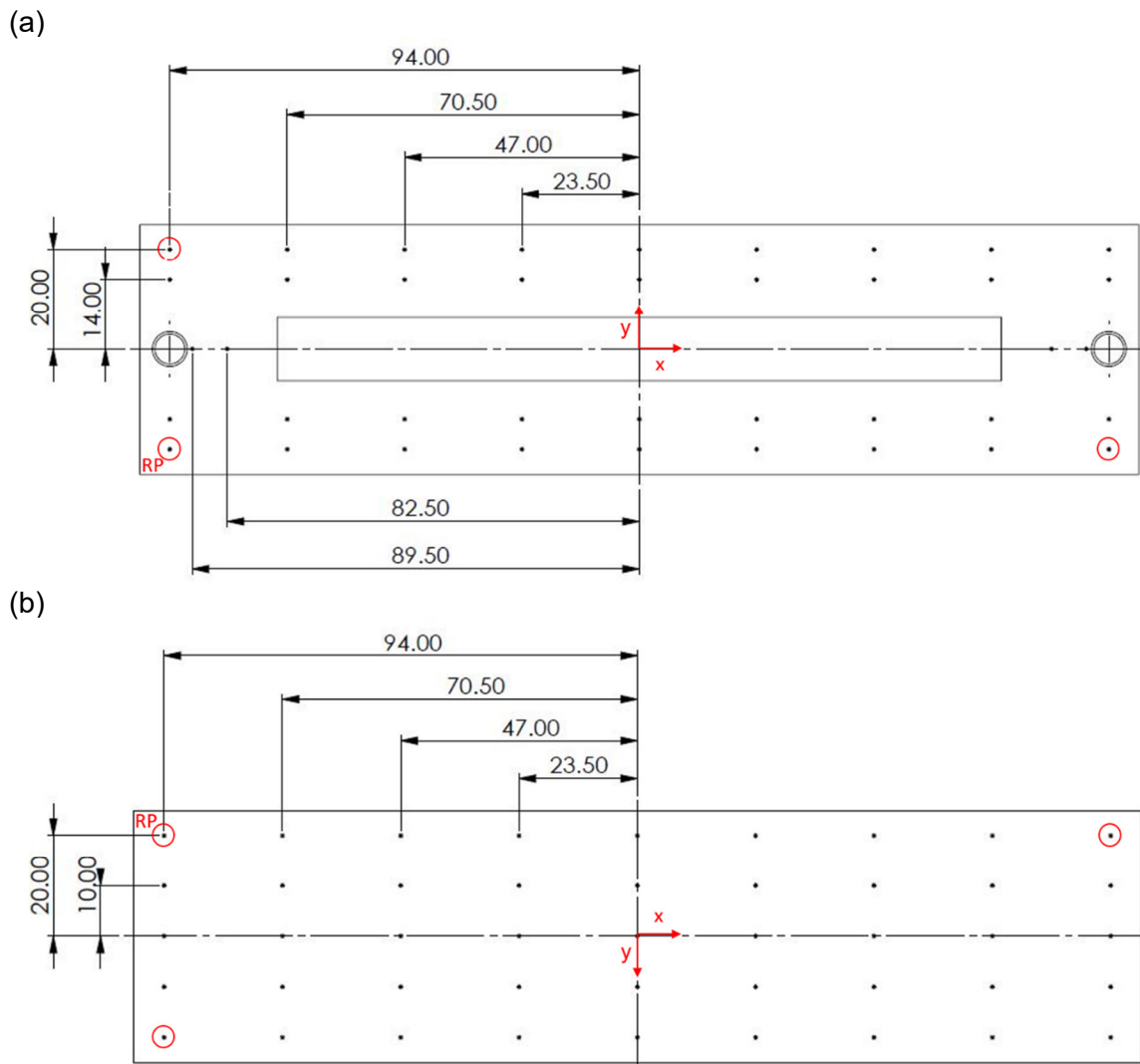
(a)

(b)

Figure 19: Schematic view of CMM points on the (a) top surface, and (b) bottom surface of the baseplate

The bottom surface is scanned with a 9x5 measurement grid, with a grid spacing of 23.5 mm in x and 10 mm in y direction. A different strategy is adopted for the top surface, since the single bead wall and the two blind holes do not allow a constant grid spacing. Hence, a measurement grid of 40 points in total is defined for the top surface. A reference plane with the points marked in red is constructed for each surface to align the coordinate frames of both surfaces. Rigid body translation and rotation is applied to make these planes parallel to the xy-plane. Additionally, a reference point (RP) is defined as centre of rotation. The results from the discrete data points are then used to calculate the changes in plate profile and out-of-plane distortion by subtracting the pre-process from the post-process measurements. For reasons of symmetry, sampling lines along the longitudinal direction with symmetric y-values are merged to one single line and their mean values and standard deviations are calculated. This results in effective sampling lines for y=0 mm, y=14 mm and y=20 mm for the top surface and y=0 mm, y=10 mm, y=20 mm for the bottom surface, respectively The experimentally determined distortion is then used to evaluate the simulation results obtained by Simufact Welding 8.0. Since the building strategy causes a symmetry break along the transverse direction, this analysis method is not applicable for the transverse direction.

5 Simulation

The thermal analysis of the PMD process involves the solution of a heat transfer problem with a moving heat source. The heat source is a mathematical description of the heat transfer of the arc to the molten pool which describes the energy distribution inside the weld pool. The determination of precise values of the Goldak double ellipsoid heat source is crucial for the simulation results. Criteria for determining the parameters of the heat source model commonly involve three aspects [44]:

i. Determination of the heat source parameters according to the measured welding temperature.
ii. Determination of the heat source parameters according to the weld pool shape.
iii. Determination of the heat source parameters according to measured residual stress or distortion.

These criteria need to be judged with regard to whether the values of the model parameters are accurate or not. In this study the relevant quantities for the calibration of the mathematical heat source are identified by a validation of the resulting temperature distribution of the real heat source within the component and a metallographic analysis of the weld pool shape using micrographs. The micrographs provide information on the internal microstructure and allow a geometrical determination of the weld seam, heat-affected zone and fusion zone. The calibration procedure, however, leads to an inverse problem in two ways. Firstly, the temperature distribution and the isothermal surface of the weld pool are known, and, secondly, the exact shape and losses of the heat source are unknown. The goal of the calibration is to calculate a temperature distribution by variants of different heat sources to match the measured values with the computed values as accurately as possible. In general, it is necessary to perform a number of simulation variants to calibrate the heat source.

5.1 Heat source calibration

According to Gu et al. [44], the methods for determining the heat source parameters can be generally divided into three categories: trial and error, regression analysis and intelligent computing. In this study a trial and error analysis is employed. Although one of the main drawbacks of using the trial and error method is that its efficiency and accuracy strongly depend on the experience of the user, this method does not require any additional effort to set up regression models or algorithms for intelligent computing. The steps of the calibration procedure employed in this study are the following:

1. Estimation of the molten pool dimensions and seam geometry.
2. Experimental setup and determination of thermo couple positions.
3. Calibration experiments.
4. Simulation setup in Simufact Welding.
5. Trial and error analysis.

5.1.1 Estimation of the molten pool dimensions and seam geometry

In the first step of the calibration procedure, two short weld beads are welded on dummy baseplates to estimate the dimensions of the isothermal surface of the weld pool and the dimensions of the weld bead geometry. The welding parameters correspond to the process parameters utilised for the fabrication of the PMD walls in chapter 4. Figure 20 (a) shows a preheating pass, Figure 20 (b) a preheating pass with a subsequent welding pass. The baseplates are measuring 100x20x10 mm.
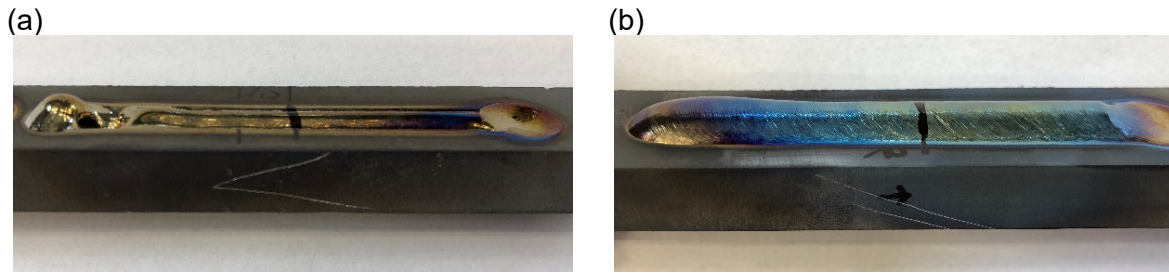
(a) (b)

Figure 20: Weld seams (a) Preheating pass, and (b) preheating pass with a subsequent welding pass

Samples are extracted from the Ti-6Al-4V baseplates, embedded in Bakelite, grinded, polished and etched with Kroll's agent. The micrographs are then metallographically analysed by using an optical microscope. Information about the microstructure, the dimensions of the weld seam and the heat-affected zone are determined. Figure 21 shows the corresponding micrographs of the preliminary test welds.
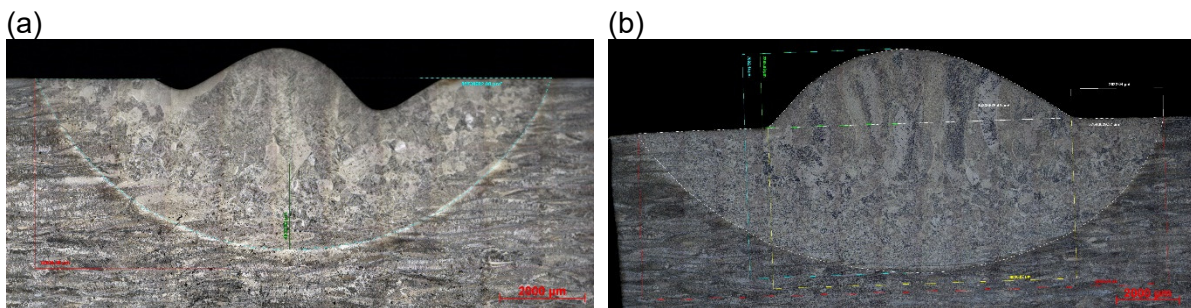
(a) (b)

Figure 21: Micrographs (a) Preheating pass; (b) Preheating pass with a subsequent welding pass

From the micrographs the width b, depth d and area A of the heat affected zone and the weld bead are determined. In relation to the weld bead the depth d represents the height of the seam. Dimensions of the HAZ of the preheating pass are provided in Table 4, HAZ and bead dimensions of the preheating pass with the subsequent welding pass are provided in Table 5.

Table 4: Analysis of the preheating pass

Geometry	$2\,b$ [mm]	d [mm]	A [mm²]
HAZ	12.20	4.03	35.74

Table 5: Analysis of the single bead with preheating

Geometry	$2\,b$ [mm]	d [mm]	A [mm²]
HAZ	16.69	4.73	57.64
Bead	9.64	2.36	14.84

These preliminary tests give a first indication of the expected geometrical dimensions of the weld bead, heat affected zone and fusion zone of plasma deposited Ti-6Al-4V which are essential for the heat source calibration.

5.1.2 Experimental setup and determination of thermocouple positions

The preliminary trials in the previous chapter provided a first estimation of the expected weld pool geometries. The actual experimental setup for the calibration, indeed, is subject to certain requirements. The length of the baseplate must be sufficient to allow the development of a stationary process and to ensure that the heat accumulation at the end of the process does not influence the temperature measurements. Additionally, the boundaries of the baseplate perpendicular to the weld direction impose certain restrictions. The influence of these boundaries on the temperature evolution is stronger the smaller the distance to the heat source. Based on these considerations, the baseplate dimension of 200x100x10 mm is set for the calibration tests.

The temperature distribution measured during the deposition process is decisive for the calibration of the heat source. Due to large temperature gradients during welding, a measuring method with high sampling rates and short response times is required, which is achieved with thermocouples. With increasing size of the contact area, the accuracy of the thermal contact is improved. A small diameter, on the contrary, improves the response time. Therefore, a compromise between measurement location, thermoelement type (temperature range, wire or mantle thermocouple), response time and contact area is established. To identify the thermal profiles within the workpiece, thermocouples are placed at specified measuring points on the baseplate. The method is in line with the work conducted by Paul Helbig [45]. Based on his work three thermocouples are placed at certain locations sloping upwards with increasing distance in welding direction, as can be seen in Figure 22. This set-up allows to capture peak temperatures and thermal gradients.
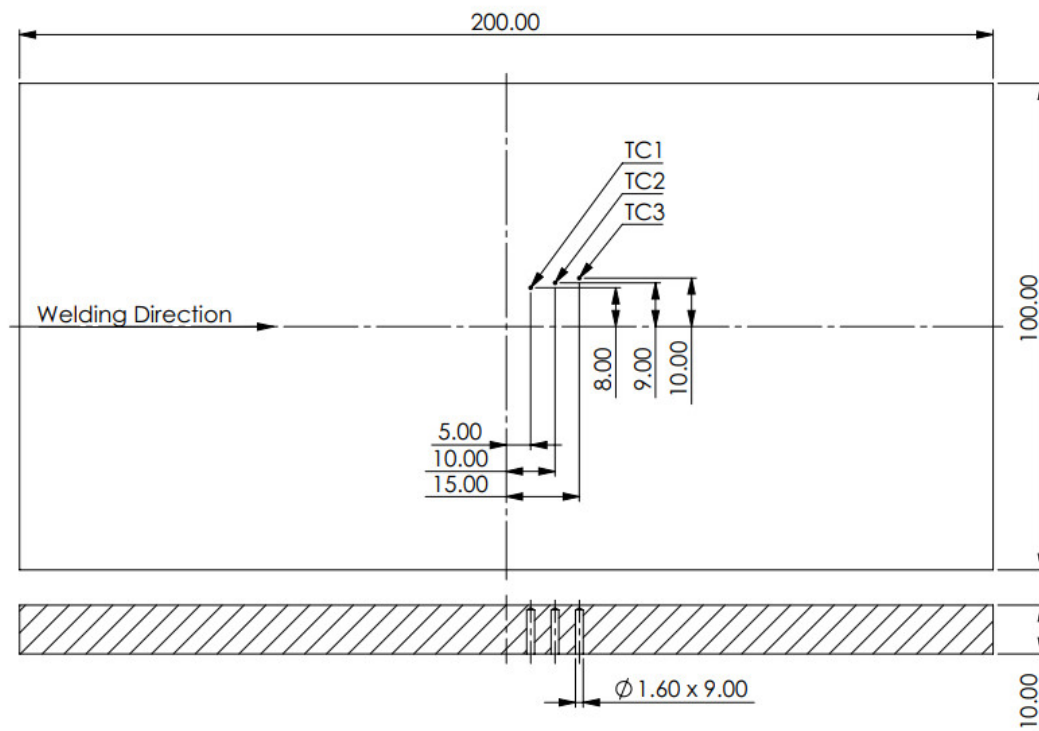

Figure 22: Thermocouple locations

The temperature evolution is measured inside the baseplate by forcing insulated thermocouples into pre-drilled holes from the bottom of the baseplate. In situ temperature measurements are made using 1.5 mm diameter type-K thermocouples provided by B+B sensors. The thermocouples have a measuring accuracy of ± 1 °C or ± 0.40 % in a

temperature range from -40 to 1000 °C after DIN EN 60584-1, class 1. The drill depth of the holes (z-direction) measures 9.0 mm, the diameter is 1.6 mm. The holes are pre-drilled on a bench drill. The thermoelements can be inserted to a total depth of 9.4 mm. A heat-conductive paste is filled inside the holes to ensure proper thermal contact. A PCE-T 390 multichannel digital thermometer is used to read and store the thermocouple signals. Data are recorded with a sampling frequency of 1 Hz. Hereby should be noted that the attachment of the thermocouples on the top surface (as realised in chapter 4 for the PMD walls) in close proximity to the centre of the seam is not applicable. The hot plasma stream causes the welded joint between the thermocouple and the baseplate to remelt and consequently to break the bond. The experimental set-up for the calibration can be seen in Figure 23.
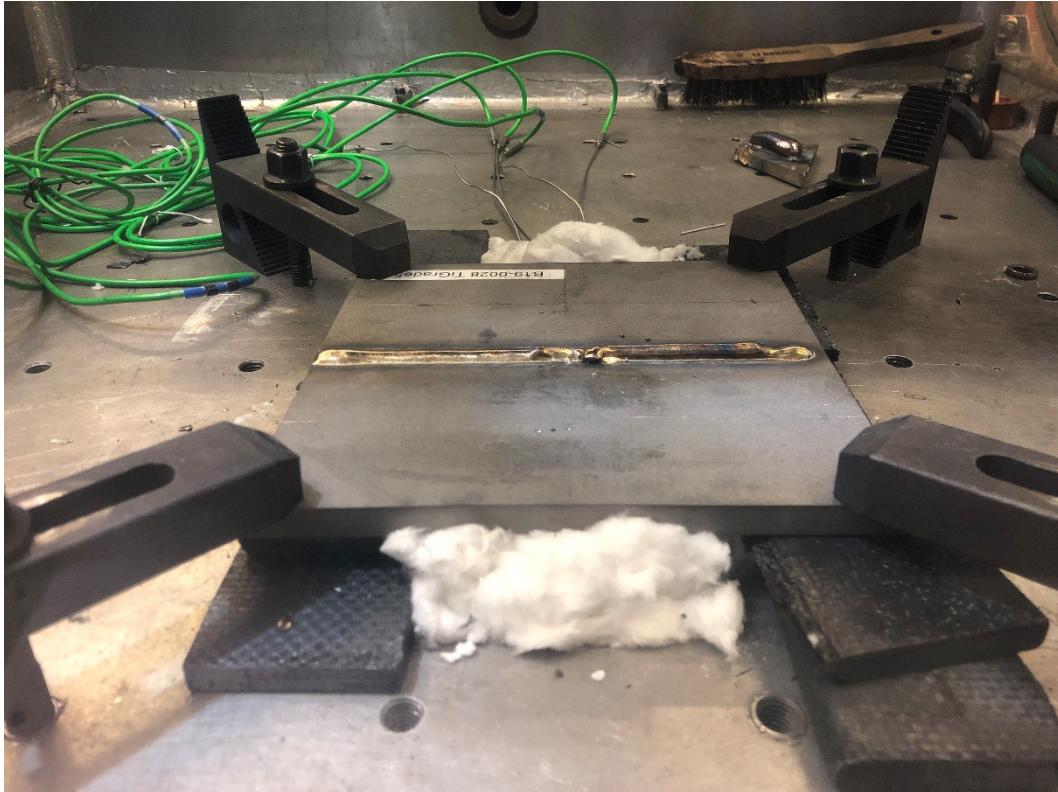

Figure 23: Experimental set-up for the calibration runs

The baseplate is supported with CFCs and the air gap in-between is filled with alumina wool to completely isolate the bottom surface of the baseplate from the backing plate. Losses due to contact heat transfer to the backing plate and due to convective heat transfer inside the air gap are minimised. Weld beads with a length of 170 mm are produced to obtain a stationary process. The positioning of the thermocouples from the bottom, however, has one main drawback. This measurement setup requires sufficient space between the baseplate and the backing plate to guide the thermocouples without kinks. Therefore, no direct contact between backing plate and baseplate is realised and information of the contact thermal conductivity from the baseplate to the backing plate cannot be acquired.

5.1.3 Calibration experiments

In total three calibration runs are performed: firstly, a single preheating pass, secondly a single printing pass, and thirdly, two preheating passes with a subsequent printing pass. Thermal profiles are measured during deposition at specified locations defined in Figure 22. After the experiments, samples are extracted, embedded in Bakelite, grinded, polished and etched with Kroll's agent. The micrographs are then metallographically analysed by using an optical

microscope which provides information about the microstructure and the dimensions of the weld seam and heat-affected zone. The resultant micrographs can be seen in Figure 24.
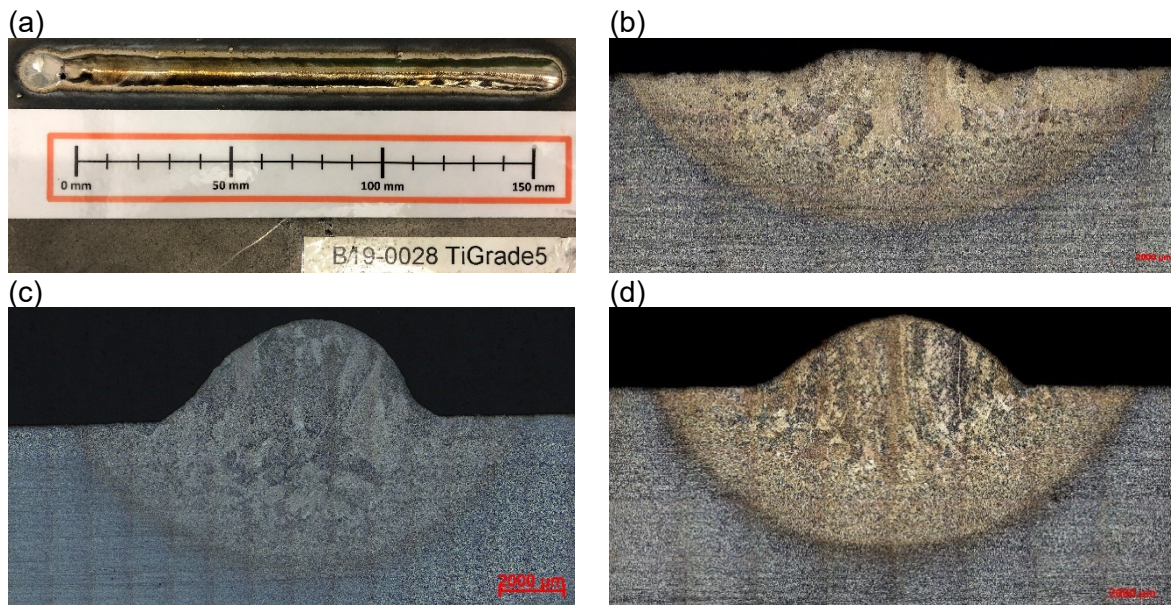

Figure 24: (a) Single seam; (b) Micrograph preheating pass; (c) Micrograph single seam; (d) Micrograph single bead plus preheating

From the micrographs the width b, depth d and area A of the heat affected zone and the weld bead are determined. In relation to the weld bead the depth d represents the height of the seam. Dimensions of the HAZ, FZ and bead geometry of the corresponding calibration runs are provided in Table 6, Table 7 and Table 8.

Table 6: Analysis of the preheating pass

Geometry	$2\,b$ [mm]	d [mm]	A [mm²]
FZ	6.34	1.56	5.85
HAZ	13.08	3.72	34.52

Table 7: Analysis of the single bead

Geometry	$2\,b$ [mm]	d [mm]	A [mm²]
FZ	8.88	2.68	16.74
HAZ	13.43	4.41	41.95
Bead	8.82	3.15	17.36

Table 8: Analysis of the single bead with preceding preheating

Geometry	$2\,b$ [mm]	d [mm]	A [mm²]
FZ	9.45	3.12	20.81
HAZ	16.77	5.62	68.68
Bead	9.50	2.54	15.58

Comparing the results presented in Table 7 and Table 8, the single bead plus preheating shows an increased bead width with a simultaneous reduction of height. Furthermore, the HAZ and FZ of the bead with preheating are significantly larger due to the higher energy input. Considering material deposition, the area of the single bead plus preheating and the single bead without preheating are within measurement uncertainties in good agreement with equation ((4.3)), which gives the cross-sectional area of the deposited material as a function of wire feed speed, travel speed and wire diameter resulting in

$$A_{\text{MD}} = \left(\frac{d^2\pi}{4}\right) \cdot \frac{v_{\text{WFS}}}{v_{\text{TS}}} = \left(\frac{1.2^2\pi}{4}\right) mm^2 \cdot \frac{2910 \, mm/min}{200 \, mm/min} = 16.45 \, mm^2 \, . \tag{5.1}$$

The deviations of the cross-sectional area of the welded beads from the theoretical are within a range of ± 5.5 % and can be explained by the formation of corrugations along the welding path. The micrographs have been obtained at a single position along the whole bead.

5.1.4 Calibration setup in Simufact Welding 8.0

Within Simufact Welding the welding process is designed based upon manufacturing data - welding process, energy input, welding speed, filler material, welding metallurgy, clamping concept, components and the finite element mesh have to be defined. All components have been designed in SoildWorks 2018 and meshed in Abaqus CAE 6.14. Symmetry properties are exploited by modelling only one half of the calibration setup. This significantly reduces calculation time. The CFC and alumina wool support are modelled as one single component to reduce complexity and to enable the implementation of one effective contact heat transfer coefficient over the bottom surface of the baseplate. The cross-section profiles of the weld beads are modelled by a second-degree polynomial fitting curve in the form of

$$f(x) = -c_2 x^2 + c_0 \, . \tag{5.2}$$

The parabolic model is in good agreement with the actual shape of the weld beads. Two coefficients c_0 and c_2 have to be determined. Since height, width and area of the single beads are known, the function is over defined. By convention, this work defines the area and the width as driving parameters for the calculation of the coefficients, therefore keeping the height as free variable. The coefficients of the single beads are specified in Table 9.

Table 9: Parameters of the weld bead fitting function

Geometry	c_2 [mm^{-1}]	c_0 [mm]
Single bead	-0.15181	2.95
Single bead with preheating	-0.10903	2.46

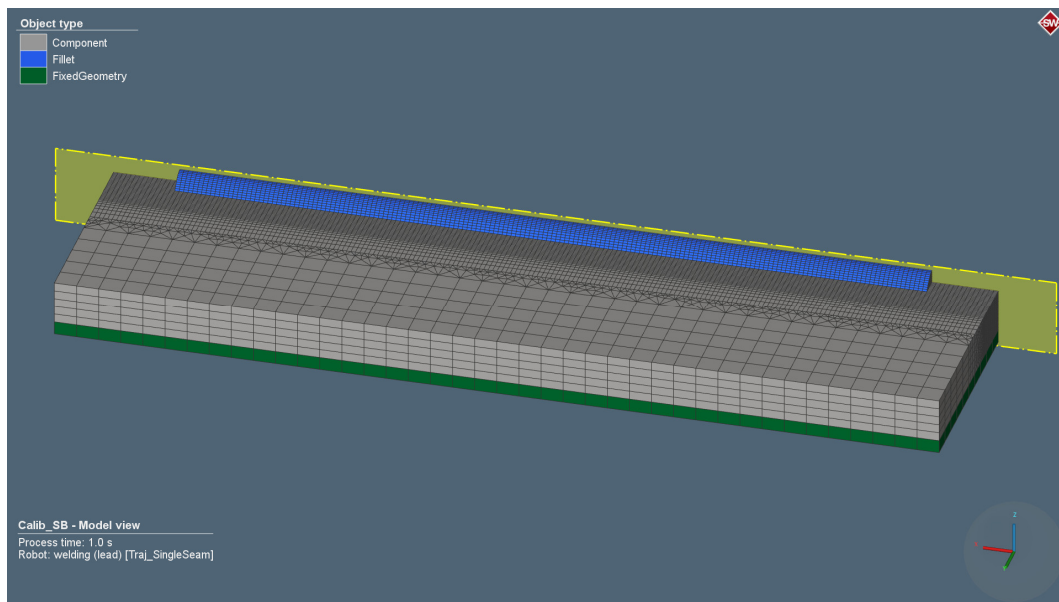The model view of the calibration setup can be seen in Figure 25.

Figure 25: Model view of the calibration setup

Figure 25 presents the 3D half symmetry mesh that is used for the thermal analysis of the calibration experiments. The yellow surface represents the symmetry plane. Clamps constraining the baseplate are not included in the thermal analysis of the calibration. The reasons can be summarised as the following: firstly, the fixations have been hand-tightened just to keep the assembly in position not applying any significant pressure to establish an effective thermal contact, secondly, the contact area of all four clamps is significantly smaller than the contact area of the backing plate, and thirdly, because of reasons of simplicity. For the thermal model, linear hexahedral elements of type C3D8R and linear wedge elements of type C3D6 are used for the thermal simulation. To capture the thermal performance around the heat source, dense meshes of size 1x0.5x0.5 mm are used for the bead and the area near the welding line. The mesh becomes coarser in y-direction away from the welding line (Figure 26).
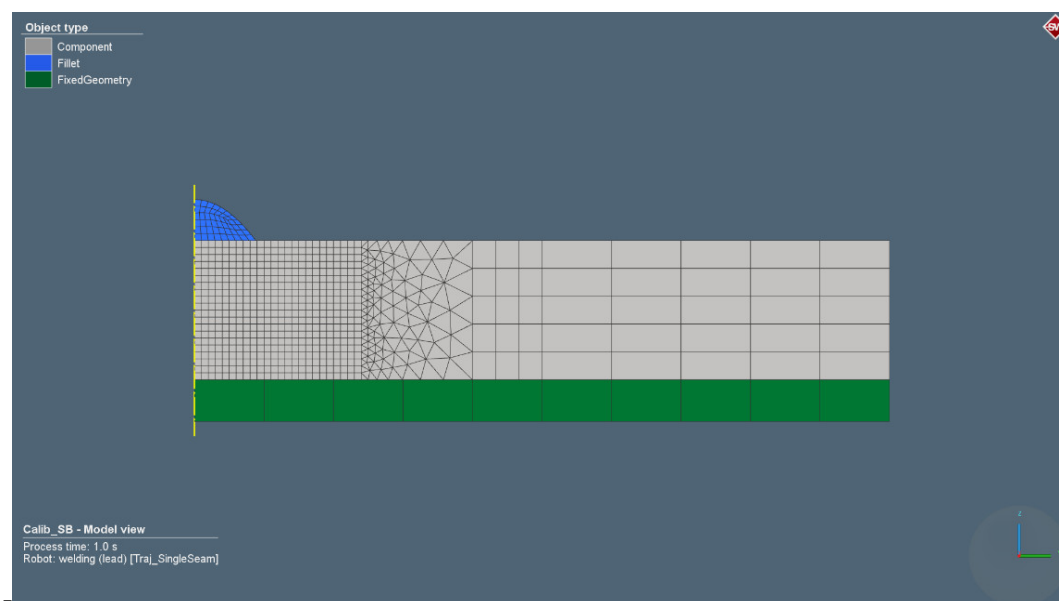

Figure 26. Cross-section view of the calibration model

The support of the baseplate is modelled as fixed geometry. A fixed geometry prevents nodes of the component in contact with the fixed geometry from any movement. This type of boundary condition reduces calculation time compared to a bearing type boundary condition and is for the thermal analysis of the calibration procedure suffice. To increase the resolution and capture the physics happening in the area close to the weld bead without changing the element size in the entire area, adaptive mesh refinement is implemented. Elements around the heat source are refined locally with a global refinement level of one, i.e. elements are subdivided into eight separate elements (Figure 27).
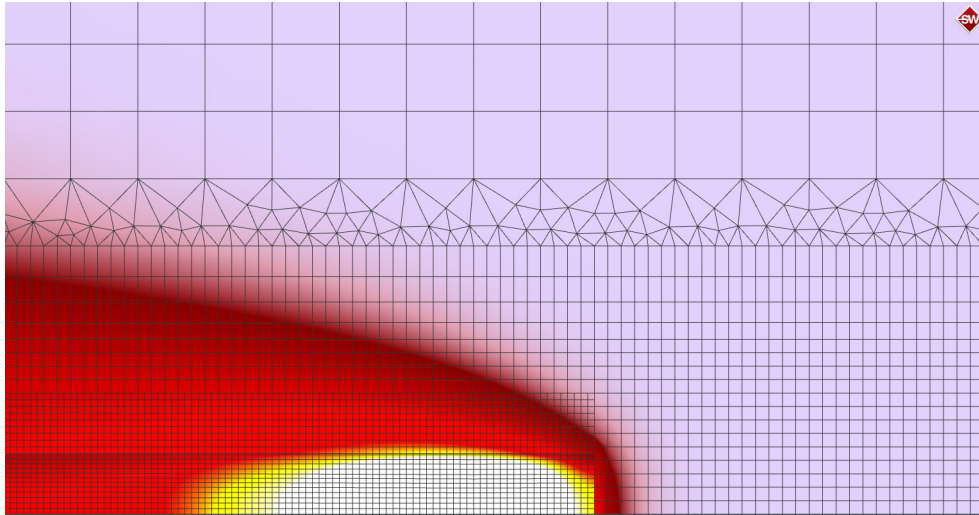

Figure 27: Local mesh refinement based on heat source area criteria

An overview of all processes occurring during the simulation are visualised in the process control centre. Times of present components and robots, welding times, delay times, cooling times and the timing of mechanical boundary conditions are listed therein. The process control centre of the calibration process is schematically shown in Figure 28.

Figure 28: Process control centre of the calibration setup

An overall process time of 400 s is set to capture the cooling behaviour of the assembly and to precisely define the cooling and heat source parameters.

The moving heat source is modelled as a result of a trial and error analysis fitting the shape of the fusion zone and the temperature profiles to the experiment by varying the heat source's geometrical parameters and thermal boundary conditions. The extraction of the weld pool shape from the simulation results is indispensable to determine the heat source parameters according to weld pool shapes. The numerically obtained cross sections are analysed using Simufact's welding monitor (Figure 29).
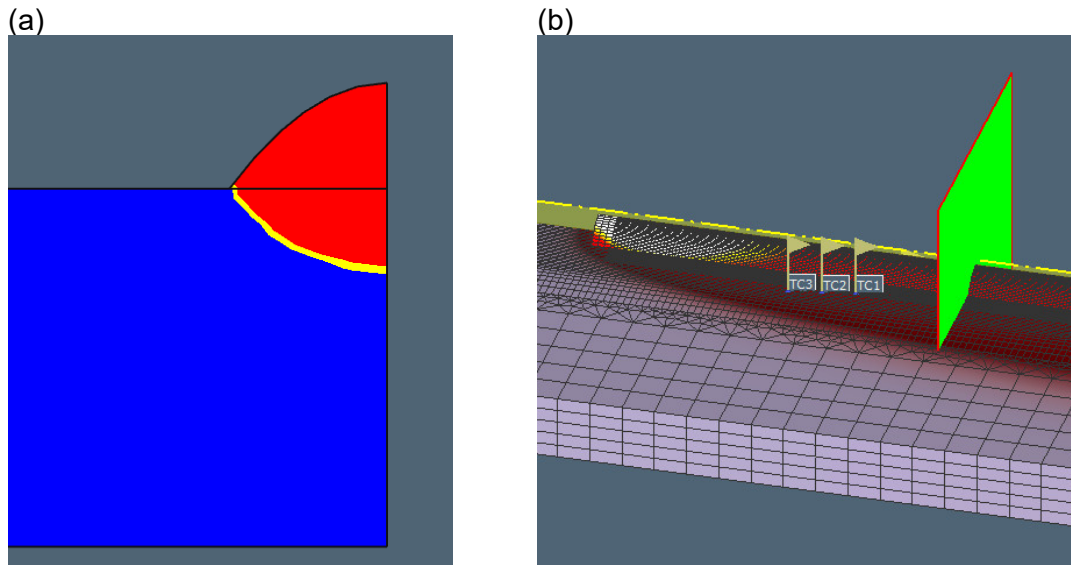
Figure 29: Welding monitor: (a) Cross section; (b) Cutting plane along trajectory

The welding monitor can be used to calibrate the heat source during or after an analysis. It creates a cut along the selected welding trajectory and is placed behind the moving heat source. Moreover, the particles are indicated in Figure 29. They represent the thermocouple locations and are used to derive the thermal profiles from the simulation. The molten pool dimensions obtained from the metallurgical analysis are used to define the geometrical parameters of the Goldak double ellipsoid heat source. Width b and depth d are directly obtained from the micrographs of the cross-sections of the weld pool shapes. The front length a_{f} and rear length a_{r} are estimated by the following rules given by Simufact [33]

$$
\begin{aligned}
a_{\mathrm{f}} &= b \,, \\
a_{\mathrm{r}} &= 2\,b \,.
\end{aligned}
$$
(5.3)

The initial heat source parameters for the trial and error analysis of the calibration procedure are presented in Table 10 and Table 11.

Table 10: Initial heat source parameters for the preheating pass

a_{f} [mm]	a_{r} [mm]	b [mm]	d [mm]	M [-]	f_{f} [-]
3.17	6.34	3.17	1.55	0	0.66

Table 11: Initial heat source parameters for the printing pass

a_{f} [mm]	a_{r} [mm]	b [mm]	d [mm]	M [-]	f_{f} [-]
6.72	13.44	6.72	4.41	0	0.66

Besides the definition of heat source parameters, thermal boundary conditions have to be specified, i.e. the cooling behaviour of the component. The thermal boundary conditions are described by a convective heat transfer coefficient h, a contact heat transfer coefficient a and a coefficient of radiation ε. To assess how these parameters affect the thermal simulation and to limit the possible value set, a parameter study is conducted in Appendix C - Numerical parameter study. With this approach, it is intended to reduce iterations of different parameter

combinations and calculate with relevant parameters in the first place. The welding parameters are presented in Table 12.

Table 12: Welding parameters for the heat source calibration

Run	I [A]	U [V]	v_{TS} [mm/min]
Preheating	130	25	300
Deposition	140	25	200

5.2 Single wall model

To determine the cross-section profiles of the fabricated Ti-6Al-4V walls, demonstrator 3 is exemplary cut in two halves using WEDM. The cut surface of one half is then scanned with an Alicona Infinite Focus optical 3D measurement system. The 3D point cloud obtained is analysed and edited in MATLAB 2016a. From the three-dimensional data points a two-dimensional projection of the cut surface is computed. Points defining the boundary of the surface are determined and exported to SolidWorks 2018. Within the CAD software the imported pointes are connected using spline interpolation to reconstruct the cross section of demonstrator 3. The 2D surface scan of the cross section and the reconstructed cross section are shown in Figure 30.
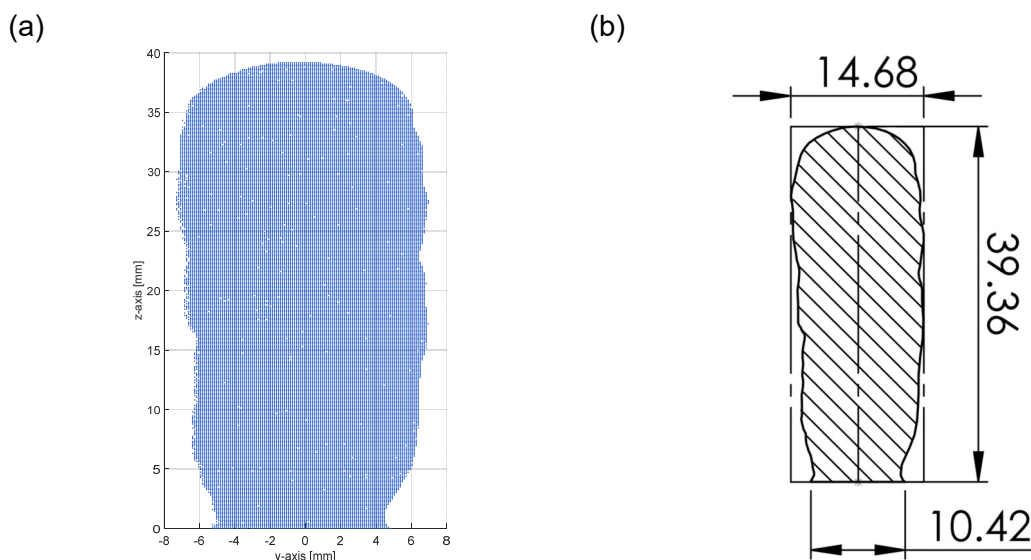
(a) (b)

Figure 30: (a) Point cloud derived in MATLAB; (b) Derived CAD model within SolidWorks

In this study, each welding seam is considered as rectangular cross section. This approach reduces model complexity and enables engineers to set up simulations faster. For components with more complex geometries, the implementation of detailed weld beads increases the modelling effort. Moreover, the exact geometry of the weld beads is not always known. Some numerical studies considered each welding seam as rectangular cross section yielding good results [18], [46]. To determine the rectangular cross-section profiles, area and height of the wall are divided by the total number of deposited layers. The dimensions used for the determination of the rectangular layer geometry are summarised in Table 13.

Table 13: Cross-sectional dimensions of demonstrator 3

Total area [mm²]	Total wall height [mm]	Number of layers [-]
498.15	39.36	32

From Table 13, the cross-sectional area and layer height for each deposited layer are determined as 15.58 mm² and 1.23 mm, respectively. The wall width of each layer is the result of the cross-sectional area divided by the layer height yielding 12.67 mm. An overview of the layer geometry is presented in Table 14.

Table 14: Layer dimensions

CSA [mm²]	Layer height [mm]	Wall width [mm]
15.58	1.23	12.67

The cross-sectional area of each deposited layer determined from the deposited wall is in good agreement with the cross-sectional areas determined from the metallographic analysis (compare Table 7, Table 8, and equation ((5.1)). With these parameters the 3D model of the deposited wall is reconstructed in a layer-wise fashion. A model view of the plasma metal deposition process is shown in Figure 31.
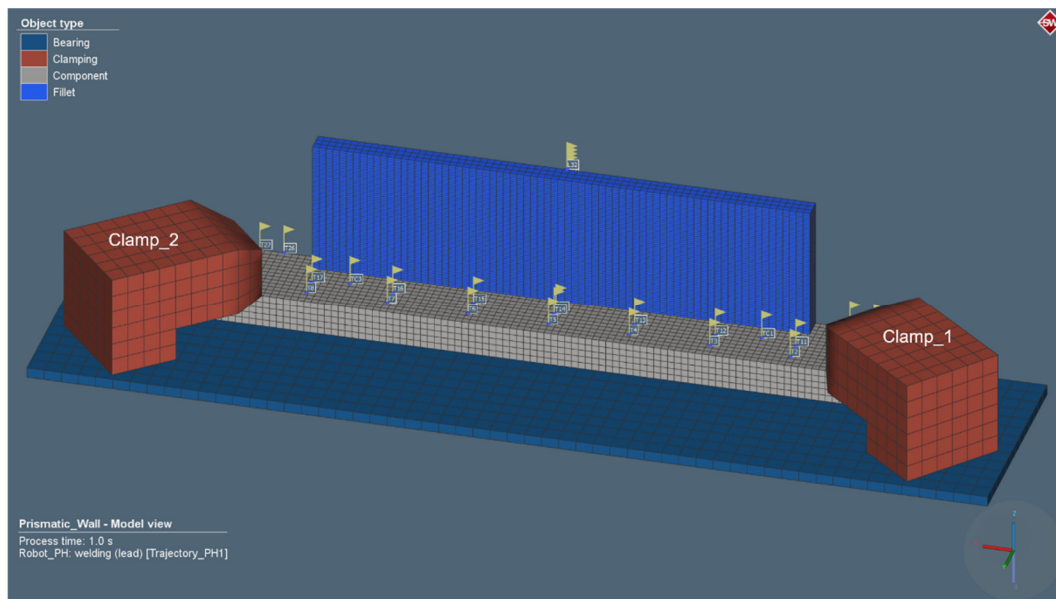

Figure 31: Half-symmetry model of the PMD process

The backing plate is modelled as a bearing. This type of boundary condition enables separation and sliding of components in contact with the bearing and prevents nodes of components in contact with the bearing from movement into the bearing. The clamping concept of the deposition experiments outlined in chapter 4 is implemented in the simulation using simplified models of the clamps. In Simufact Welding, clamps work as springs applying a force opposite to a movement normal to the surface depending on the size of the displacements. Additionally, clamps are pressing components against each other. The clamping movement is controlled via a stiffness and a force. The stiffness is estimated 3,837 N/mm and the clamping force 67,635 N. The estimation of these parameters is

explained in detail in Appendix D - Mechanical boundary conditions. For the plasma metal deposition model, linear hexahedral elements of type C3D8R are used for the thermo-mechanical simulation. The baseplate and the layers are meshed with a global element size of 2 mm, the backing plate and the clamps with a global element size of 5 mm. Each layer is additionally seeded with two elements over the layer height. The overall mesh consists of a total number of 21,820 elements and total number of 39,406 nodes. To trace result values at certain positions in the model, particles are defined at coordinates corresponding to the measurement grid used for the distortion measurements and to the thermocouple locations. In addition, particles are placed along the geometric centreline of the wall ranging from the bottom of the baseplate to the top layer. The results of the tracking points are used to compare the numerical data with the experiments.

Within the robot menu in Simufact Welding different timings of the welding process can be adjusted. This enables a close to reality integration of sequences of the welding process from the G-code directly into the simulation. The exact timings for preheating and layer deposition are shown in Figure 32.
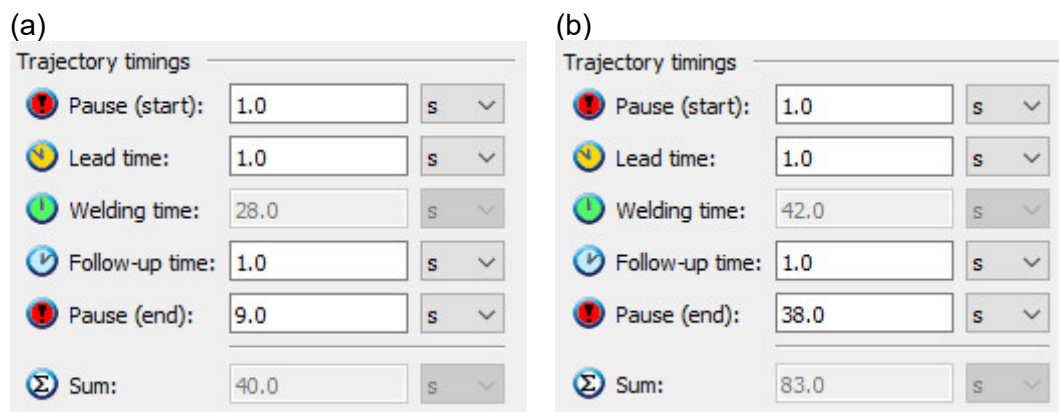

(a)

Trajectory timings			
Pause (start):	1.0	s	∨
Lead time:	1.0	s	∨
Welding time:	28.0	s	∨
Follow-up time:	1.0	s	∨
Pause (end):	9.0	s	∨
Sum:	40.0	s	∨

(b)

Trajectory timings			
Pause (start):	1.0	s	∨
Lead time:	1.0	s	∨
Welding time:	42.0	s	∨
Follow-up time:	1.0	s	∨
Pause (end):	38.0	s	∨
Sum:	83.0	s	∨

Figure 32: Trajectory timings: (a) Preheating; (b) Deposition

The pause time in the beginning considers a delay time to purge locally with argon (no energy input), while the lead time considers a delay with an active heat source to melt the material at the start point. Within the lead time the feed of the wire is initiated. During the first two sequences there is no movement of the heat source. The welding time is automatically calculated by Simufact as the quotient of trajectory length and welding speed. At the end of the trajectory the movement stops, but the heat source is still active. This time period is called follow-up time. The cooling time between layers for preheating and printing was set to 1 s and 30 s respectively, which yielded together with the travel movements of the gantry to the park position a total dwell time of 9 s and 38 s between subsequent layers (no energy input).

On the basis of the experimental trials, the time frame for depositing the walls and cooling down to room temperature is known. As a result, the total simulation time is set to 4,000 s. To investigate the behaviour of the wall upon clamp release, the model is computed using three different strategies for unclamping. Figure 33 schematically shows the individual clamp release times.
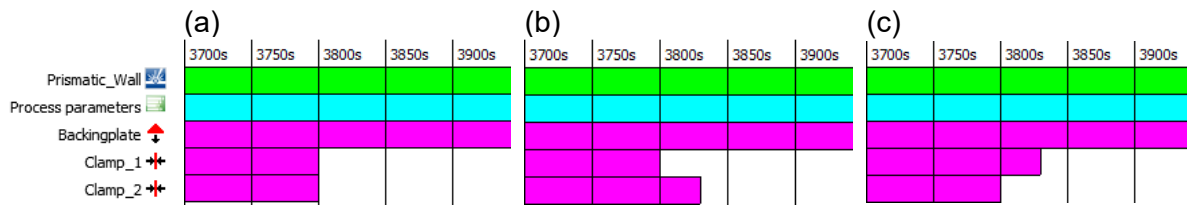
Figure 33: Process control centre indicating clamp release times: (a) Simultaneous unclamping; (b) Clamp 1 followed by clamp 2; (c) Clamp 2 followed by clamp 1

The delay time for non-simultaneous release of clamp 1 and clamp 2 and vice versa is set to 30 s. This time interval approximately corresponds to manual release of the clamps after the deposition process.

5.3 Aerospace bracket model

Finally, a common connecting element or fastening element in the aerospace industry is analysed. Aircraft brackets are essentially supported structures that are used to attach two different components while supporting one over the other. Redesigning brackets for AM can result in significant reduction of material costs, reduced mechanical post processing, weight savings and can decrease fuel consumption of airplanes. The 3D model of the to-built geometry and the part after machining are schematically shown in Figure 34.
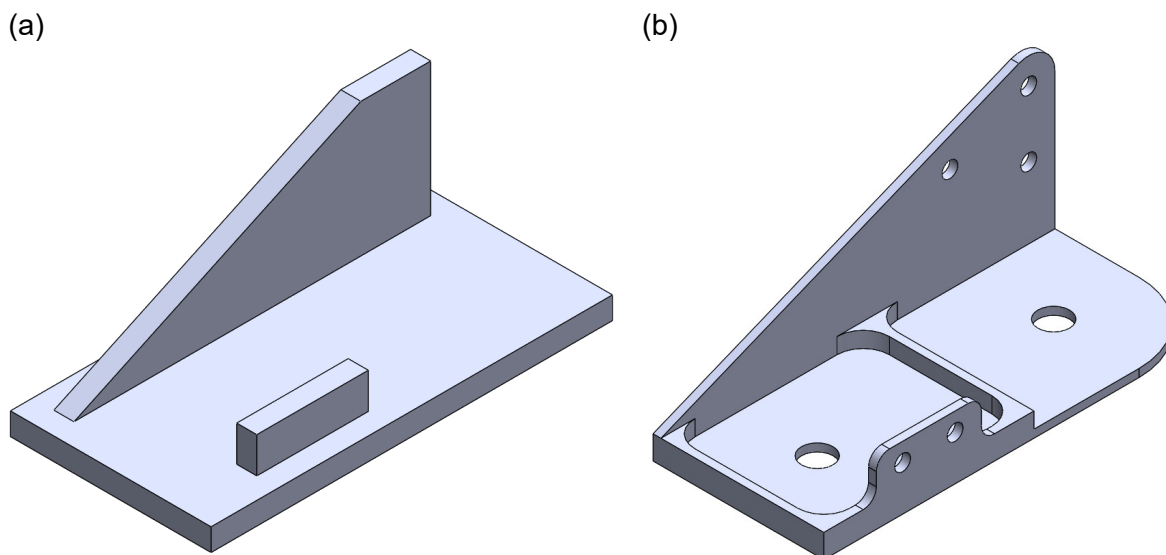

Figure 34: 3D model of the bracket in the (a) as-built condition and (b) after final machining

Figure 34 (a) shows that the to-built geometry is oversized in order to incorporate the final geometry and to take into account the material loss due to mechanical postprocessing. From this CAD file the building strategy for the PMD process is derived. The part consists of two single walls deposited on a rectangular Ti-6Al-4V baseplate. The walls are built up layer by layer until a pre-defined height is reached. The goal is to determine the optimal building strategy by using numerical simulations to minimise distortion and reduce residual stresses. Two building strategies are investigated: firstly, the small wall is deposited followed by the subsequent deposition of the inclined wall and, secondly, a layer of the small wall is followed by a layer of the inclined wall. Both strategies are based on bidirectional layer deposition. The baseplate is fixed to the backing plate of the welding chamber with two clamps. Prior to deposition, the cold baseplate is preheated with the arc to improve bonding of the first layers to the baseplate. A model view of the bracket is shown in Figure 35. The set-up allows no exploitation of symmetry properties.
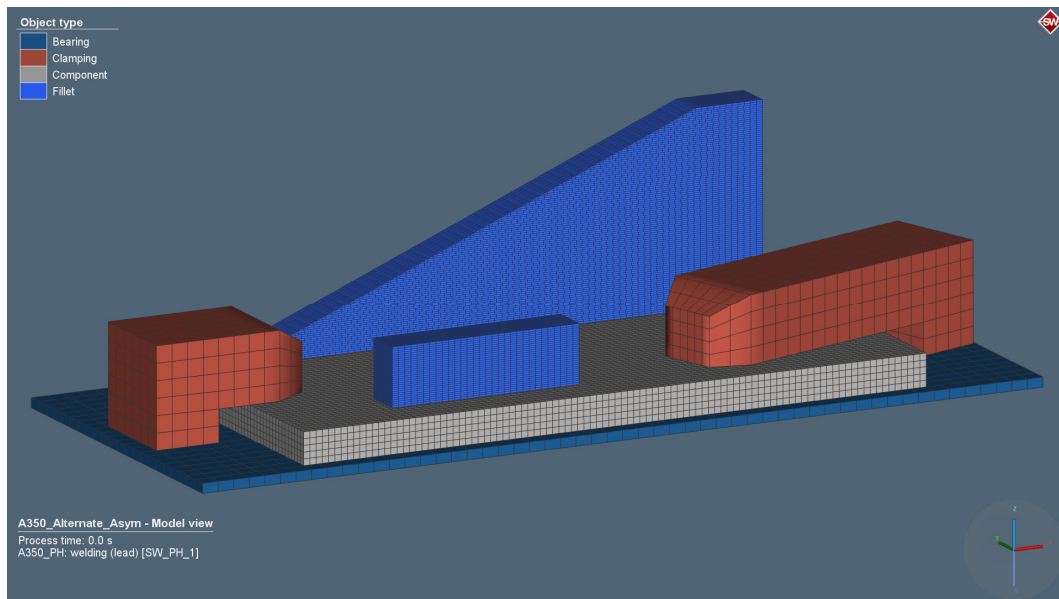
Figure 35: Model view of the airplane bracket

Linear hexahedral elements of type C3D8R are used for the thermo-mechanical simulation. The baseplate and the walls are meshed with a global element size of 2 mm, the backing plate and the clamps with a global element size of 5 mm. Each layer is additionally seeded with two elements over the layer height. The overall mesh consists of a total number of 61,612 elements and total number of 96,450 nodes. The deposition parameters for the fabrication of the bracket correspond to the parameters utilised for the additive manufacturing of the single wall structures in chapter 5.2. The dwell time between layers is estimated 6 s which corresponds to the time needed for the gantry to travel from the end position of the current layer to the start position of the subsequent layer. The total simulation time is set to 3,600 s. Clamps are released simultaneously after 3,540 s. Accordingly, the results achieved are used to elaborate an optimal building strategy for the process to demonstrate the practicability of numerical simulations on an industrial scale.

6 Results

In this section, the experimental and simulation results are presented, whereas the experimental results from the plasma metal deposition process are given first. Afterwards, the calibration procedure for the thermo-mechanical simulations is discussed and finally, the numerical model of the single wall and aerospace bracket model are reviewed.

6.1 Ti-6Al-4V single wall structures

A series of eight single wall structures are fabricated using a plasma-based direct energy deposition process. As material of interest an α/β titanium alloy (Ti-6Al-4V) is investigated. Multi-layer walls are deposited along the centreline of the baseplate with reversed welding directions for each layer. Each wall consists of 32 layers. Average wall height and average maximum wall width measured at the centre of the deposited walls are 37.47 ± 0.98 mm and 13.30 ± 0.45 mm, respectively. The average mass of the single wall structures is 300 ± 11 g. The total layer height divided by the number of layers yields an average layer height of 1.17 ± 0.03 mm. An example of a Ti-6Al-4V wall built by plasma metal deposition can be seen in Figure 36.
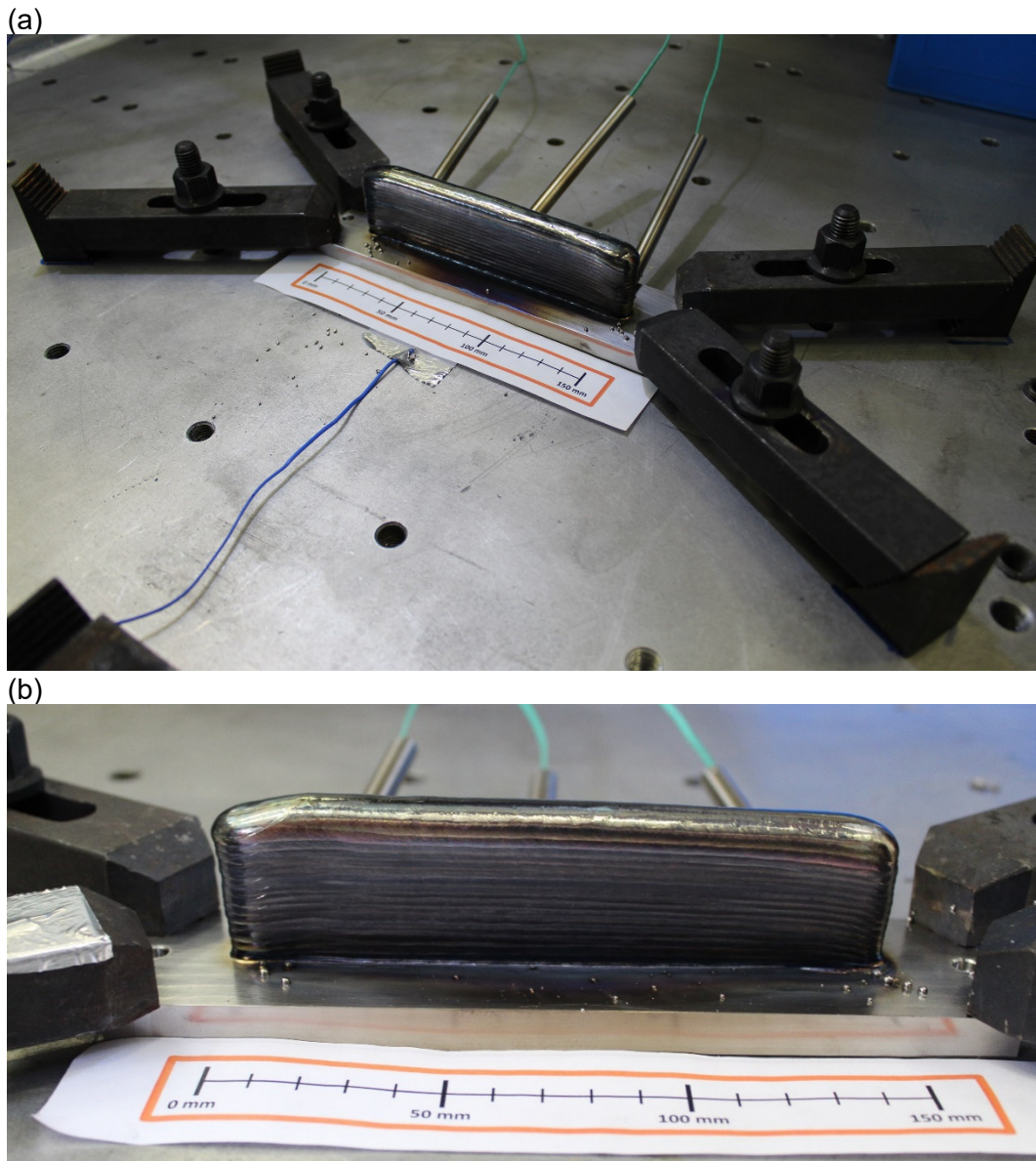
(a)

(b)

Figure 36: Ti-6Al-4V single wall structure produced with plasma metal deposition

All demonstrators have a silver colour which is a sign of proper shielding against atmospheric contamination. The surface discoloration of Ti-6Al-4V can be used to visually assess the degree of oxidation. With increasing oxidation the surface colour changes from metallic silver, light straw through dark straw, light blue, dark blue, to grey and powdery [47]. Further visual assessment reveals an increase in wall width along the build height. This observation is also confirmed by measurements of the layer height and wall width during deposition. The layer height and the maximum wall width (considering the surface waviness of the weld) are measured with a calliper after the 10th, 20th and 32nd layer at the centre of the wall. Since manual recording of measurement data inside the welding chamber is quite laborious and to not interrupt the continuity of the process, measurements are only conducted at a few points. Data for the first layer are taken from the calibration experiments (Table 8). The layer height and wall width along the build height can be seen in Figure 37.
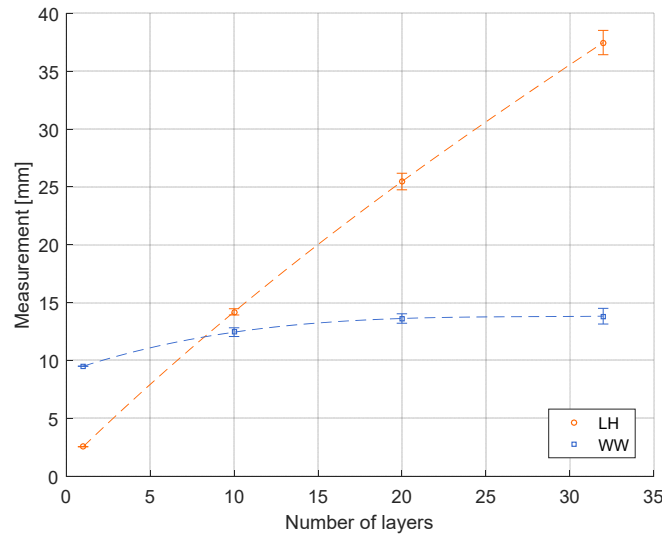
Figure 37: Layer height and wall width measured during deposition

Figure 37 shows that the layer height increases nearly linearly with increasing wall height. The width of the cross section, on the contrary, experiences a steady increase from the first layer, reaching a steady deposition width at higher layers. This geometry related phenomenon can be explained by the balance of heat input and dissipation. In the first few layers, the thermal effect of the baseplate leads to a reduction in wall width and an increase in layer height. This effect has been observed by Martina et al.[21], [37] and described by Wu et al. [47]. The thermal history of WAAM components is governed by a balance between conduction, convection, and radiation. As reported by Wu et al. [47], the cold baseplate acts as a heat sink in the first layers, leading to faster cooling rates and thus narrower beads. Convection and radiation become more significant with the component being built up layer by layer. With an increasing wall height, the conductive thermal resistance to the baseplate which heats up during the deposition process, is increased. Despite titanium being a poor thermal conductor, convection and radiation are less effective than conduction. The molten pool dissipates heat at slower rates and, therefore, wider beads can be observed with increasing wall height until the heat dissipation and heat input reach a balance resulting in steady wall widths. For a more precise evaluation additional measurement data are required. The results shown, however, reflect the balance of energy input and dissipation as a geometrical boundary condition well and give insight into the development of the cross sections of deposited walls at constant deposition parameters. To achieve consistent geometrical dimensions, i.e. WW and LH, throughout the whole AM process, the building strategy must be adopted accordingly. For the sake of simplicity, all layers have been built with the same set of parameters and consistent building strategy.

6.2 Weld bead shape

As mentioned in chapter 4.2, preheating is implemented to avoid the first track to become too narrow and to prevent separation from the baseplate. Bonding of the liquid molten pool to the baseplate can be explained by the contact angle at the interface between the solid, liquid and vapour phase. The wetting angle is the main characteristic of the interphase of the three phases. The presence of solid-liquid-vapour interfaces and related interfacial phenomena play an extremely important role in high temperature processes, such as welding. Deposits of droplets of fed wire form a drop of liquid metal at the interface of the baseplate. The shape of the droplet is directly linked to the process parameters and a competition between volumetric

forces, such as gravity or electromagnetic forces, and interfacial phenomena, such as surface tension or drag forces [48]. These phenomena combined with heat and mass transfers define the shape of the weld pool and, thus, the final quality of the welding operation. To acquire information on the spreading of the molten material on the baseplate, the wetting angles of the printing pass and the printing pass with preceding preheating are analysed (Figure 38).
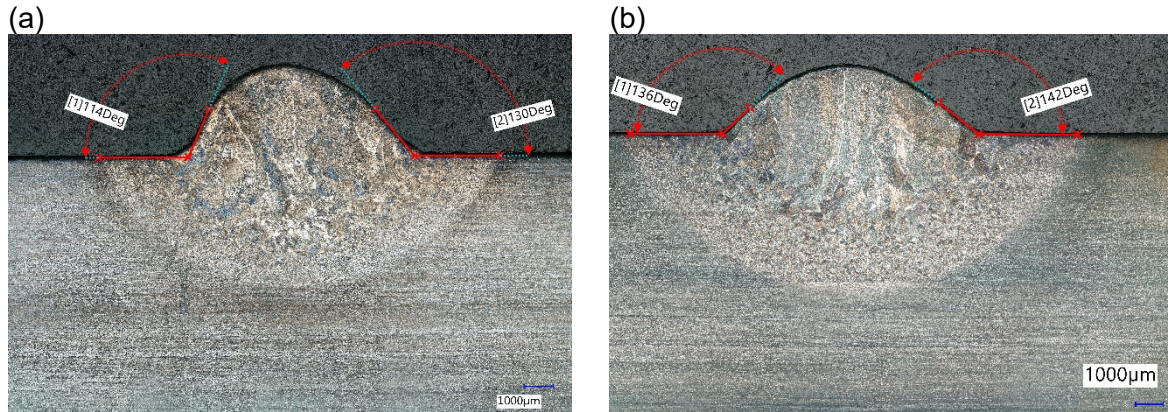

Figure 38: Complementary wetting angles: (a) Single bead; (b) Single bead with two preceding preheating passes

The corresponding wetting angles of the left θ_{left} and right θ_{right} side are shown in Table 15.

Table 15: Wetting angles

Calibration	θ_{left} [°]	θ_{right} [°]
Single Bead	66	50
Single Bead plus preheating	44	38

The inequalities between left and right side of the beads result from the transverse feeding direction of the wire. The wire feed droplets push the liquid material outwards on the opposite side resulting in steeper wetting angles. Furthermore, it can be observed that preheating results in smaller wetting angles, thus increasing the wettability of the molten material to the baseplate. The formation of various weld-shape defects, such as undercuts (wetting angle greater than 90), lacks-of-fusion, lacks-of-penetration, can be related to the wettability of solid metal by metal melt [48]. Additionally, the shape of the deposited bead and the minimum possible thickness of the deposited metal are related to the value of the wetting angle. It can be concluded that preheating of the baseplate before the welding process, either by hot plasma gas or by means of heating mats, has beneficial effects on the interlayer connection between the first layer and the baseplate.

6.3 Heat source calibration

The calibration procedure consists of three separate experiments – a preheating pass, a single bead, and a single bead with two preceding preheating passes. The moving heat source is modelled as a result of thermal analysis fitting the shape of the fusion zone and the temperature profiles to the experiment by varying the heat source's geometrical parameters and thermal boundary conditions. When modelling the heat source as prescribed heat input, the power distribution of the physical heat source is imitated. The heat input from the energy source is essential to perform accurate simulations of the welding process. The parameters of the Goldak double ellipsoid heat source for preheating and printing obtained by trial and error analysis are shown in Table 16.

Table 16: Goldak double ellipsoid heat source parameters

Run	a_f [mm]	a_r [mm]	b [mm]	d [mm]	M [-]	f_f [-]
Preheating	2.85	5.70	2.85	1.4	0	0.66
Deposition	6.72	13.44	6.72	4.41	0	0.66

The cooling behaviour and arc efficiency are determined by inverse simulation. From this, an arc efficiency of 0.4, an emissivity of 0.7, a convective heat transfer coefficient of 8 W/(m²·K) and a contact heat transfer coefficient of 10 W/(m²·K) are obtained. The parameters for the thermal boundary conditions are assumed to be independent of the temperature. A summary of the welding parameters is presented in Table 17.

Table 17: Welding parameters

Run	I [A]	U [V]	v_{TS} [mm/min]	η [-]	E_l [J/mm]
Preheating	130	25	300	0.4	260
Deposition	140	25	200	0.4	420

6.3.1 Weld pool shape

The heat source model is an important part when carrying out simulations of welding processes. The geometrical fit between the simulated and measured weld pool is achieved by applying the calibration process. During calibration, the heat source model parameters, such as weld penetration and weld width are changed and fine-tuned with the aim of attaining the best fit with the measured weld pool size. A visual comparison can be made through the weld profiles obtained by simulation and experimentation, as presented in Figure 39. The boundary between the modelled fusion zone is defined by the temperature at which the Ti-6Al-4V undergoes solidification. This temperature is 1,550 °C accordingly.
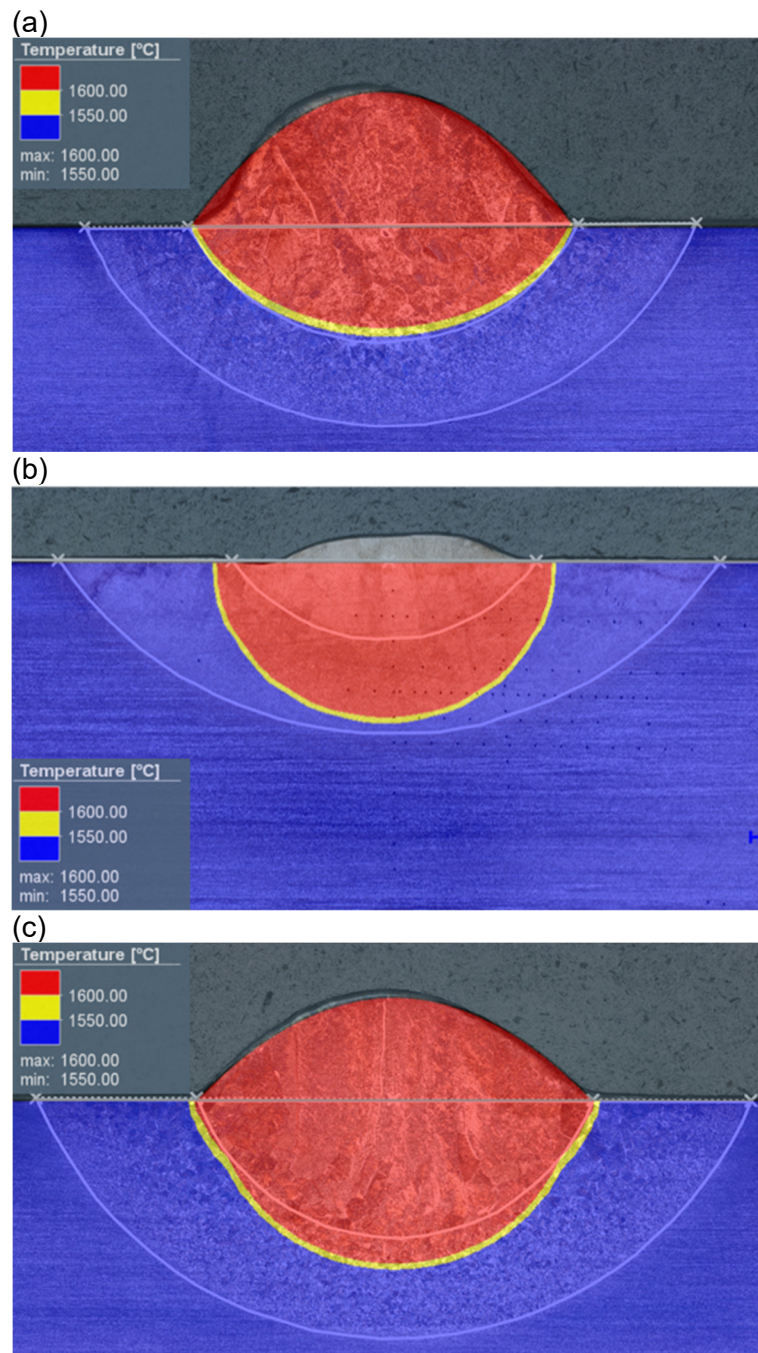
Figure 39: Comparison of FEM calculated and experimental micrographs for (a) a single bead, (b) for preheating and (c) for a single bead with preceding preheating

Since the experimental fusion zone of the single bead is used to determine the numerical heat source's geometrical parameters, this zone is fairly accurately reproduced by the simulation, as seen in Figure 39 (a). Note that although the computed fusion zone is calibrated to match the experimental one, the computed heat source underestimates slightly the penetration depth. As can be seen in Figure 39 (b), the numerically calculated fusion zone for preheating overestimates the experimentally determined weld pool. Although designing the numerical heat source 10 % smaller than the experimental weld pool geometry, as proposed by Goldak et al. [32], the fusion zone is still overestimated. It should be noted that the simulation does not consider any fluid flows of the molten pool. Visual assessment of the micrograph in Figure 39 (b) reveals that the liquid metal is drawn downwards in the peripheral areas while it is forced upwards towards the centre. Molten pool movements indeed affect the melting

process in various ways including the weld pool geometry, heat flow, temperature and temperature gradients. Considering Figure 39 (c), it can be observed that the simulation overestimates the penetration depth of the weld pool. Most likely, this is related to the oversized preheating fusion zone and its energy input into deeper areas of the baseplate than experimentally determined. The ratio of molten pool width and molten pool depth $\phi = 2b/d$ gives an indication of the development of the weld pool geometries - the higher the ratio, the flatter and wider the molten pool:

Table 18: Molten pool ratio

	PH	SB	SB plus PH
Experiment	4.06	3.31	3.03
Simulation	2.22	3.67	2.45

Comparing the experimental molten pool ratios presented in Table 18, the ratio for preheating is significantly larger than for the single beads. In the case of a preheating pass no filler material is added and the molten pool flow is mainly caused by forces based on surface tension gradients in the melt. Thereby, liquid metal is transported from the centre of the weld pool towards the boundaries creating a wide and flat molten pool as can be seen in Figure 39 (b). The ratio of the single bead with preceding preheating is slightly lower than the single bead ratio without preheating indicating higher weld penetration. Except the numerically determined molten pool ratio for preheating, the molten pool ratios of the single bead and the single bead with preheating well reflect the trend of the experimental values. Considering the single bead with preheating, the overestimated weld penetration is affecting the value significantly. In general, it can be deduced from Table 18 that the molten pool ratio decreases with increasing energy input of the heat source causing the fusion zone to get deeper.

6.3.2 Thermal profiles

The thermal models of each calibration experiment are verified by comparing the temperature history results from the measured and calculated data. The temperature development obtained by Simufact Welding 8.0 and the experimental trials are presented in Figure 40, Figure 41 and Figure 42 for the single bead, preheating and single bead with preceding preheating, respectively.
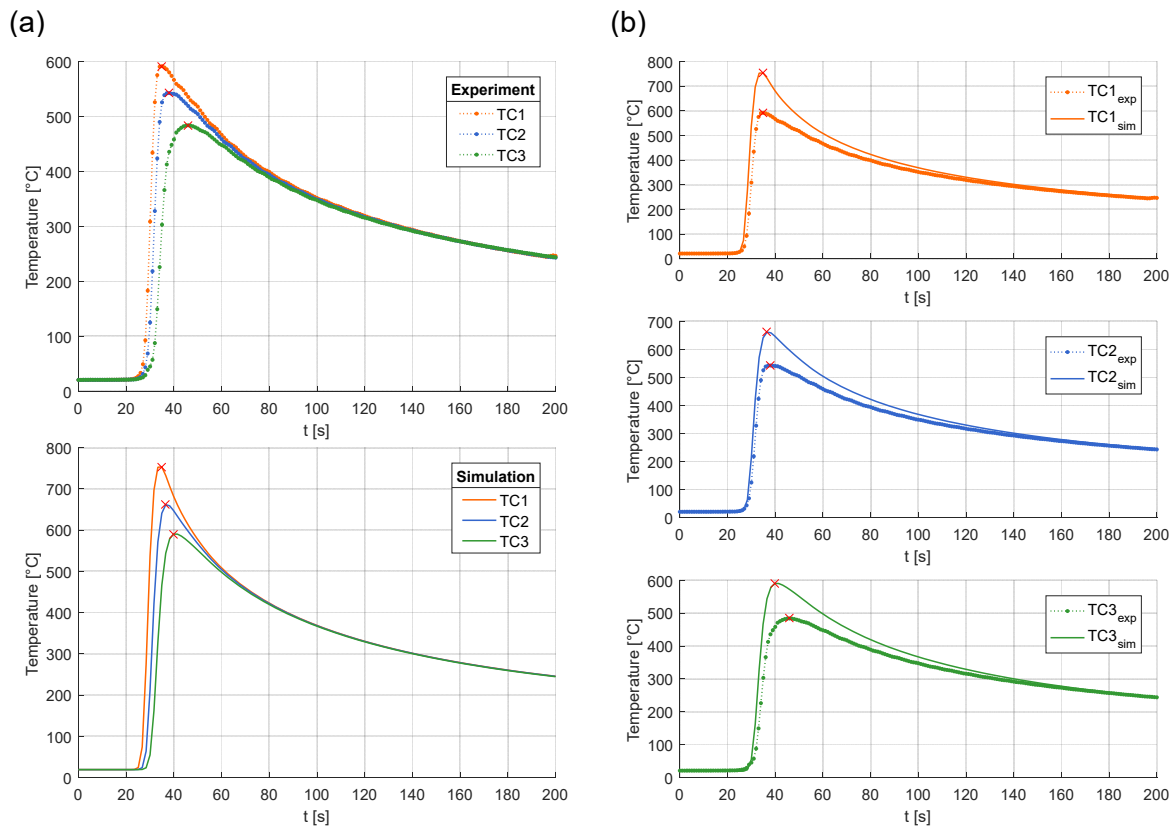
Figure 40: Temperature profiles obtained during single bead deposition: (a) Overview; (b) Comparison

In Figure 40, it can be observed that temperature peaks decrease with increasing distance from the welding trajectory, i.e. depending on the distance from the heat source different temperature-time curves are obtained. Additionally, the cooling speed decreases with increasing distance. After reaching the peak temperature and the heat source moving along its trajectory, the cooling phase starts. With increasing distance, the temperature curves become flatter until the temperature gradients of the different thermocouple locations are balanced. From this point the three different thermocouple locations show the same cooling behaviour and cooling speed. Furthermore, the figures show that the heating rates, heating times and cooling rates obtained by the simulation coincide with the experimental results. The FEA framework gives overall accurate predictions of the temperatures at the thermocouple positions. However, it is observed that the model overshoots the experimentally measured peak temperatures. One assumed reason for these discrepancies is the fact that the temperatures have not been measured at the very tip of the thermocouples and, although using heat conducting paste, the contact has not been optimal. The thermocouples used, however, introduce an uncertainty due to relatively high response times of 0.9 s and a limited sampling frequency of the data logger of 1 s. Therefore, due to the inertia of the measurement system highly dynamic temperature changes cannot be resolved accurately, especially when the heat source passes the thermocouple locations. Aarbogh et al. [49] reported similar discrepancies in their study. Similar time-temperature profiles are observed for the preheating pass, as seen in Figure 41.
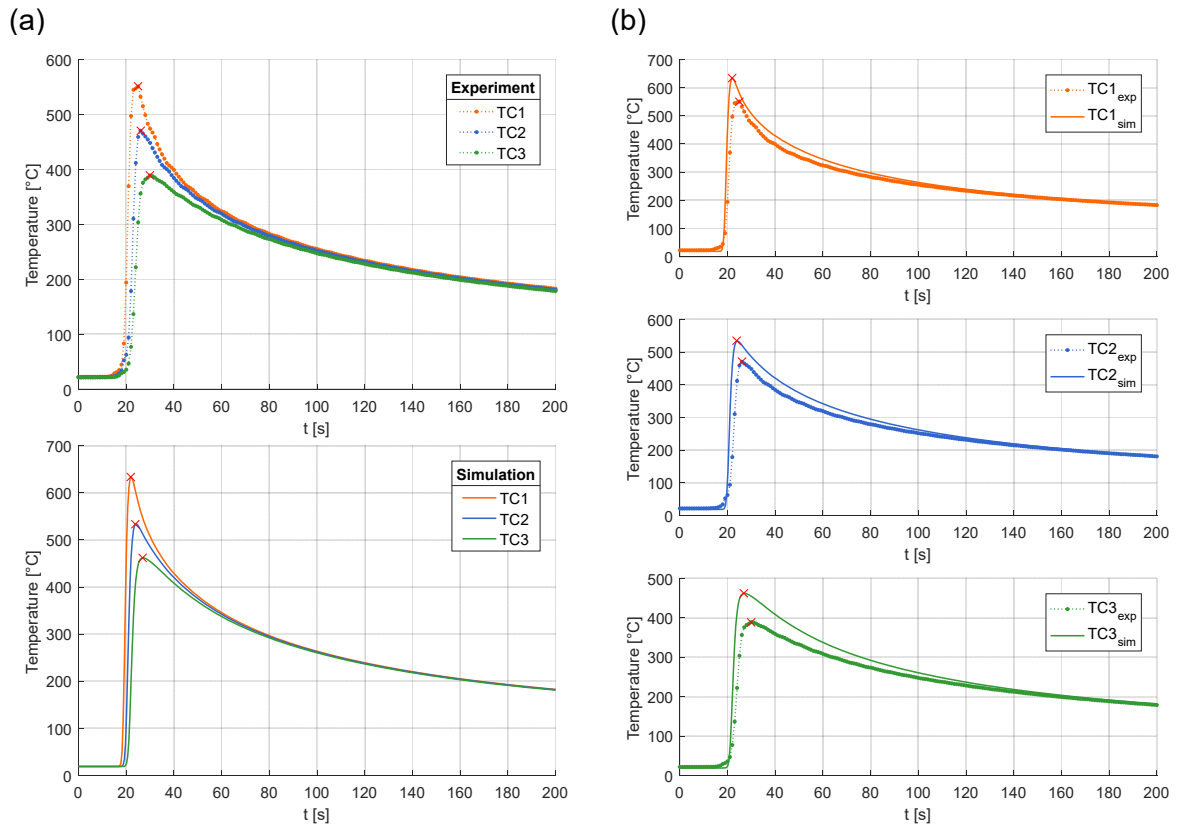
Figure 41: Temperature profiles obtained during preheating: (a) Overview; (b) Comparison

The temperature peaks are not as pronounced as for the single bead due the lower energy input per unit of length. In this case the peak temperatures are also overestimated by the simulation. The cooling behaviour of experiment and simulation equalises about 100 seconds after peak temperatures are reached and stays consistent verifying the selected thermal boundary conditions. Figure 42 shows the temperature profiles obtained during single bead deposition with preceding preheating.
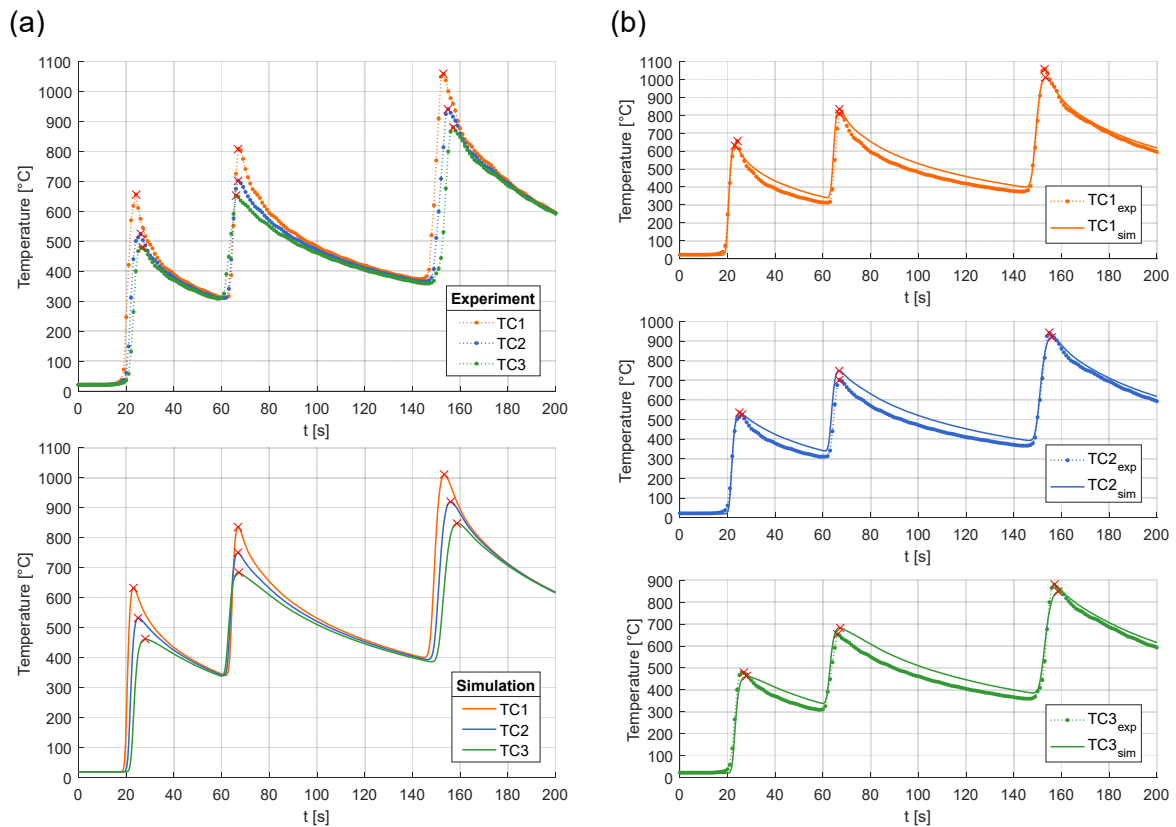
Figure 42: Temperature profiles obtained during single bead deposition plus preheating: (a) Overview; (b) Comparison

The temperature profiles of experiment and simulation are in good agreement. The preheating passes rise the temperature in the weld region to around 400 °C reducing the thermal gradient necessary to enable fusion at the weld interface. The maximum peak temperature measured at TC1 raises above 1,000 °C and is therefore above the β transus temperature of Ti-6Al-4V. The associated change in microstructure is well reflected considering the measurement location of TC1 and the width of the HAZ. The half width of the HAZ determined from the micrographs is 8.385 mm, TC1 is located 8 mm from the centreline. In a single weld bead the final HAZ appears at the position where the peak temperature rise is approximately equivalent to the β transus temperature [50].

6.4 Single wall model

6.4.1 Thermal

The numerical model for the plasma metal deposition of the single wall structures employs the double-ellipsoid heat sources for preheating and depositing obtained from the calibration procedure. The parameters for the thermal boundary conditions are maintained except for the contact heat transfer coefficient. The baseplate is now in contact with the aluminium backing plate. The contact heat loss through the backing plate is determined by running a series of numerical trials and tuning the values so that the predicted temperature profiles match the experimental results. A value of 100 W/(m²·K) gives the best match with the experiments. Figure 43 presents the experimentally measured and numerically obtained temperature profiles during deposition and cooling.
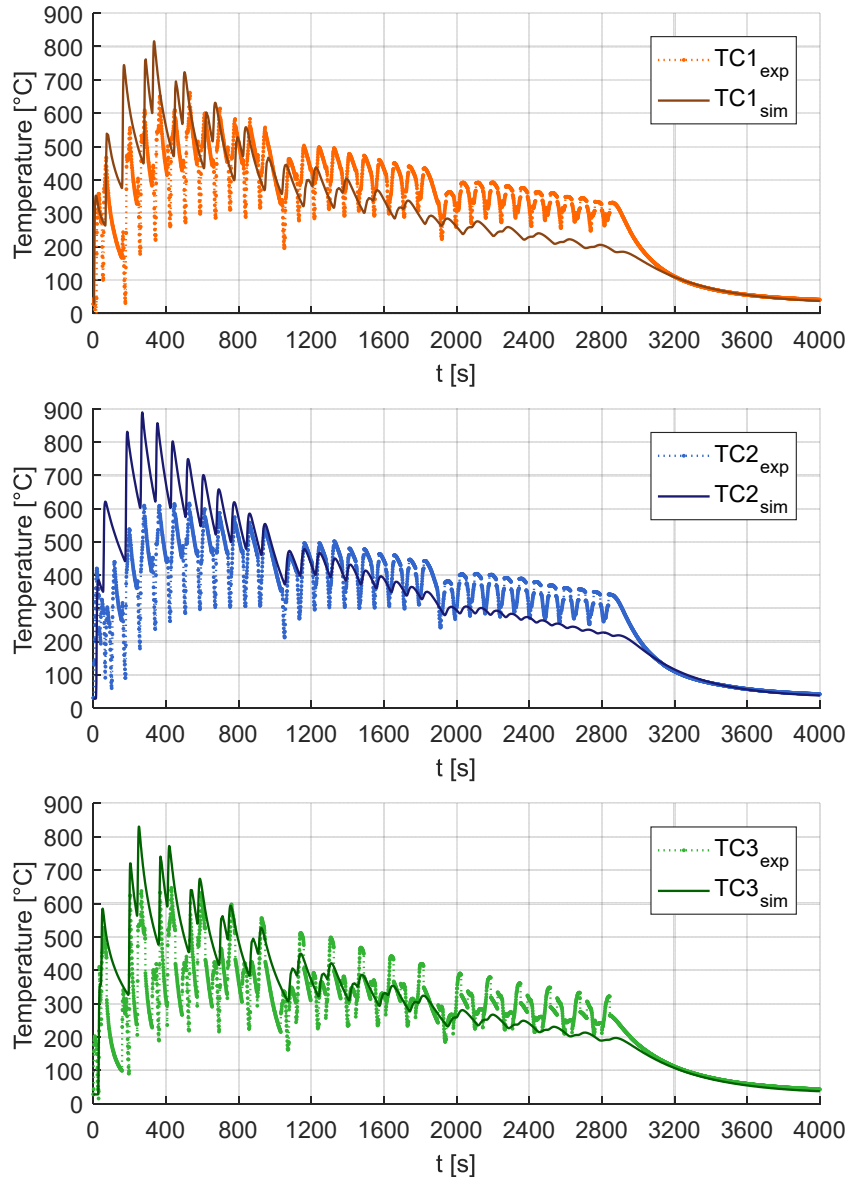
Figure 43: Temperature profiles obtained during single wall deposition

The overall trend of the temperature evolution is well reflected by the simulation. Referring to the calibration procedures, the peak temperatures in the first layers are overestimated. Over the building time, the thermal profiles of the experiment show a less pronounced temperature decrease than the numerical results. A figurative reason is believed to be the pilot arc. During dwell times between layers, the torch travels to its park position with the pilot arc active, thus affecting the cooling behaviour of the deposited wall. The initially assumed free convection is locally disturbed by the hot plasma streams of the pilot. Considering the trajectory timings defined in Simufact for the welding process (see Figure 32), no energy input is defined during the pause time after the end of a trajectory. The cooling curve after the deposition process, however, is well reflected by the simulation indicating that the parameters set for the thermal boundary conditions are accurate. Further, a distinct noise in the experimental measurement signal can be noticed. This may be due to insufficient shielding of the thermocouple against the electromagnetic influence of the plasma.

6.4.2 Mechanical

The mechanical performance of the additive manufactured walls is investigated. The total distortion is an important evaluation index of plasma metal deposited components. Distortion has a strong impact on the dimensional precision. Figure 44 displays measured and numerical post process displacements along the longitudinal direction after cooling and under different cases of unclamping. The course of the displacements between the data points has been modelled using spline interpolation. In the case for y=0 mm at the top surface no data points along the wall are available. Thus, the interpolation between the four remaining points, (x=-89.5 mm, x=-82.5 mm and x=82.5 mm, x=89.5 mm, respectively) serves only as an indicator for the gradient in the out-of-plane distortion between these points and cannot be compared with the other measurement lines at the top surface.
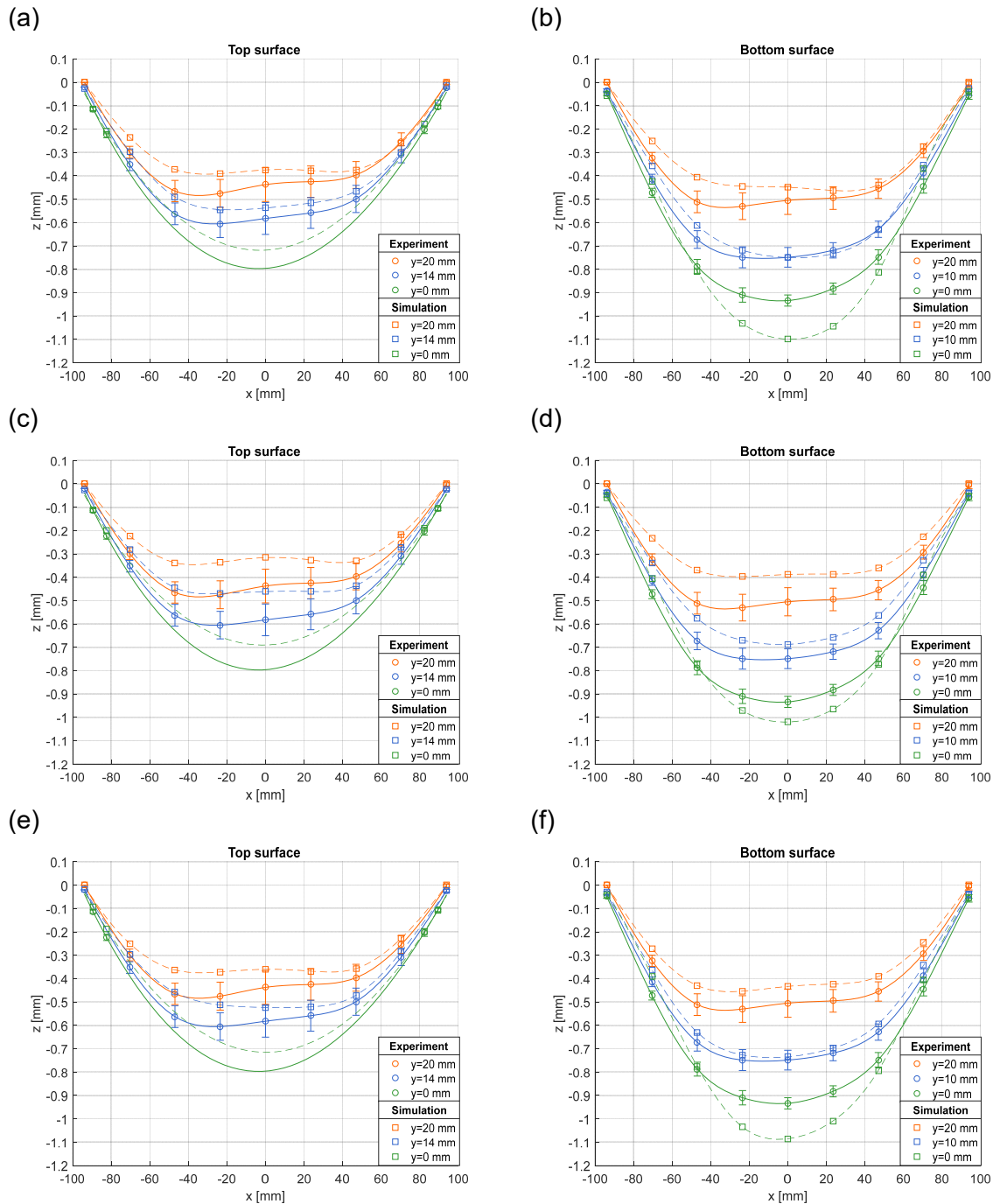
(a)

(b)

(c)

(d)

(e)

(f)

Figure 44: Out-of-plane distortion along the longitudinal direction: (a) and (b) clamp 1 followed by clamp 2; (c) and (d) simultaneous unclamping; (e) and (f) clamp 2 followed by clamp 1

The predicted distortions of all three unclamping cases are compared to the measured distortion. In Figure 44, the downward bending of the baseplate in relation to the reference plane defined in chapter 4.5 can be seen. It should be noted that in recent studies the authors refer to this phenomenon as upward bending, as it is a matter of reference. To stay consistent with their terminology upward bending is further used in this thesis. The upward bending can be explained as follows [19]: the deposited layer expands during heating and contracts during cooling. The contraction of the upper layer is constrained by the previously deposited layers and generates tensile residual stress, resulting in upward bending of the baseplate. Larger distortions are found at the bottom surface. Here, the baseplate bends upwards by

57

approximately 0.9 mm at the centreline of the surface showing the maximum distortion. Comparing the scan lines at y=10 mm and y=14 mm, the top surface shows a less pronounced out-of-plane distortion. The scan lines at y=20 mm show similar values at both surfaces. Another prominent observation from the measured data points is their asymmetrical course over the length of the baseplate. Although a bidirectional building strategy has been employed, already the deposition of the first layer causes non-uniform heating and cooling of the baseplate. As a result of the non-homogenous temperature field, inconsistent thermal expansion of the heat affected zone leads to a non-homogenous plastic deformation triggering the asymmetric behaviour of the baseplate. Although all eight demonstrators have been built with the same process parameters, the CMM points are subject to a certain range of fluctuation. Deviations in the application of the clamping forces, a modified temperature control, influence of the rolling direction of the baseplates, the geometry of the wall - all these factors have an impact on the final distortion of each component.

A graphical evaluation of Figure 44 reveals a qualitative agreement of the modelling results with the measurements, despite representing noticeable smaller deflections. The only exception is the longitudinal distortion along the centreline of the baseplate at y=0 mm of the bottom surface. Here, the numerical results overpredict the distortion. The deviations between experimental and numerical values are strongly linked to the heat input and the mechanical and thermal boundary conditions. Referring to the temperature history plot in Figure 43, the temperature profiles obtained from the simulation decrease at a higher rate over the building time than the experimental resulting in faster cooling. This in turn leads to the material being stiffer, yielding smaller displacements. In the simulation, it is also assumed that the backing plate is rigid and does not allow any penetration of the baseplate. In reality, of course, the aluminium backing plate has a lower stiffness than the titanium baseplate and tends to deform locally elastically and plastically due to mechanical clamping forces exerted on the Ti-6Al-4V baseplate. All these factors are linked to the evolution of the final distortion of the PMD single wall structure. In each of the cases in Figure 44, the numerical results display a similar accumulation of distortion after cooling and unclamping. The case of simultaneous unclamping follows the course of the CMM points for the top and bottom surface most precisely, but shows a high deviation in the residuals. On the contrary, Figure 44 (a), case 1 top surface, approximates the out-of-plane distortion of the top surface best, while Figure 44 (f), case 3 bottom surface, appears to fit the data of the bottom surface best. Error metrics from statistics are used to judge the quality of the models and verify the statements above. The mean absolute percentage error (MAPE) for each case can be calculated as

$$MAPE = \frac{100\%}{n} \sum_{i=1}^{n} \left| \frac{x_i^{\text{exp}} - x_i^{\text{sim}}}{x_i^{\text{exp}}} \right|. \tag{6.1}$$

where n is the total number of data points, i the current data point, x^{exp} is the experimental value and x^{sim} is the simulated value. Table 19 shows the mean absolute percentage error for the top and bottom surface for all three unclamping cases.

Table 19: MAPE for the unclamping cases

Case	Description	MAPE top surface [%]	MAPE bottom surface [%]
1	Clamp 1 followed by clamp 2	12.60	12.57
2	Simultaneous unclamping	15.33	15.23
3	Clamp 2 followed by clamp 1	11.96	11.16

A good correlation is achieved for each case fitting the top and bottom surface in equal measure. Thus, each unclamping strategy is, within numerical and experimental errors, suitable to predict the out-of-plane distortion of the PMD single wall structure. The largest errors are found for symmetric unclamping, while case 3 (clamp 2 follows clamp 1) shows the lowest errors for both, the top and bottom surface. The most prominent observation from these numbers, though, appears to be that the prediction of the out-of-plane distortion of the bottom surface is more accurate than the prediction of the top surface, i.e. the MAPE value of the bottom surface is smaller than the MAPE value of the top surface. Contrary to the expectation that Figure 44 (a) matches the top surface and Figure 44 (f) matches the bottom surface best, the unclamping strategy of case 3 fits according to the MAPE values the measured distortion most accurately. It becomes evident that different unclamping strategies affect the final distortion of the PMD walls. Figure 45 (a) and (b) illustrate the predicted total displacement of the wall after case 3 cooling and unclamping. The distortion of the model has been scaled by a factor of 4 so that the deformation becomes evident and to emphasise the deformation of the baseplate.
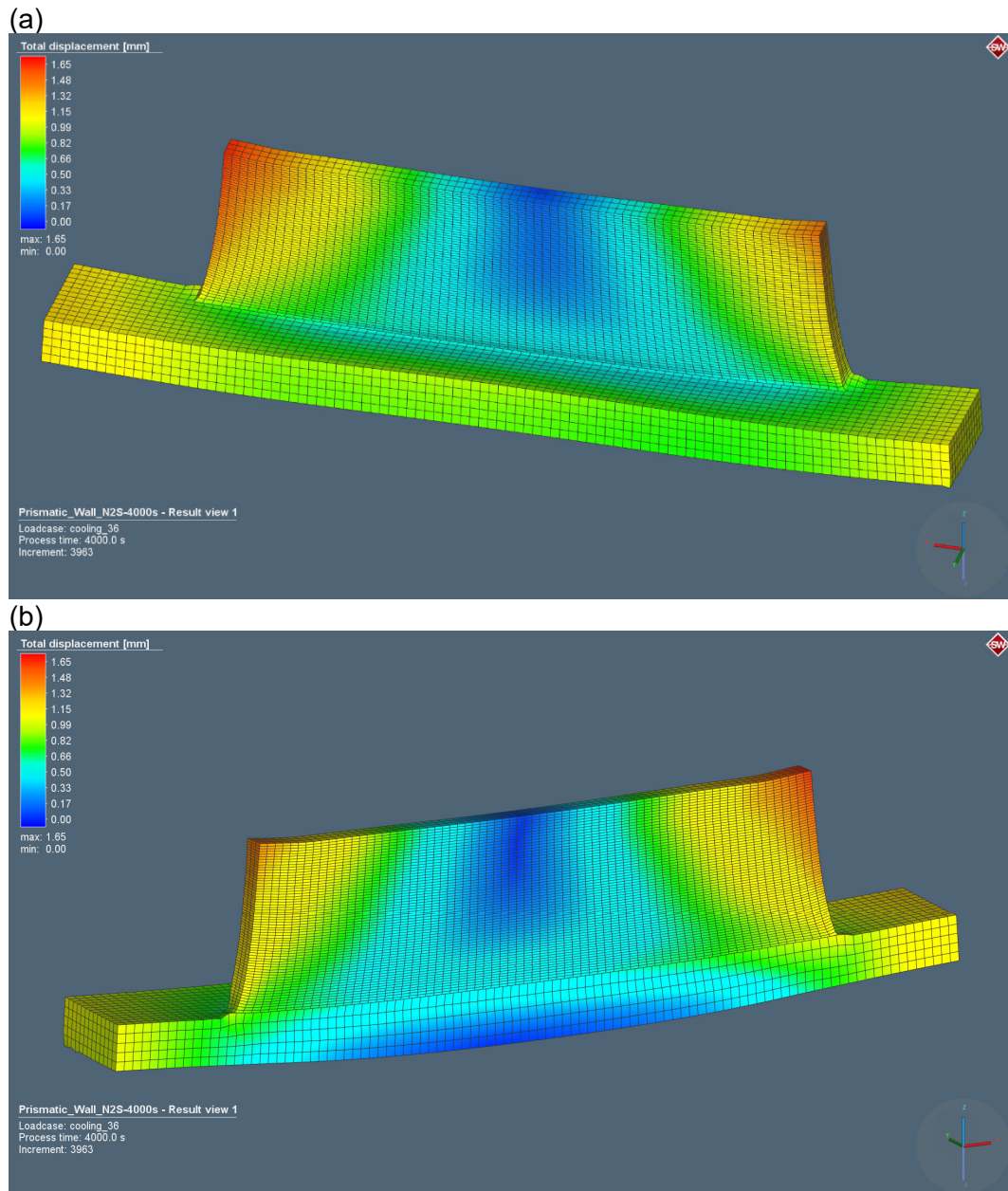
Figure 45: Total displacement of the PMD wall after case 3 cooling and unclamping:
(a) Overview; (b) Symmetry plane

After unclamping and cooling, the component bends upwards and shows significant out-of-plane distortion. The deposition of liquid metal on a solid baseplate and its' constrained shrinkage during cooling causes elastic and plastic deformations. In the central area of the wall distortion is restricted due to the wall itself functioning as a stiffening structure, at the bottom distortion is restricted due to the backing plate. The deposited wall is pulling the baseplate upwards causing a significant residual stress state. The mean normal stress, which is the average of the three principal stresses, for case 3 cooling and unclamping is shown in Figure 46. The mean normal stress of the model has been scaled by a factor of 4.
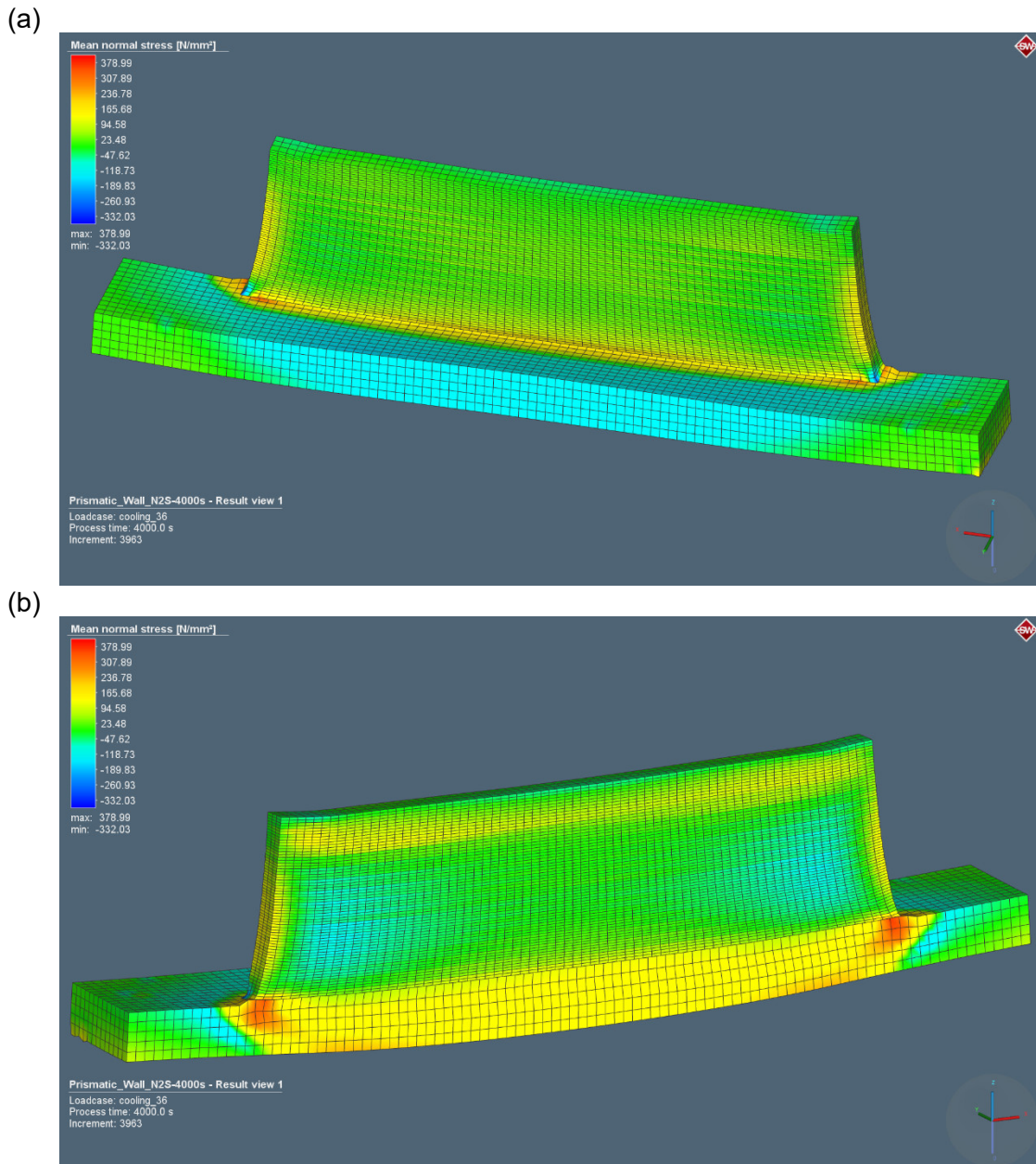
(a)

(b)

Figure 46: Mean normal stress of the PMD wall after case 3 cooling and unclamping:
(a) Overview; (b) Symmetry plane

In Simufact Welding 8.0 the residual stress distribution can be analysed. Most areas of the component are subjected to tensile residual stresses. Compressive stresses occur in the baseplate in an area surrounding the deposited wall and in the mid-outer regions of the wall. Another interesting observation is the stress concentration at the bonding area of the wall to the baseplate. Here, tensile residual stresses reach a maximum making this critical point susceptible to hot cracking and delamination. Such stress concentrations can be identified by the simulation and incorporated into strategies to avoid tearing or delamination of the deposited material. Due to thermal effects inherent to plasma metal deposition, in-process and post-process distortion and residual stresses are unavoidable. Dimensional and shape changes can be used to identify the effects of resulting residual stresses. The residual stress distribution along the centreline of the additive manufactured wall before and after releasing the mechanical boundary conditions can be seen in Figure 47.
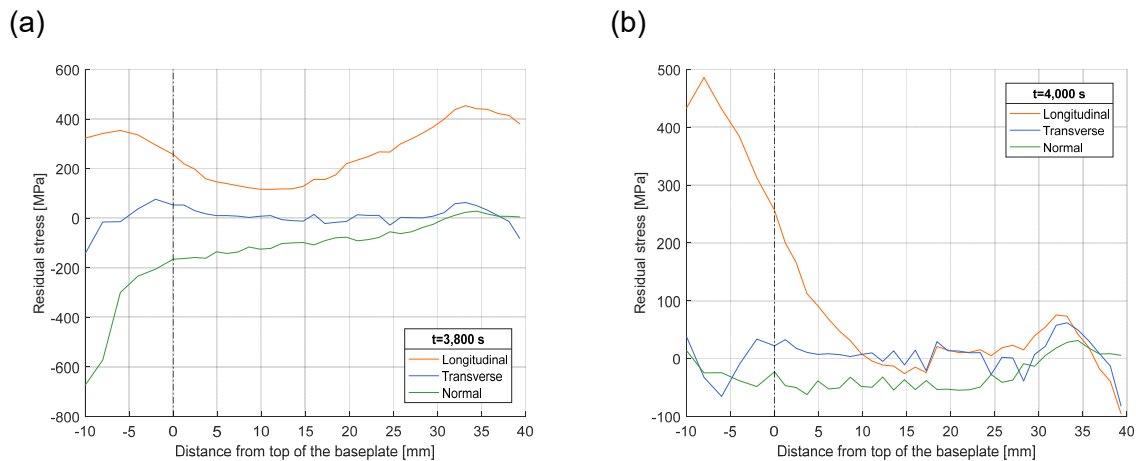
(a)

(b)

Figure 47: Predicted residual stress along the centreline of the wall in longitudinal (x), transverse (y), and normal (z) direction while: (a) clamps are on; (b) clamps are off

When the specimen is clamped, the longitudinal stress predicted across the wall shows first a local peak in the baseplate and then starts to decrease until a wall height of around 15 mm is reached. The stress in the first layers of the deposit is relatively uniform. Towards the final build height, the stress is increasing, reaching its highest value in the deposited wall. The transverse stress is ranging from -140 MPa to 75 MPa and is significantly lower than the longitudinal stresses. Normal stress shows a high accumulation of compressive stress in the baseplate and is steadily increasing over the build height of the wall. Upon releasing the clamps, stress relaxation occurs and inherent plastic strains cause the specimen to bend upwards. Distortion changes the stress field by reducing the tensile stresses in the top of the wall and by increasing tensile stresses in the bottom of the baseplate. The interesting aspect of the longitudinal stresses in Figure 44 (b) occur towards the extremities of the wall. For example, the stress at the top of the wall has a much lower value than at the bottom of the baseplate due to the distortion of the component. This distortion also causes the stress at the bottom of the plate to become highly tensile. There is a reduction of the tensile longitudinal stresses from the baseplate with an increased number of layers. Within a wall height of 10 mm to 30 mm, longitudinal and transverse stresses are almost zero, reaching a peak between 30 mm and 35 mm and are becoming compressive at the top of the wall. Interestingly, there are no significant jumps in the stress profiles at the baseplate-wall interface, as several studies reported [18], [19], [21], [51]. The difference is found to be in the clamping strategy. In this work the baseplate has been clamped only at its four corners allowing the material to distort in the central area during the process which influenced the final stress state. [18], [19], [21], [51] used a more thorough clamping restricting the movement of the baseplate. Investigations showed that uniform residual stresses are produced along the wall during the process being balanced by compressive stresses in the baseplate with a non-continuous transition at the interface. Unclamping causes a redistribution of the stresses. Tensile stresses drop linearly towards the top of the wall. Colegrove et al. [19] proposed an analytical model to estimate residual stress in the longitudinal direction. One assumption of this model is that there is no deflection of the component during deposition. Hönnige and co-workers [52] used the analytical model for estimating distortion and residual stress with reasonably good accuracy. It should be noted that the stress profiles in Figure 47 are determined numerically and need, of course, experimental validation. However, the numerically obtained stress profiles are in good correlation with works conducted by Martina et al. [21] and Hoye et al. [51] showing a similar distribution of stress within an additively manufactured wall structure.

6.5 Aerospace bracket model

Manufacturing of complex structures for industrial applications requires innovative software solutions that enable precise, reliable and reproducible predictions of distortion and residuals stress fields. Simple geometries, such as single wall structures, can be used to validate the numerical models and raise confidence in structural welding simulations to simulate more complex parts. Based on this considerations, computer-aided calculations are used to determine the optimal building strategy for the plasma deposition of a Ti-6Al-4V aerospace bracket. Two building strategies have been identified prior to the process which are analysed virtually. The mechanical performance of both strategies after cooling and unclamping is examined. The total distortion is presented in Figure 48 scaled by a factor of 4.
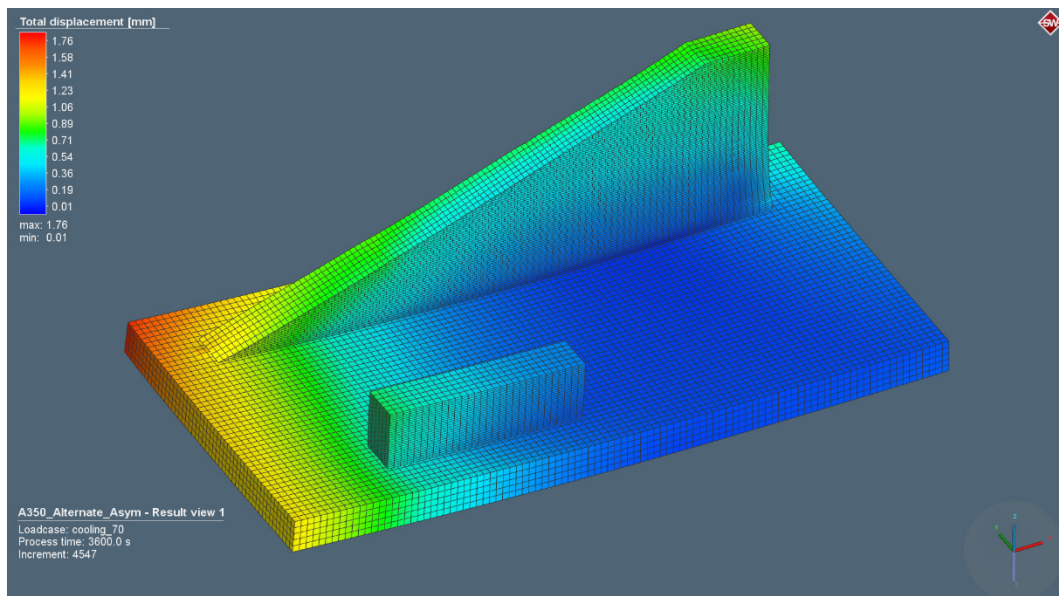
(a)
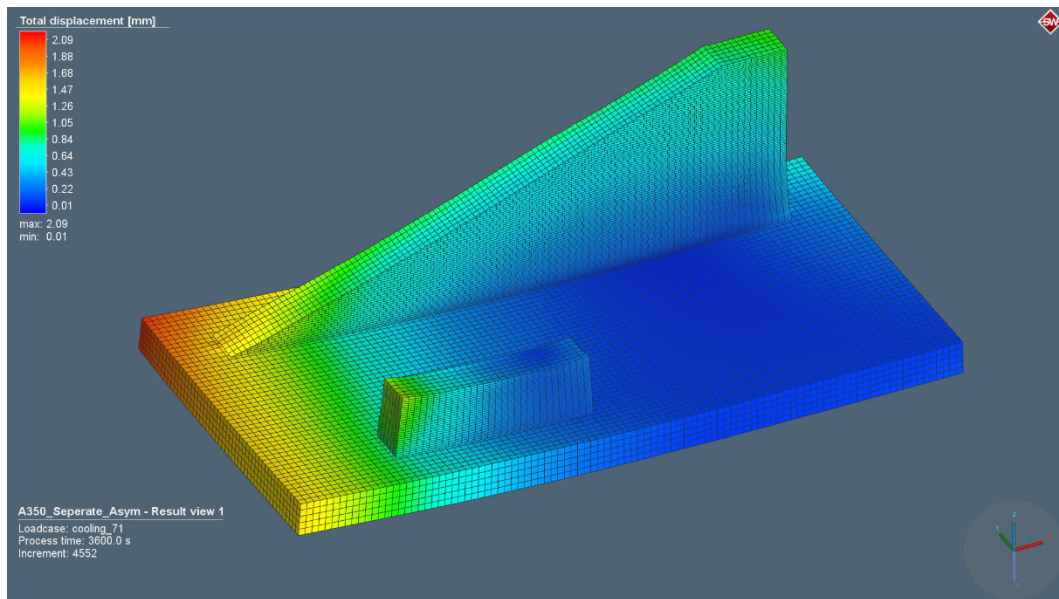
(b)

Figure 48: Total displacement of the aerospace bracket after cooling and unclamping: (a) Strategy 1; (b) Strategy 2

Both building strategies yield similar results regarding the total distortion. Strategy 1, however, shows larger values of distortion in the region where the inclined wall is rising. In this corner

there is no mechanical restraint and the inclined wall is pulling the baseplate upwards. Due to a more homogenous heat distribution of strategy 2, the component is subject to less distortion. Considering the manufacturing of a component on the industrial scale, more attention should be paid to the clamping strategy. To reduce the overall distortion of the bracket, a different clamping strategy would be required. However, due to the dimensions of the baseplate and the design of the plasma torch, the chosen clamping strategy guaranteed accessibility of the torch reaching every start and stop point without crashing.

Numerical simulations are a powerful technique to analyse the thermal and mechanical evolution of components and their properties during the additive manufacturing process. Assessing the results of the numerical simulations, strategy 2 is employed for the additive manufacturing of the Ti-6Al-4V bracket. Less distortion and a more homogenous heat distribution are the driving factors. Figure 49 shows the bracket in the as-built condition and after final machining.
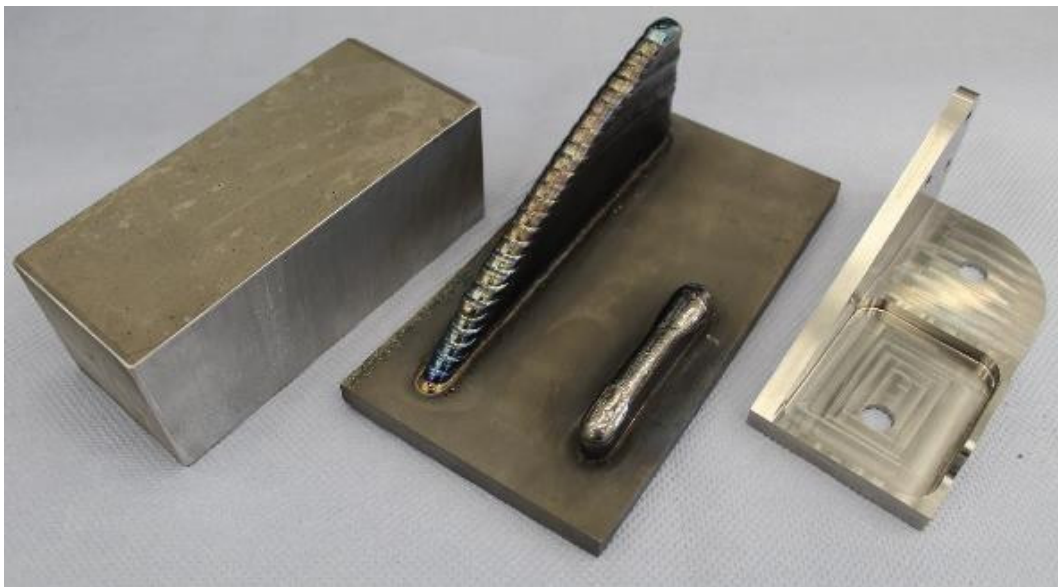
Figure 49: Aerospace bracket manufacturing

The walls show a homogeneous structure without the occurrence of defects. It can be deduced that PMD can be used to produce large-volume homogeneous parts and components. The advantage for a production by means of additive manufacturing is reflected in the material savings, reduced mechanical post-processing and resulting cost savings. In comparison to conventional production methods, the production by means of generative methods allows material savings up to approximately 80 %.

7 Discussion

One of the most important model parameters in structural welding simulations is the representation of the heat source. The shape and the heat flux distribution of a heat source need to be calibrated according to experimentally measured values. Thus, the heat source is not a result of the simulation, but rather a boundary condition that needs to be calibrated. In relation to structural welding simulations, it is fundamental to define an accurate description of the heat source in order to get the best possible results [44], [45], [49]. Table 20 presents the deviations between the measured and calculated parameters that can be derived.

Table 20: Heat source parameters determined by measurement and simulation

Process	Measured values [mm]			Calculated values [mm]			Relative error [%]		
	$2\,b_{\exp}$	$d_{\exp}$	$\phi_{\exp}$	$2\,b_{\text{sim}}$	d_{sim}	ϕ_{sim}	$e_r^{2\,b}$	e_r^d	e_r^ϕ
PH	6.34	1.56	4.06	8.0	3.60	2.22	26.18	42.31	-45.32
SB	8.88	2.68	3.31	8.80	2.4	3.67	-0.90	-10.45	10.88
SB + PH	9.45	3.12	3.03	9.8	4.0	2.45	3.70	28.21	-19.14

From Table 20, it can be determined that deviations between the measured and calculated fusion zone vary to different degrees depending on the process under consideration. The largest deviations are found for the weld pool dimensions during preheating varying from -45.32 % up to 42.31 %. On the contrary, the weld pool shape of the single bead is in good agreement with the measurement. The calculated weld pool of the single bead appears more slender than the experimental one, while the weld pool shape of preheating, and printing plus preheating are overpredicted. The fusion zone of printing with preceding preheating shows good agreement with the calculated width, but shows a discrepancy of up to 28 % considering the depth. Here, the overestimated depth of the preheating pass strongly influences the result. In this study, a trial and error approach has been employed to inversely fit the numerical parameters to the experimental data. The same method has been used by Aarbogh et al. [49]. The authors tuned the input parameters through trial and error, and inverse simulation. From an economical point of view, this method is time consuming, computationally costly and requires a certain level of experience. Gu et al. [44] proposed a technique to extract the parameters of the weld pool shape from the simulation. The main limitation is that the technique elaborated in [44] allows only the calculation of the depth and the width of the molten pool. The authors stated equations to estimate the length of the front and rear ellipsoids as a multiple of the measured width as $a_{\text{f}} = 0.5\,W_{\text{m}}$ and $a_{\text{r}} = 2\,W_{\text{m}}$, respectively. In [49] the authors estimated the front and rear ellipsoid lengths with $a_{\text{f}} = W/2$ and $a_{\text{r}} = W$. In contrast to the width and depth which can directly be determined from micrographs of the weld cross section, the exact determination of the length of the front and rear ellipsoid is experimentally more laborious. To increase the accuracy of the heat source, in-process measurement of the weld pool shape, for example through high speed cameras, could be implemented in the calibration procedure. An accurate calibration of the heat source is crucial for the simulation results. Only then it is possible to reproduce the effective heat input corresponding to real conditions. Improved temperature measurements, a more standardised experimental setup, different operating points of the process and the investigation of various deposition strategies (linear, oscillating, side-by-side beads) could be addressed in future experiments. Ideally, the ultimate goal for a company operating in the field of AM and incorporating simulations into process development is the creation of a heat source database containing input parameters for various operating points, materials, boundary conditions, and machines.

Structural welding simulations allow the prediction of geometrical deviations and accumulated residual stresses as well as their optimisation before conducting experiments. Due to the great length of the multi-layer welds, calculation times for fully transient thermo-mechanical simulations are relatively long, the calculation stability suffers from a high number of bodies in contact elements in the model and the modelling effort is high, as the geometries need to be sliced and positioned layer-wise. Depending on the complexity of the models, the simulation times can vary from a few minutes to several days [46], [53]. The comparison of computational times used for the models is presented in Table 21. The simulations have been performed on an eight core 3.30 GHz i7-5820K processor with 32 GB installed RAM. All models have been calculated by using parallelisation, i.e. the calculation of one simulation is done in parallel using several CPU cores. Simufact supports two parallelisation options, namely domain decomposition method (DDM) and shared memory parallelisation (SMP) [54]. DDM subdivides the model into several sub-models that are connected with each other, whereas SMP allows one solver to use multiple cores.

Table 21: Computational time comparison between different models

Model	Adaptive mesh refinement	Parallelisation	Computational time [h]
Calibration PH	yes	yes	~ 1
Calibration SB	yes	yes	~ 4
Calibration SB + PH	no	yes	~ 2
Single wall	no	yes	~ 24
Aerospace bracket	no	yes	~ 100

When comparing the single wall model and the aerospace bracket model in Table 21, it becomes obvious that with increasing size and complexity of the models the computational times increase gradually. Besides the model size, adaptive mesh refinement increases the computational costs by adding elements to the model. However, there are various ways to reduce computational times including adaptive mesh refinement and un-refinement, the use of symmetry in the models, parallel computing, reduced number of contact bodies and reasonable mesh sizes [45], [46], [53].

In the current release of Simufact Welding, Simufact Welding 2020, users benefit from a new DED module. Compared to the previous version, it comes with many features that enable users to set up DED simulations in faster and more efficient way. Benchmarks between the old and the new version even show a speedup by a factor of 3 [28]. Such developments regarding software tools in the field of additive manufacturing help to fully exploit the potential of DED and make the calculation of complex models on an industrial scale economical.

8 Summary and conclusion

Plasma metal deposition of large-scale Ti-6Al-4V multi-layer structures are investigated experimentally and numerically. A finite element simulation using Simufact Welding 8.0 is set-up to predict the mechanical performance of single bead walls. Experiments are carried out in order to provide data for verifying the calculated temperature profiles, the out-of-plane distortion, and for calibrating the mathematical heat source. Moreover, an airplane bracket is analysed to identify the optimal building strategy and to verify the simulation process for the industrial purpose. According to the results of this study, the following conclusions can be drawn:

1. Based on experimental results, the Goldak double ellipsoid heat source model is verified to suit the experimental determined conditions. As an important feature for the application of structural welding simulations, more accurate temperature measurements for the heat source calibration are necessary. Improved temperature measurements can be addressed by the use of shielded thermocouples, different attachment techniques, higher frequency of data logging and the recording of the weld pool shape.

2. Additionally, the thermal and mechanical boundary conditions are assumed to be constant throughout the deposition process. In fact, these parameters are not only temperature dependent but also a function of the build height and geometry.

3. The results obtained from Simufact Welding 8.0 reproduce the distortion and temperature distribution of the experiment well. Discrepancies between simulation and experiment can occur due to inaccuracies in the calibration of the heat source, thermal and mechanical boundary conditions. Also, the level of detail in the modelling of the bead and wall geometry should be considered as influencing quantity. The weld bead profile for the deposition of the wall is modelled as a rectangle.

4. The virtual process development of the aerospace bracket shows the potential of numerical simulations as digital twin to costly experimental trials.

References

[1] L. Vály, D. Grech, E. Neubauer, M. Kitzmantel, Ľ. Bača, and N. Stelzer, 'Preparation of Titanium Metal Matrix Composites Using Additive Manufacturing', *Key Eng. Mater.*, vol. 742, pp. 129–136, Jul. 2017, doi: 10.4028/www.scientific.net/KEM.742.129.

[2] M. Kitzmantel, L. Vály, D. Grech and G. Mozdzen, 'Challenges for XXL components by powder and wire metal deposition - 4M System', presented at the MAMC, Vienna, Austria, 2016.

[3] *Norsk Titanium*, Dec. 30, 2019. https://www.norsktitanium.com/.

[4] G. Lütjering and J. C. Williams, *Titanium*. Berlin ; New York: Springer, 2003.

[5] G. Welsch, R. Boyer, and E. W. Collings, Eds., *Materials properties handbook: titanium alloys*. Materials Park, OH: ASM International, 1994.

[6] M. Peters, J. Kumpfert, C. H. Ward, and C. Leyens, 'Titanium Alloys for Aerospace Applications', *Adv. Eng. Mater.*, vol. 5, no. 6, pp. 419–427, Jun. 2003, doi: 10.1002/adem.200310095.

[7] C. Leyens and M. Peters, Eds., *Titanium and titanium alloys: fundamentals and applications*. Weinheim : [Chichester: Wiley-VCH ; John Wiley] (distributor), 2003.

[8] N. Knezović and A. Topić, 'Wire and Arc Additive Manufacturing (WAAM) – A New Advance in Manufacturing', in *New Technologies, Development and Application*, 2019, pp. 65–71.

[9] S. W. Williams, F. Martina, A. C. Addison, J. Ding, G. Pardal, and P. Colegrove, *Wire+Arc Additive Manufacturing*. 2015.

[10] I. Karabegović, *New Technologies, Development and Application*. 2019.

[11] J. Z. Li *et al.*, 'Review of Wire Arc Additive Manufacturing for 3D Metal Printing', *Int. J. Autom. Technol.*, vol. 13, no. 3, pp. 346–353, May 2019, doi: 10.20965/ijat.2019.p0346.

[12] 'SBI International', *SBI International*, May 09, 2020. https://www.sbi.at/en/home/ (accessed May 09, 2020).

[13] P. J. Withers and H. K. D. H. Bhadeshia, 'Residual stress. Part 1 – Measurement techniques', *Mater. Sci. Technol.*, vol. 17, no. 4, pp. 355–365, Apr. 2001, doi: 10.1179/026708301101509980.

[14] P. J. Withers, 'Residual stress and its role in failure', *Rep. Prog. Phys.*, vol. 70, no. 12, pp. 2211–2264, Dec. 2007, doi: 10.1088/0034-4885/70/12/R04.

[15] K. Masubuchi, 'Residual Stresses and Distortion in Welds', in *Encyclopedia of Materials: Science and Technology*, Elsevier, 2005, pp. 1–6.

[16] D. Radaj, *Wärmewirkungen des Schweißens Temperaturfeld, Eigenspannungen, Verzug*. Berlin, Heidelberg: Springer Berlin Heidelberg, 1988.

[17] H.-J. Hänsch, J. Krebs, and Hänsch-Krebs, Eds., *Eigenspannungen und Formänderungen in Schweißkonstruktionen: Grundlagen und praktische Anwendungen*. Düsseldorf: DVS-Verl, 2006.

[18] J. Ding *et al.*, 'Thermo-mechanical analysis of Wire and Arc Additive Layer Manufacturing process on large multi-layer parts', *Comput. Mater. Sci.*, Jul. 2011, doi: 10.1016/j.commatsci.2011.06.023.

[19] P. A. Colegrove *et al.*, 'Microstructure and residual stress improvement in wire and arc additively manufactured parts through high-pressure rolling', *J. Mater. Process. Technol.*, vol. 213, no. 10, pp. 1782–1791, Oct. 2013, doi: 10.1016/j.jmatprotec.2013.04.012.

[20] N. Hoye, H. J. Li, D. Cuiuri, and A. M. Paradowska, 'Measurement of Residual Stresses in Titanium Aerospace Components Formed via Additive Manufacturing', *Mater. Sci. Forum*, vol. 777, pp. 124–129, Feb. 2014, doi: 10.4028/www.scientific.net/MSF.777.124.

[21] F. Martina *et al.*, 'Residual stress of as-deposited and rolled wire+arc additive manufacturing Ti–6Al–4V components', *Mater. Sci. Technol.*, vol. 32, no. 14, pp. 1439–1448, Sep. 2016, doi: 10.1080/02670836.2016.1142704.

[22] H. E. Coules, 'Contemporary approaches to reducing weld induced residual stress', *Mater. Sci. Technol.*, vol. 29, no. 1, pp. 4–18, Jan. 2013, doi: 10.1179/1743284712Y.0000000106.

[23] 'Ansys', Apr. 30, 2019. https://www.ansys.com/ (accessed Apr. 30, 2019).

[24] 'Comsol Multiphysics', Apr. 30, 2019. https://www.comsol.eu/ (accessed Apr. 30, 2019).

[25] 'DynaWeld', Apr. 30, 2019. https://www.dynaweld.de/ (accessed Apr. 30, 2019).

[26] 'ESI Sysweld', Apr. 30, 2019. https://www.esi-group.com/de/software-loesungen/virtual-manufacturing/welding-assembly/esi-sysweld (accessed Apr. 30, 2019).

[27] 'VIRFAC by GeonX'. https://altairhyperworks.com/partner/virfac/Modules-and-Specifications (accessed Jan. 20, 2020).

[28] Simufact Engineering Gmbh, 'Simufact Welding', *Simufact Welding*, Jan. 08, 2020. https://www.simufact.com/simufactwelding-welding-simulation.html (accessed Jan. 08, 2020).

[29] M. Megahed, H.-W. Mindt, N. N'Dri, H. Duan, and O. Desmaison, 'Metal additive-manufacturing process and residual stress modeling', *Integrating Mater. Manuf. Innov.*, vol. 5, no. 1, pp. 61–93, Dec. 2016, doi: 10.1186/s40192-016-0047-2.

[30] M. Chiumenti, M. Cervera, A. Salmi, C. Agelet de Saracibar, N. Dialami, and K. Matsui, 'Finite element modeling of multi-pass welding and shaped metal deposition processes', *Comput. Methods Appl. Mech. Eng.*, vol. 199, no. 37–40, pp. 2343–2359, Aug. 2010, doi: 10.1016/j.cma.2010.02.018.

[31] P. Michaleris, 'Modeling metal deposition in heat transfer analyses of additive manufacturing processes', *Finite Elem. Anal. Des.*, vol. 86, pp. 51–60, Sep. 2014, doi: 10.1016/j.finel.2014.04.003.

[32] J. Goldak, A. Chakravarti, and M. Bibby, 'A new finite element model for welding heat sources', *Metall. Trans. B*, vol. 15, no. 2, pp. 299–305, Jun. 1984, doi: 10.1007/BF02667333.

[33] 'Simufact Infosheet Heat Source'. .

[34] A. Lundbäck, 'Modelling of Weld Path for Use in Simulations', Jan. 2020.

[35] V. D. Fachinotti, A. A. Anca, and A. Cardona, 'Analytical solutions of the thermal field induced by moving double-ellipsoidal and double-elliptical heat sources in a semi-infinite body', *Int. J. Numer. Methods Biomed. Eng.*, vol. 27, no. 4, pp. 595–607, Apr. 2011, doi: 10.1002/cnm.1324.

[36] 'Simufact Infosheet Boundary Conditions Thermal'. .

[37] F. Martina, J. Mehnen, S. W. Williams, P. Colegrove, and F. Wang, 'Investigation of the benefits of plasma deposition for the additive layer manufacture of Ti–6Al–4V', *J. Mater. Process. Technol.*, vol. 212, no. 6, pp. 1377–1386, Jun. 2012, doi: 10.1016/j.jmatprotec.2012.02.002.

[38] J. Wang *et al.*, 'Grain morphology evolution and texture characterization of wire and arc additive manufactured Ti-6Al-4V', *J. Alloys Compd.*, vol. 768, pp. 97–113, Nov. 2018, doi: 10.1016/j.jallcom.2018.07.235.

[39] DIN EN 1001-1, 'Schweißen – Empfehlungen zum Schweißen metallischer Werkstoffe – Teil 1: Allgemeine Anleitungen für das Lichtbogenschweißen; Deutsche Fassung EN 1011-1:2009'. März 2009.

[40] L. Thijs, F. Verhaeghe, T. Craeghs, J. V. Humbeeck, and J.-P. Kruth, 'A study of the microstructural evolution during selective laser melting of Ti–6Al–4V', *Acta Mater.*, vol. 58, no. 9, pp. 3303–3312, May 2010, doi: 10.1016/j.actamat.2010.02.004.

[41] Y. M. Ren, X. Lin, X. Fu, H. Tan, J. Chen, and W. D. Huang, 'Microstructure and deformation behavior of Ti-6Al-4V alloy by high-power laser solid forming', *Acta Mater.*, vol. 132, pp. 82–95, Jun. 2017, doi: 10.1016/j.actamat.2017.04.026.

[42] P. Almeida and S. Williams, *Innovative process model of Ti–6Al–4V additive layer manufacturing using cold metal transfer (CMT)*. 2010.

[43] S. Ríos, P. A. Colegrove, F. Martina, and S. W. Williams, 'Analytical process model for wire + arc additive manufacturing', *Addit. Manuf.*, vol. 21, pp. 651–657, May 2018, doi: 10.1016/j.addma.2018.04.003.

[44] Y. Gu, Y. D. Li, Y. Yong, F. L. Xu, and L. F. Su, 'Determination of parameters of double-ellipsoidal heat source model based on optimization method', *Weld. World*, vol. 63, no. 2, pp. 365–376, Mar. 2019, doi: 10.1007/s40194-018-00678-w.

[45] P. Helbig, 'Kalibrierung von Ersatzwärmequellen für die numerische Simulation von Laserschweißprozessen', Universität Kassel, 2018.

[46] R. Martukanitz *et al.*, 'Toward an integrated computational system for describing the additive manufacturing process for metallic materials', *Addit. Manuf.*, vol. 1–4, pp. 52–63, Oct. 2014, doi: 10.1016/j.addma.2014.09.002.

[47] B. Wu, Z. Pan, D. Ding, D. Cuiuri, and H. Li, 'Effects of heat accumulation on microstructure and mechanical properties of Ti6Al4V alloy deposited by wire arc additive manufacturing', *Addit. Manuf.*, vol. 23, pp. 151–160, Oct. 2018, doi: 10.1016/j.addma.2018.08.004.

[48] G. F. Deyev, *Surface Phenomena in Fusion Welding Processes*. CRC Press, 2005.

[49] H. M. Aarbogh, M. Hamide, H. G. Fjær, A. Mo, and M. Bellet, 'Experimental validation of finite element codes for welding deformations', *J. Mater. Process. Technol.*, vol. 210, no. 13, pp. 1681–1689, Oct. 2010, doi: 10.1016/j.jmatprotec.2010.05.014.

[50] S. Liu and Y. C. Shin, 'Additive manufacturing of Ti6Al4V alloy: A review', *Mater. Des.*, vol. 164, p. 107552, Feb. 2019, doi: 10.1016/j.matdes.2018.107552.

[51] N. Hoye, H. J. Li, D. Cuiuri, and A. M. Paradowska, 'Measurement of Residual Stresses in Titanium Aerospace Components Formed via Additive Manufacturing', *Mater. Sci. Forum*, vol. 777, pp. 124–129, Feb. 2014, doi: 10.4028/www.scientific.net/MSF.777.124.

[52] 'Analytical Model for Distortion Prediction in Wire + Arc Additive Manufacturing', Oct. 2018, pp. 277–282, doi: 10.21741/9781945291890-44.

[53] J. Ding *et al.*, 'Thermo-mechanical analysis of Wire and Arc Additive Layer Manufacturing process on large multi-layer parts', *Comput. Mater. Sci.*, Jul. 2011, doi: 10.1016/j.commatsci.2011.06.023.

[54] 'Simufact Infosheet Prallelsization'. .

[55] F. J. Gil, M. P. Ginebra, J. M. Manero, and J. A. Planell, 'Formation of α-Widmanstätten structure: effects of grain size and cooling rate on the Widmanstätten morphologies and on the mechanical properties in Ti6Al4V alloy', *J. Alloys Compd.*, vol. 329, no. 1–2, pp. 142–152, Nov. 2001, doi: 10.1016/S0925-8388(01)01571-7.

[56] W. Sha and S. Malinov, *Titanium alloys: modelling of microstructure, properties and applications*. Boca Raton, Fla.: CRC Press, 2009.

[57] M. J. Donachie, *Titanium: a technical guide*. Metals Park, OH: ASM International, 1988.

[58] T. Ahmed and H. J. Rack, 'Phase transformations during cooling in α+β titanium alloys', *Mater. Sci. Eng. A*, vol. 243, no. 1, pp. 206–211, 1998, doi: https://doi.org/10.1016/S0921-5093(97)00802-2.

[59] E. R. Denlinger, 'THERMO-MECHANICAL MODEL DEVELOPMENT AND EXPERIMENTAL VALIDATION FOR METALLIC PARTS IN ADDITIVE MANUFACTURING', The Pennsylvania State University, 2015.

[60] B. Wu *et al.*, 'Mitigation of thermal distortion in wire arc additively manufactured Ti6Al4V part using active interpass cooling', *Sci. Technol. Weld. Join.*, vol. 24, no. 5, pp. 484–494, Jul. 2019, doi: 10.1080/13621718.2019.1580439.

[61] M. Graf, A. Hälsig, K. Höfer, B. Awiszus, and P. Mayr, 'Thermo-Mechanical Modelling of Wire-Arc Additive Manufacturing (WAAM) of Semi-Finished Products', *Metals*, vol. 8, no. 12, p. 1009, Dec. 2018, doi: 10.3390/met8121009.

[62] J. C. Heigel, P. Michaleris, and E. W. Reutzel, 'Thermo-mechanical model development and validation of directed energy deposition additive manufacturing of Ti–6Al–4V', *Addit. Manuf.*, vol. 5, pp. 9–19, Jan. 2015, doi: 10.1016/j.addma.2014.10.003.

[63] A. Schweizer, *Formelsammlung und Berechnungsprogramme Anlagenbau*, Jan. 05, 2020. https://www.schweizer-fn.de/stoff/reibwerte/reibwerte.php (accessed Jan. 05, 2020).

[64] 'Coefficient of friction', Jan. 05, 2020. http://www-eng.lbl.gov/~ajdemell/coefficients_of_friction.html (accessed Jan. 05, 2020).

Appendix A – Titanium and its alloys

Titanium is an allotropic element, i.e. it exists in more than one crystallographic configuration. Pure titanium crystallises at ambient temperature and pressure in a hexagonal close packed structure (hcp, α phase), undergoing an allotropic phase transformation as its temperature is raised through 882 °C to a body-centred cubic (bcc) β phase. Each crystallographic modification is only stable within particular temperature ranges and the corresponding allotropic transformation temperature is strongly influenced by interstitial or substitutional elements and therefore depends on the purity of the metal [4, p. 14]. The melting point of pure titanium is 1668 °C. The atomic unit cells of hexagonal close packed α titanium and the body-centred cubic β titanium are schematically shown in Figure 50. Additionally, the most densely packed planes and directions are indicated.
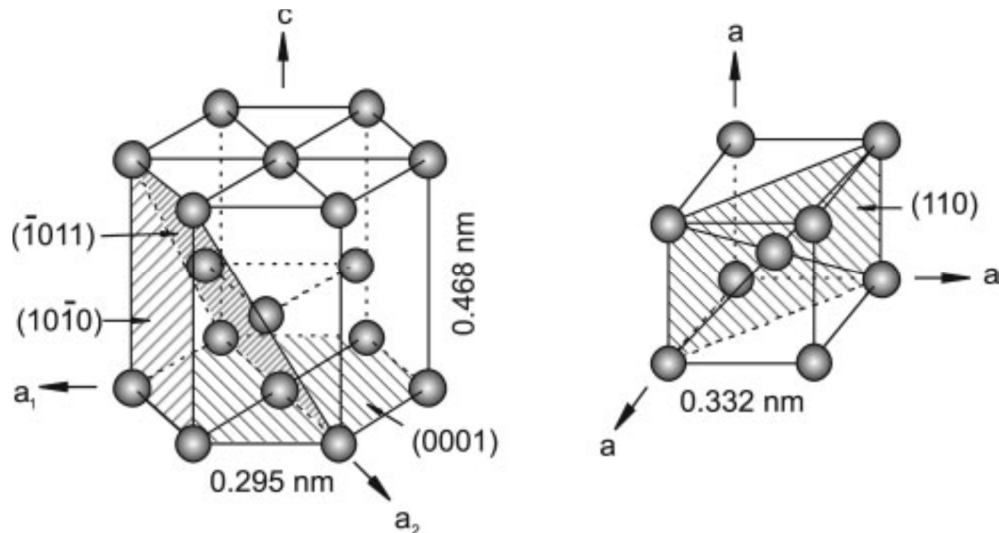

Figure 50: Unit cells of α and β phase [4]

The existence of two different crystal structures has a considerable influence on many properties of titanium alloys. Lütjering and Williams [4, pp. 14–17] showed that the intrinsically anisotropic behaviour of the hcp crystal structure of the α phase causes a distinctive directionality of the mechanical behaviour for titanium and its alloys. The modulus of elasticity can vary between 145 GPa for a load applied parallel to the c-axis and 100 GPa for a load applied perpendicular to the c-axis. Also, the shear modulus varies between 32 GPa to 46 GPa for shear stresses applied in the (0002) and $\{10\bar{1}0\}$ planes or $<11\bar{2}0>$ direction, respectively. Regarding to polycrystalline materials, the elastic properties depend on the nature and intensity of the crystallographic texture.

The elastic properties of the β phase at room temperature can only be measured if the metastable β phase is enriched with β stabilising elements, since it is not stable in pure titanium. For sufficiently high concentrations of β stabilising elements and fast cooling, the metastable β phase can be retained at room temperature. The elastic properties of the β phase depend on the amount of stabiliser elements, but have in general lower modulus of elasticity than α and α+β alloys. [4]

A.1 Alloying elements

Alloying elements in titanium can be classified according to their effect on the stabilities of the α and β phase depending on whether they increase or decrease the α/β transition temperature of pure titanium. Depending on their influence on the β transus temperature, the alloying elements are classified as neutral, α stabilisers, or β stabilisers [4]:

- α stabilising elements extend the α phase field to higher temperatures with increasing solute content and can be divided into substitutional and interstitial elements. Aluminum is the most widely used substitutional element, oxygen, nitrogen, and carbon are the most common interstitial elements. Among the α stabilising elements, aluminum is by far the most important alloying element due to its large solubility in both the α and β phase. α stabilisers develop a two-phase α+β field and raise the β/(α+β) transformation temperature.

- Alloying additions that decrease the (α+β)/α transus to lower temperatures are referred to as β stabilisers. β stabilising elements are subdivided into β isomorphous and β eutectoid elements. The β isomorphous group consists of elements that are miscible in the β phase, the eutectoid group forms eutectoid systems with titanium. V, Mo and Nb are the most frequently used β isomorphous elements in titanium alloys. Sufficient concentrations of these elements can stabilise the metastable β phase to room temperature. Among the β eutectoid elements, Cr, Fe and Si are used in many titanium-based alloys and others are just used for special purposes.

- Zr, Hf and Sn are considered neutral elements since they have nearly no influence on the α/β phase boundary. They lower the β transus temperature slightly and increase the transformation temperature again at higher concentrations. [4], [7]

The influence of various alloying elements on the phase diagrams of different titanium alloys can be seen in Figure 51. Also outlined is the likely formation of intermetallic compounds $\gamma(A_xB_y)$ with increasing content of alloying elements for Ti-Al-type and Ti-Fe-type alloys.
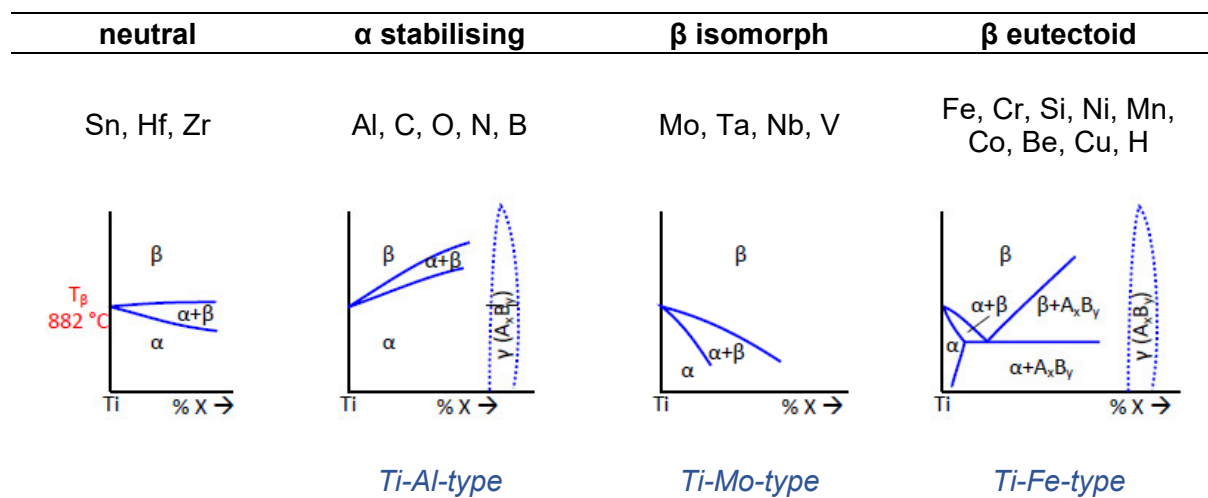
neutral	α stabilising	β isomorph	β eutectoid
Sn, Hf, Zr	Al, C, O, N, B	Mo, Ta, Nb, V	Fe, Cr, Si, Ni, Mn, Co, Be, Cu, H

Figure 51: Effect of alloying elements on phase diagrams of titanium alloys [4]

Commercial titanium alloys are usually classified into three different categories, referring to the common phases present: α, α+β, and β alloys. This classification can be further subdivided into near α and near β or metastable β alloys [7]. The classification of titanium alloys is schematically outlined in the pseudo-binary section through the β isomorphous phase diagram (Figure 52).
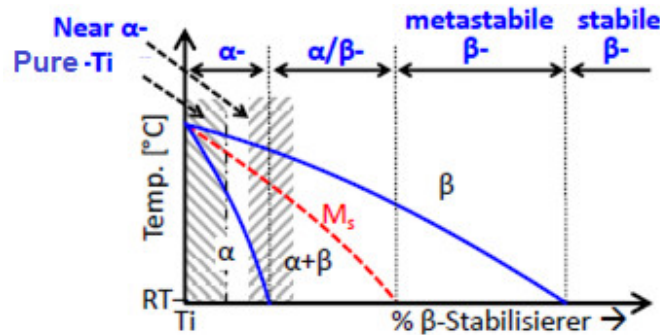
Figure 52: Classification of titanium alloys [4]

According to this scheme, the group of α alloys consists of commercially pure (cp) titanium and alloys alloyed with α stabilising elements and/or neutral elements. Near α alloys contain minor fractions of β stabilising elements and are placed near the α/(α+β) phase boundary. The group of α+β alloys has a range from the α/(α+β) phase boundary up to the intersection of the M_s line with room temperature and is dominated by the Ti-6Al-4V alloy. The martensitic phase transformation of α+β alloys can be achieved upon fast cooling from the β phase field to room temperature. The group of β alloys consists of metastable and single phase field β alloys. The proportion of β stabilising elements is raised to a level, where β alloys no longer transform martensitically upon fast cooling from the β phase field, marking a characteristic feature of the β alloys. Metastable β or near β alloys are located in the equilibrium α+β phase region of the pseudo-binary phase diagram, thus they are located still in the two-phase field. Single phase field β alloys mark the end of the alloying scale, but do not exist as commercial materials. [4], [7]

A.2 Ti-6Al-4V phase diagrams

Ti-6Al-4V is the most widely used titanium alloy due to its good balance of strength, ductility, fatigue, and fracture properties [4]. Its ternary phase diagram, which is composed of two binary phase diagrams with Al as α stabilising element and V as a β stabilising element is shown in Figure 53.
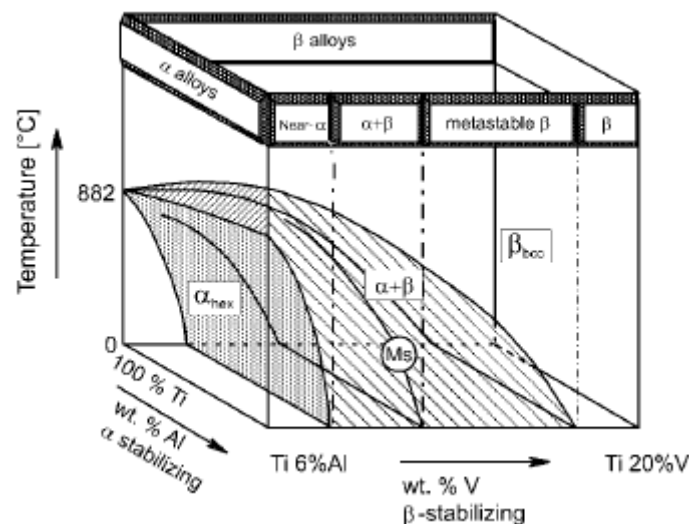

Figure 53: Ternary phase diagram of Ti-6Al-4V [7]

As pointed out in the previous chapter, aluminum is the most widely used substitutional element in titanium. Figure 54 shows the equilibrium phase diagram of the Ti-Al system. For

higher concentrations of aluminum the formation of intermetallic compounds, such as Ti_3Al (α_2), TiAl (γ), $TiAl_2$ and $TiAl_3$ is likely to occur. The presence of Ti_3Al and TiAl intermetallic phases is noteworthy, since both phases are of great importance for titanium-aluminide alloys, especially for high temperature applications [4]. Ti_3Al starts to form in the two phase region ($\alpha + Ti_3Al$) at about 5 wt.% Al for temperatures above 500 °C and is extremely brittle. To avoid the precipitation of Ti_3Al in the α phase, the aluminium concentration in most alloys is limited to 6 wt.% [4]. In Ti-6Al-4V, the formation of Ti_3Al has been experimentally verified for oxygen concentrations less than 0.2 wt.% O_2, and at aging temperatures from 500 to 600 °C with increased oxygen concentrations [5].
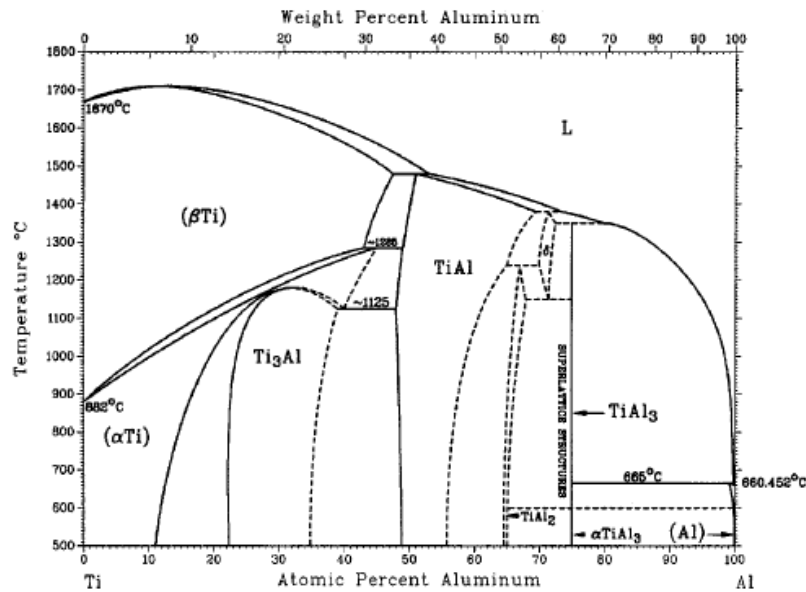

Figure 54: Ti-Al binary phase diagram [7]

A.3 β/α phase transformations

Ti-6Al-4V β transus temperature is around 1000 °C and varies slightly according to small variations in the quantities of interstitial oxygen content. The final microstructure is affected by the cooling rate from the β region to room temperature.

Table 22: T_β of Ti-6Al-4V depending in O_2 content [4]

Common Name	Alloy composition [wt.%]	T_β [°C]
Ti-6-4	Ti-6Al-4V (0.20 O_2)	995
Ti-6-4 ELI	Ti-6Al-4V (0.13 O_2)	975

The transformation from bcc β phase to hcp α phase can either occur by a diffusion controlled nucleation and growth or martensitically by a diffusionless process [55]. In the first case, the β to α transformation begins below the β transus temperature when the alloy is slowly cooled from the β region. The α phase first nucleates preferentially at β grain boundaries (α_{GB}) within the metastable β phase followed by the growth of this nucleus into the surrounding β matrix. During continued cooling α plates grow into the β grain by a transfer of atoms as well-defined plates with their long dimension parallel to $\{110\}_\beta$ plane [55]. Observations by transmission electron microscopy and energy dispersive spectroscopy indicated that the β to α transformation is controlled mainly by vanadium diffusion [56, p. 207]. α plates belonging to

the same variant of Burger`s relationship are called colony α. Individual α plates are separated within the colonies by retained β matrix (β plates), which results in a lamellar microstructure.
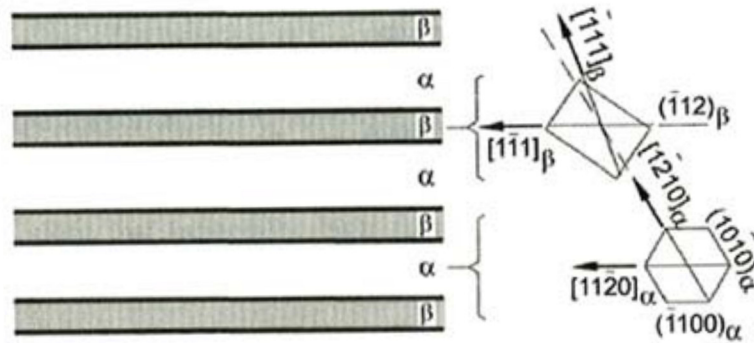

Figure 55: Representation of the crystallographic relationship between α plates and retained β in α colonies [4]

Widmanstätten structure or basket weave is a particular type of lamellar structure which develops with an increasing cooling rate or when newly nucleated lamellae collide with each other and cannot grow further resulting in a nucleation not only on β grain boundaries, but also on boundaries of already developed α lamellae/colonies. The new α plates grow perpendicular to the existing α colony growth direction to minimise the overall elastic strain. [4]

In the second case, β can decompose by a martensitic reaction upon fast cooling from the β phase field. Lütjering and Williams [4] describe the martensitic transformation as a cooperative movement of atoms by a shear type process resulting in a microscopically homogeneous transformation of the bcc into the hexagonal crystal lattice over a given volume. During this shear transformation process, the most densely packed $\{110\}_\beta$ planes merge into the $\{0001\}_\alpha$ basal plane of the hexagonal lattice.
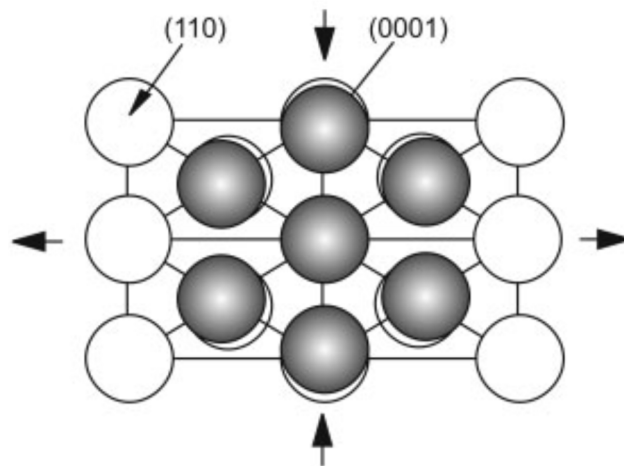

Figure 56: Schematic illustration of the martensitic transformation between bcc β and hcp α [7]

Two types of martensite can be distinguished: hexagonal close packed martensite (α') and orthorhombic martensite (α''). α' is crystallographically related to the α-phase and can be observed in two morphologies, namely massive martensite or acicular martensite. Massive martensite occurs only in pure titanium, very ductile alloys, and alloys with high martensitic transformation temperatures. Acicular martensite occurs in alloys with a higher solute content

(lower martensitic start temperature M_s) and consists of a mixture of individual α plates with different variants of the Burgers relationship. α' is supersaturated in β stabilisers and decomposes into to α+β by precipitating incoherent β particles at dislocations or β phase layers at plate boundaries upon annealing in the α+β phase field. [4]

Orthorhombic α'' martensite is a rather soft martensite and can be obtained by quenching the β phase enriched with 10 ± 2 wt.% vanadium above 800 °C (slightly above the martensitic start temperature), or as a stress-induced product by straining metastable beta [5].

It should be noted that upon quenching from above β transus to room temperature, not all of β is converted to α' or α''. The addition of alloying elements, e.g. aluminium and vanadium in Ti-6Al-4V, place the martensite finish temperature M_f below room temperature. [57]

A.4 Microstructure of Ti-6Al-4V

As an alpha beta alloy, Ti-6Al-4V forms a variety of microstructures with different geometrical arrangements of alpha and beta phases. A combination of the properties of both phases can benefit to achieve specific characteristics of the material. Properties of Ti-6Al-4V are substantially influenced by the microstructure. Depending on the particular thermo-mechanical treatment and interstitial oxygen content, different volume fractions of α and β phases can be obtained [5]. In general, the morphologies and microstructures can be classified into three different categories: lamellar structure, equiaxed structure or bimodal type microstructure, which is a mixture of both [4], [5]. Alternatively, the microstructure can be differentiated based on the transformation behaviour of bcc β phase to hcp α phase. Beta can transform into alpha in two ways, either by a diffusion controlled nucleation and growth process, or by a diffusionless transformation. Thus, understanding the mechanisms of microstructure formation is useful to link the observed microstructure of additive manufactured parts to its thermal history, and to predict some of the mechanical properties.

A.4.1 Fully lamellar structure

Lamellar structures can be obtained by cooling from the β phase field. Depending on the cooling rate, the lamellae are either coarse or fine. A fairly coarse lamellar structure forms due to slow cooling into the two-phase region from above the β transus $T_β$ leading to nucleation and grain growth of the α phase in plate form (as lamellae) into the prior β grain, starting from β grain boundaries. It is referred to as plate-like α (Figure 57 (b)). In optical micrographs, normally the α phase appears white, surrounded by a black β phase matrix. Faster cooling (air cooling) results in fine needle-like α or acicular α (Figure 57 (c)). Basket weave or Widmanstätten structures can develop under certain intermediate cooling rates, which become finer with increasing cooling rate. The β phase remains as thin layer between the Widmanstätten α plates. Rapid quenching from above the β transus leads to a martensitic transformation of β, resulting in needle-like hcp α' martensite (Figure 57 (d)). Thus, much finer lamellar structures can be obtained by water quenching from the β phase field. [4], [5], [7]
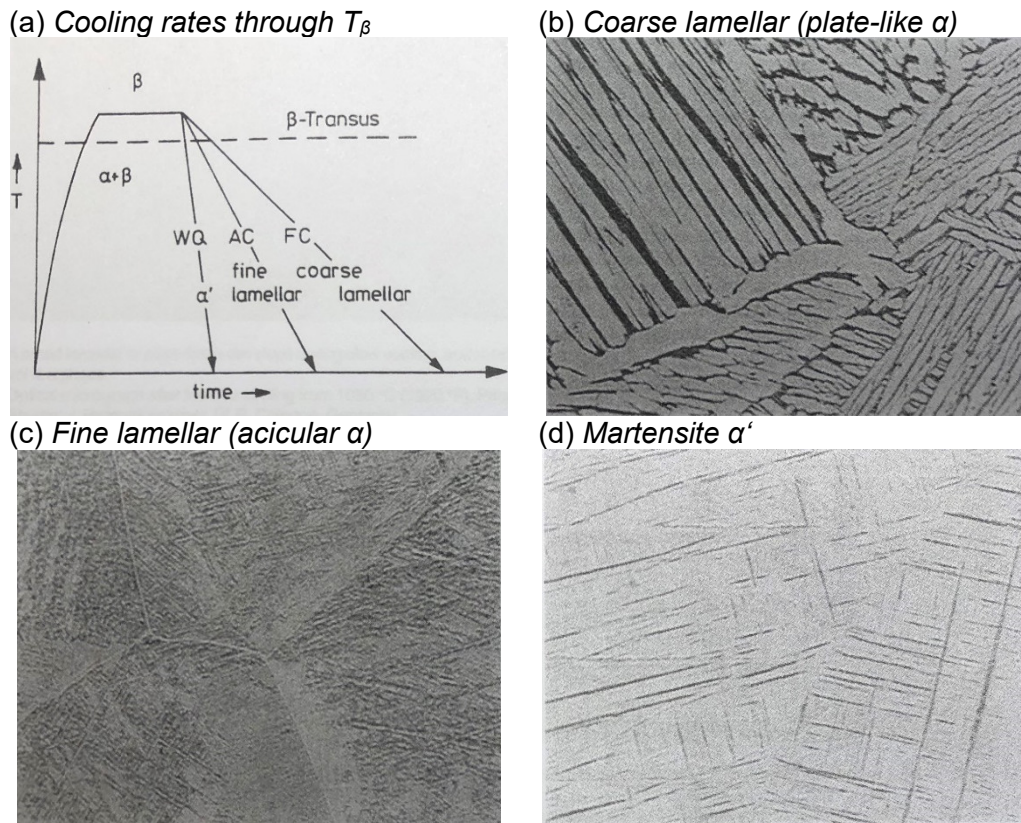
(a) *Cooling rates through T_β*

(b) *Coarse lamellar (plate-like α)*

(c) *Fine lamellar (acicular α)*

(d) *Martensite α'*

Figure 57: Effect of the cooling rate from the β phase field on lamellar structures [5]

As can be seen in Figure 57 (a), the cooling rate through the β transus determines the characteristic features of the lamellar microstructure, such as the size of the α lamellae, the α colony size, and the thickness of α layers at β grain boundaries. All this features decrease with increasing cooling rate[4, p. 178]. Furthermore, the cooling rate and alloy composition determine the transformation mechanism of the bcc β phase to the hexagonal α phase. Slow cooling rates permit diffusion-controlled partitioning between α and β, whereas high cooling rates supress the diffusion-controlled nucleation and growth process and the transformation occurs martensitically. For a fully martensitic microstructure, i.e. the transformation is completely diffusionless, cooling must happen at extremely high rates at above 410 °C/s and from temperatures above the martensitic start temperature (M_S). [58]. The martensitic start temperature is not constant and varies depending on the starting structure and homogeneity of the microstructure [7].

A.4.2 Fully equiaxed structure

The equiaxed microstructure is the result of a recrystallisation process. The route to produce fully equiaxed microstructures is hot working of the material in the α-β phase field, where the lamellar alpha breaks up into equiaxed alpha. Subsequent annealing at subtransus temperatures generates a recrystallised and equiaxed microstructure [5]. Sufficiently slow cooling rates are necessary to allow the growth of primary equiaxed α ($α_p$) only, rather than the formation of α lamellae within the β grains. The β phase is located at the triple points of the α phase grains. Another way to produce much finer equiaxed microstructures consists in annealing at lower temperatures, at which the equilibrium volume fraction of $α_p$ is large enough to stimulate the grow of α grains directly from the deformed lamellae. [4]
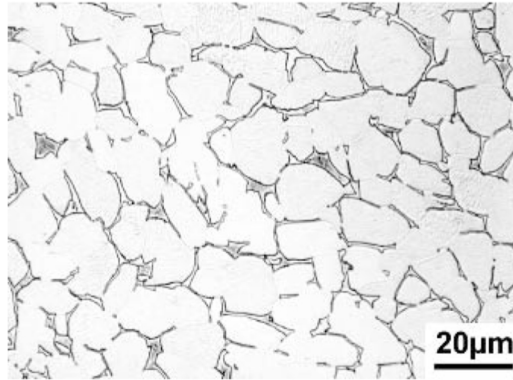
Figure 58: Fully equiaxed microstructure [4]

A.4.3 Bimodal type microstructure

The processing conditions to obtain bimodal (duplex) structures are similar with those of the equiaxed structure, except for the higher cooling rates after the recrystallisation anneal. The bimodal structure is achieved by annealing just below the β transus temperature in the α+β phase field followed by subsequent water quenching or air cool. The microstructure consists of isolated primary equiaxed α_p grains in a transformed β matrix (lamellar structure). Thus, the bimodal microstructure can be considered as a combination of lamellar and equiaxed microstructure. The duplex annealing (DA) temperature determines the volume fractions of α_p and transformed β, the cooling rate mainly influences the width of the α lamellae. [4], [5]
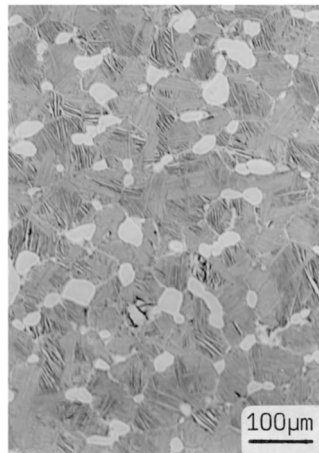

Figure 59: Bimodal microstructure [4]

Appendix B – Thermo-mechanical properties of Ti-6Al-4V

Temperature dependent thermal and mechanical properties of Ti-6Al-4V found in literature are listed in Table 23 and Table 24. This data can be used as an informative basis.

Table 23: Temperature dependent properties of Ti-6Al-4V [59]

T [°C]	λ [W/m/°C]	c_p [J/kg/K]	E [GPa]	σ_Y [MPa]	α [10^{-6}/°C]
20	6.6	565	104	768	8.60
93	7.3	565	101	735	8.66
205	9.1	574	94.0	685	8.75
315	10.6	603	88.3	636	9.08
425	12.6	649	82.6	586	9.40
540	14.6	699	77.5	542	9.55
650	17.5	770	72.6	501	9.70
760	17.5	858	67.7	459	9.70
870	17.5	959	62.8	417	9.70

In [59] the Poisson's ratio and the density are assumed to be constant over the whole temperature domain with 0.34 and 4.43 g/cm³ respectively. Conductivity, specific heat, Young's Modulus, yield strength and coefficient of thermal expansion are assumed to be constant above 870 °C.

Table 24: Temperature dependent properties of Ti-6Al-4V [60]

T [°C]	λ [W/m/°C]	c_p [J/kg/K]	E [GPa]	σ_Y [MPa]	α [10^{-6}/°C]
20	6.8	611	114	804	9.1
100	7.9	678	110	620	9.1
200	8.79	691	104	638	9.2
300	10.47	703	98	552	9.3
400	12.56	741	92	455	9.5
500	14.24	754	84	377	9.7
750	27	760	75	350	9.7
1000	30	950	74	130	10
1500	35	1092	57	40	11.5
1700	14	1347	10	40	15.8

In [60] the Poisson's ratio is also assumed to be a constant with value of 0.30.

Appendix C – Numerical parameter study

To avoid arbitrary trial and error simulations by testing combinations of different cooling parameters, a parameter study is conducted examining the impact of single parameters on the temperature profiles and fusion zone dimensions. Thereby, specific parameters are varied while others are kept constant. To get an estimation of the expected temperature fields, several simulations are executed, in which different points corresponding to thermocouple locations of the calibration experiments on the upper surface of the baseplate (in the Simufact GUI these points are called particles) are implemented. These points are then displayed in a time-temperature diagram. To assess the molten pool dimensions Simufact has a built-in welding monitor which allows to analyse the cross section along trajectories. The following paragraphs provide an overview of the influence of individual parameters. The single bead model is utilised to perform the numerical trials. Heat source and welding parameters are shown in Table 25 and Table 26.

Table 25: Heat source parameters employed for the parameter study

a_f [mm]	a_r [mm]	b [mm]	d [mm]	M [-]	f_f [-]
6.72	13.44	6.72	4.41	0	0.66

Table 26: Welding parameters employed for the parameter study

I [A]	U [V]	v_TS [mm/min]
130	25	200

C.1 Coefficient of thermal efficiency

The heat input during welding can be regarded as a main factor influencing the properties of welds. It influences the time-temperature cycles occurring during welding. The thermal efficiency thus describes the ability of a welding process to convert the energy provided (e.g. electrical) to the heat source into heat at the welding point. It includes essential losses through e.g. radiation and heat dissipation. In a first step, values for the thermal efficiency are varied. Table 27 gives an overview of the thermal input parameters. Hereby, the model is assumed to be completely adiabatic.

Table 27: Parameter variation of the thermal efficiency

Parameters		V1	V2	V3	V4
Thermal efficiency	η	0.2	0.4	0.6	0.8
Coefficient of radiation	ε	0	0	0	0
Convective heat transfer coefficient	h	0	0	0	0
Contact heat transfer coefficient	a	0	0	0	0

The heat input by the moving heat source along a trajectory causes the formation of time-dependent temperature fields in the workpiece. In Figure 60 the time-temperature profiles

for different values of the thermal efficiency at a specific location on the baseplate can be seen.
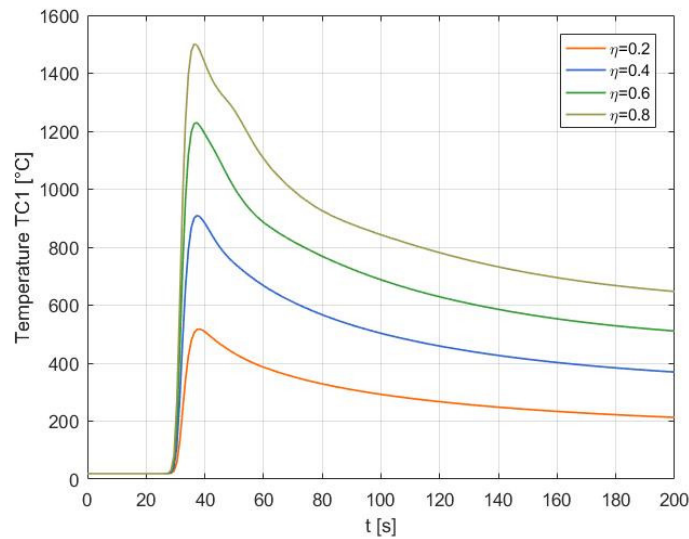

Figure 60: Time-temperature profiles for different values of the thermal efficiency

The thermal efficiency significantly influences peak temperatures and the formation of the melting zone. An efficiency of 0.8 onwards even causes burn-through in the baseplate (Figure 61 (b)).
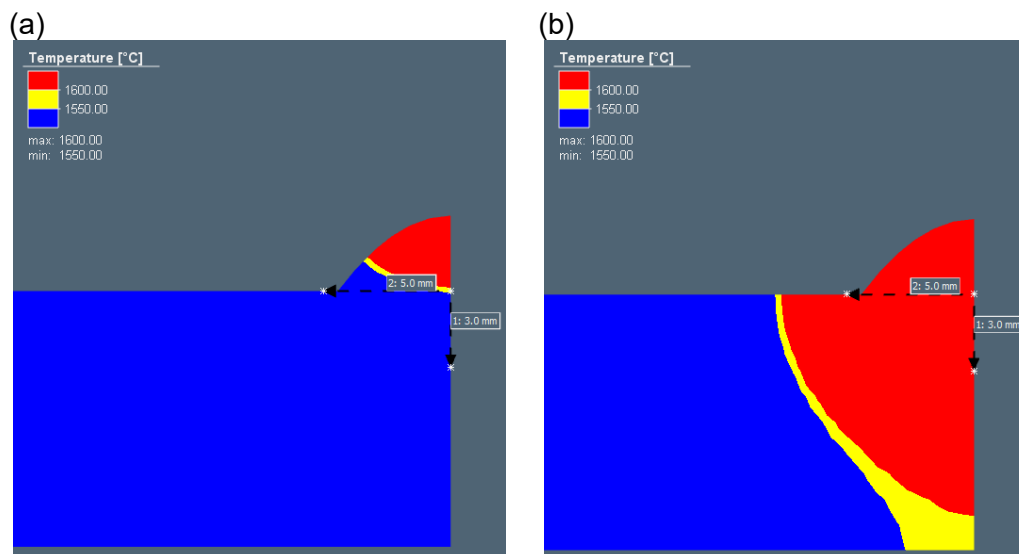

Figure 61: Molten pool dimensions for different values of epsilon: a) $\eta = 0.2$; b) $\eta = 0.8$

Considering the measured temperature profiles of the single pass weld and the dimensions of the fusion zone obtained from the metallurgical analysis, a value of 0.4 for the thermal efficiency yields the most accurate results with the measurements. In the following simulations, successively losses due to radiation, convection and contact heat transfer are incorporated in order to integrate the cooling behaviour into the model.

C.2 Coefficient of radiation

The effect on the cooling behaviour due to radiation losses is studied. Thermal parameters for the simulations can be seen in Table 28.

Table 28: Parameter variation of the coefficient of radiation

Parameters		V1	V2	V3	V4
Thermal efficiency	η	0.4	0.4	0.4	0.4
Coefficient of radiation	ε	0.2	0.4	0.6	0.8
Convective heat transfer coefficient	h	0	0	0	0
Contact heat transfer coefficient	a	0	0	0	0

The thermal efficiency is kept constant at 0.4, losses due to convection and contact are set to zero and the coefficient of radiation is varied in steps of 0.2. Time-temperature profiles for different values of the coefficient of radiation are shown in Figure 62.
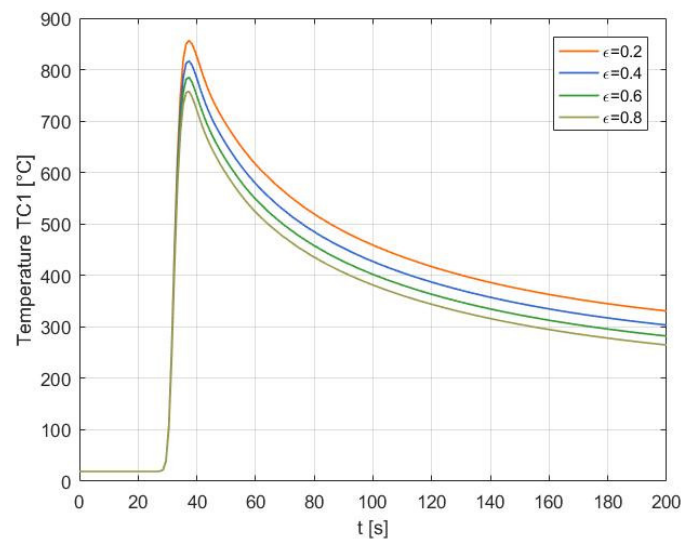

Figure 62: Time-temperature profiles for different values of the coefficient of radiation

The coefficient of emissivity influences the peak temperature considerably. The steepest slopes in the temperature profiles are observed in the high temperature domains. It can be deduced that the radiation losses are more dominant in the high temperature regions close to the weld zones. Additionally, the coefficient of radiation affects the dimensions of the fusion zone - the higher the coefficient of radiation, the smaller the molten pool dimensions, as can be seen in Figure 63.
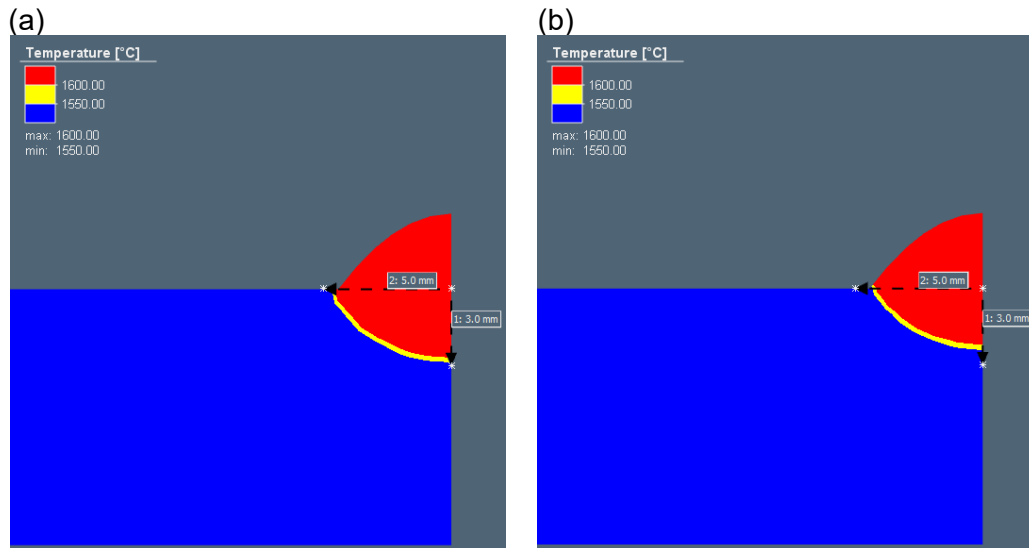
Figure 63: Molten pool dimensions for different values of epsilon: a) $\varepsilon = 0.2$; b) $\varepsilon = 0.8$

C.3 Convective heat transfer coefficient

The same procedure is applied for the convective heat transfer coefficient. Thermal parameters for the simulations can be seen in Table 29.

Table 29: Parameter variation of the convective heat transfer coefficient

Parameters		V1	V2	V3	V4
Thermal efficiency	η	0.4	0.4	0.4	0.4
Coefficient of radiation	ε	0	0	0	0
Convective heat transfer coefficient	h	5.0	10.0	20.0	30.0
Contact heat transfer coefficient	a	0	0	0	0

The convective heat transfer coefficient can range from 5 W/(m²·K) [49] up to 35 W/(m²·K) [61]. If active cooling is applied, the coefficient might get quite large and achieve values up to 100 W/(m²·K) [62]. In this study no active cooling is applied. The shielding gas flow is considered not agitating the argon atmosphere in the welding chamber. Consequently, the convection becomes equal to free convection and uniform on all surfaces. The calculated time-temperature profiles can be seen in Figure 64.
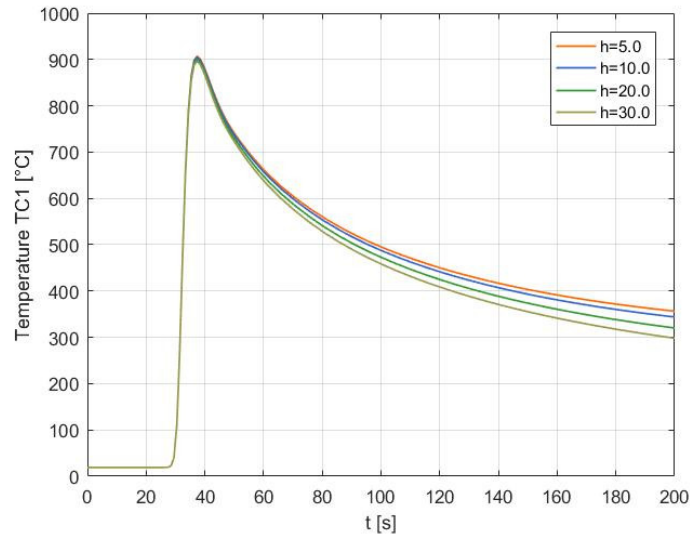
Figure 64: Time-temperature profiles for different values of the convective heat transfer coefficient

In contrast to radiation losses, the impact on peak temperatures and fusion zone dimensions (Figure 65) is not as distinctive. The temperature profiles initially show a similar gradient and only start to fan out towards lower temperatures depending on the value of the coefficient. Thus, the convection heat transfer is more dominant in the lower temperature regions away from the weld.
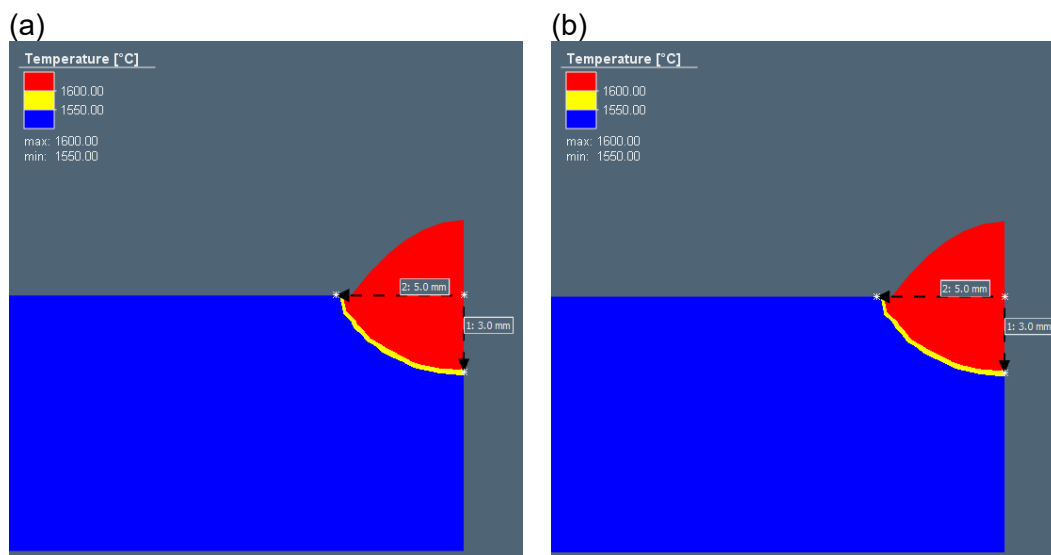

Figure 65: Molten pool dimensions for different values of h: a) $h = 5.0 \frac{W}{m^2 K}$*; b)* $h = 30.0 \frac{W}{m^2 K}$

C.4 Contact heat transfer coefficient

Finally, the behaviour of the contact heat transfer coefficient is studied. Contact heat transfer depends on the surface quality, material pairings and pressure. Thermal input parameters for the numerical simulation can be seen in Table 30.

Table 30: Parameter variation of the contact heat transfer coefficient

Parameters		V1	V2	V3	V4
Thermal efficiency	η	0.4	0.4	0.4	0.4
Coefficient of radiation	ε	0	0	0	0
Convective heat transfer coefficient	h	0	0	0	0
Contact heat transfer coefficient	a	10.0	100.0	200.0	1000.0

The contact heat transfer is used to calculate the heat flux from the baseplate to the backing plate. Graf et al. [61] has modelled the thermal face flux condition with 100 W/(m²·K) for magnesium AZ31 and 2000 W/(m²·K) for steel G4Si. Figure 66 shows the time-temperature profiles obtained for different values of the contact heat transfer coefficient.
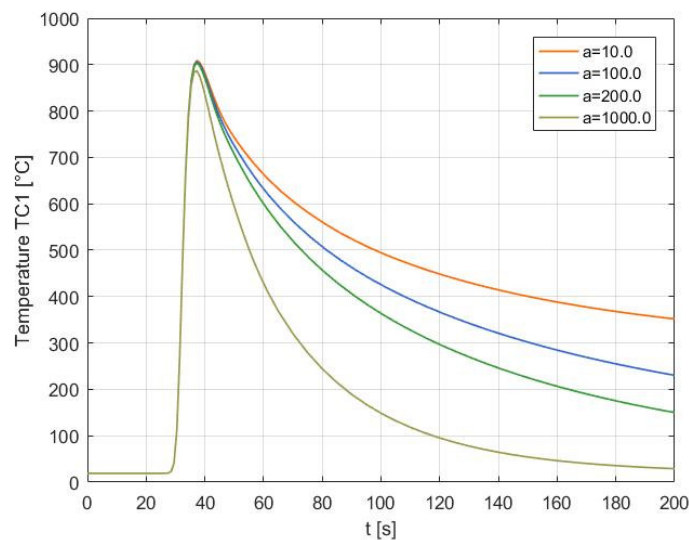

Figure 66: Time-temperature profiles for different values of the contact heat transfer coefficient

Values of the contact heat transfer coefficient up to 200 W/(m²·K) do not influence the peak temperatures significantly and fan out towards cooler temperatures. A heat transfer coefficient of 1000 W/(m²·K) shifts the peak temperature to lower temperatures and shows steep temperature gradients until the component reaches ambient temperature. The contact heat transfer also strongly depends on the contact area of the components in contact. The impact of the heat transfer coefficient on the molten pool dimensions is negligible, as shown in Figure 67.
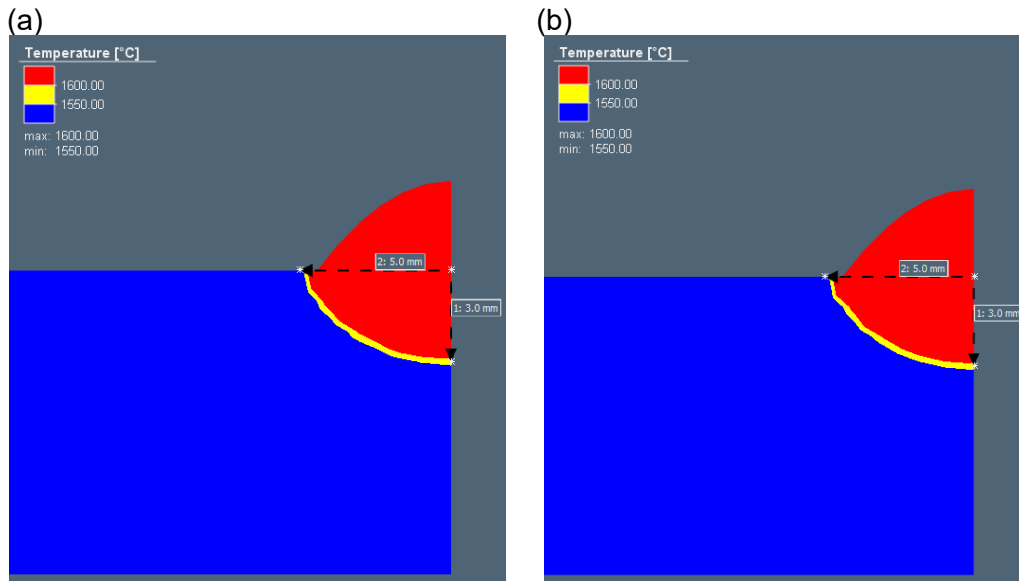
(a)

(b)

Figure 67: Molten pool dimensions for different values of h: a) $a = 10.0 \frac{W}{m^2 K}$; *b)* $a = 1000.0 \frac{W}{m^2 K}$

Appendix D – Mechanical boundary conditions

Clamps are essential components during the plasma metal deposition process restricting the workpiece to distort and keeping it in position within the working space. In the simulation framework within Simufact Welding clamps can be defined and applied as boundary conditions to the workpiece. Clamps work as springs and can directly apply a force opposite to a movement normal to the surface, thus directly responding to the welded structure. The implementation of a clamp in the simulation tool requires mechanical properties of the clamp depending on its type of definition. In this study the clamping movement was controlled via "Stiffness & force". The definition requires a translational and/or a rotational stiffness and additionally an initial force additionally. The estimation of these two parameters is briefly explained in the following paragraphs.

D.1 Clamp stiffness

A linear elastic analysis using Abaqus CAE 6.14 is performed to estimate the spring stiffness of the clamp. The clamp consists of two parts, a steel step block and a steel step clamp. The clamp is loaded with an arbitrary constant force of 2,500 N acting on the negative of the surface that actually presses on the baseplate of the experimental setup described in chapter 4. The model is constrained by fixing all degrees of freedom of the bottom surface of the step block. The step block (master) and step clamp (slave) are connected using a surface-to-surface tie constraint. The implementation of an interaction property in Abaqus requires the definition of a slave and master surface. A drawing of the model can be seen in Figure 68.
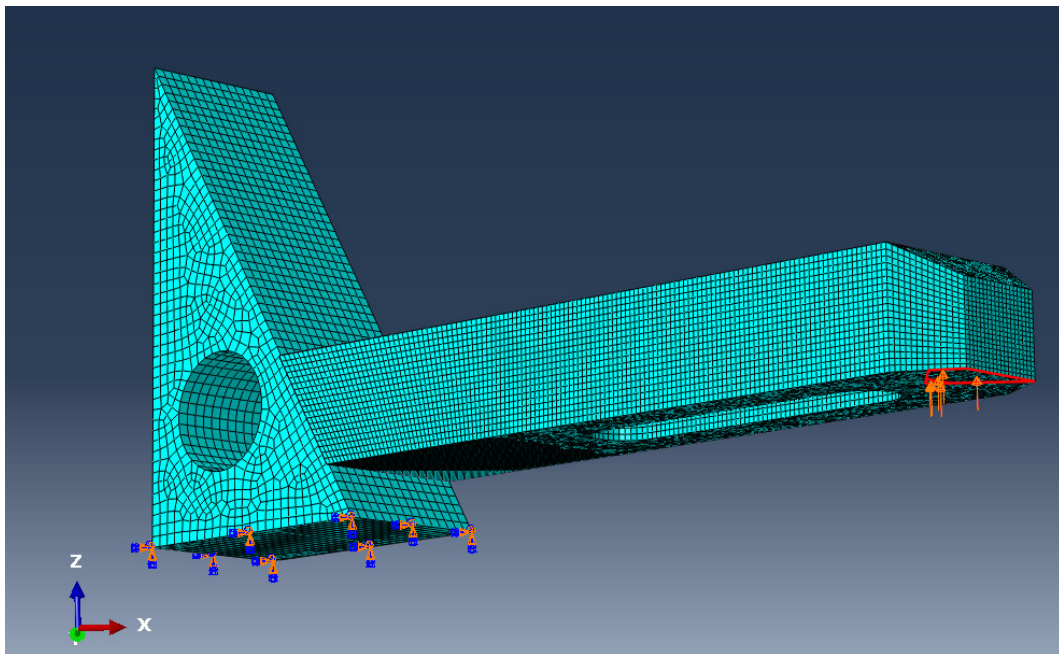

Figure 68: Meshed CAD model of the clamp assembly

Table 31 shows the material data used in the finite element analysis. Isotropic material behaviour was specified.

87

Table 31: Material data used in the finite element analysis

Material	E [MPa]	ν [-]
Steel C45	210,000	0.28

A finite element mesh with a total number of 94,520 nodes and a total number of 83,914 linear hexahedral elements of type C3D8R is used. The clamp is meshed with a global element size of 1 mm, the block with a global element size of 2 mm. After the finite element model is solved, the average deflection of the whole surface marked in red in Figure 68 is determined. The deflection is set in relation with the force applied (Figure 69). The slope of the linear curve yields the translational spring stiffness of the clamp. The data points in between result from incremental application of the load.
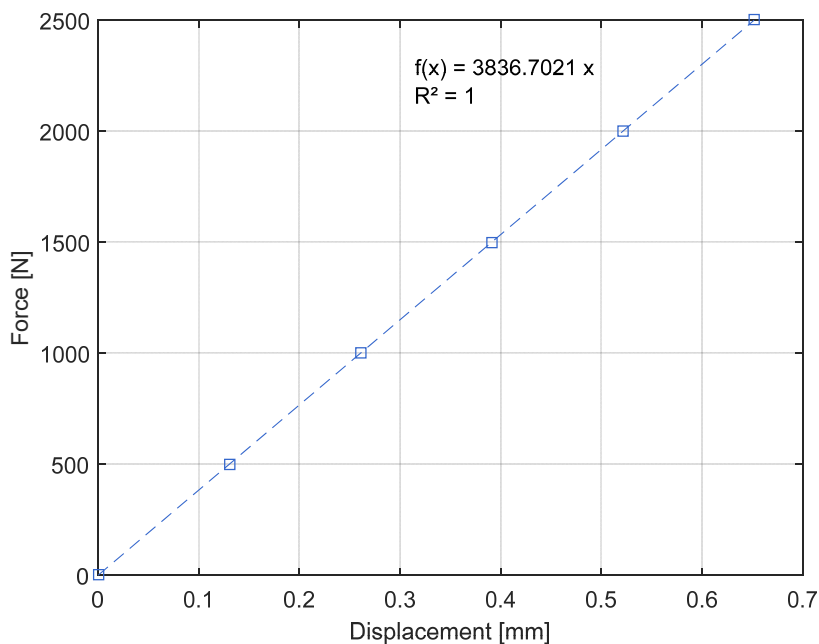

Figure 69: Force-Displacement relation of the clamp

To impose a mechanical boundary condition the real clamping system is simplified, whereby the clamp is replaced by a spring with a corresponding spring stiffness. The spring stiffness is set to a constant value of 3,837 N/mm.

D.2 Contact Force

Another analysis using Abaqus CAE 6.14 is performed to estimate the contact pressure of the clamp on the baseplate. The model consisted of six parts, an aluminum backing plate, a titanium baseplate, a steel stud, a steel hexagonal flange nut, a steel step block and a steel step clamp. As outlined in chapter 4, the baseplates are fixed to the backing plate of the welding chamber by using clamps placed at specified positions. The steel bolts are pre-tensioned with a torque of 80 Nm. This pretension is a critical parameter for the following simulation. In Abaqus the pretension can be defined as an applied force or a length. In this study, the pretension is adjusted over the length which is determined as the following: firstly, the flange nut is tightened manually until it makes contact with the clamp and, secondly, a torque wrench is used to apply a torque of 80 Nm, whereas the number of turns of the nut is

counted. After about 5/8 turns the required torque is reached. The thread pitch which is 1.75 mm in the case of a M12 metric thread, multiplied by the number of turns is used as a satisfactory approximation to calculate the preload length of the screw. The stud is hence pre-tensioned with a length of 1.09 mm. The model is constrained by fixing all degrees of freedom of the bottom surface of the backing plate and symmetry boundary conditions on the cut surfaces. A drawing of the model can be seen in Figure 70.
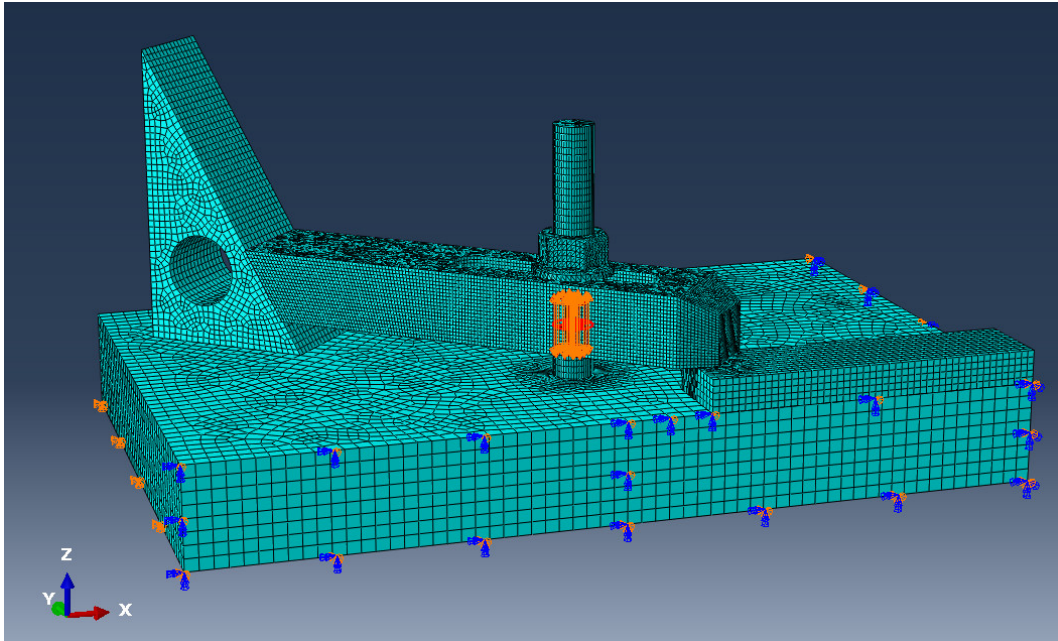

Figure 70: Meshed CAD model of the contact force assembly

Table 32 shows the material data used in the finite element analysis. Isotropic material behaviour was specified.

Table 32: Material data used in the finite element analysis

Material	E [MPa]	ν [-]
Steel C45	210,000	0.28
Ti-6Al-4V	104,800.31	0.31
Al 6061	69,000	0.33

In Table 33 all surface-to-surface interactions between the instances of the FEM model are shown. To reduce computational costs and time, friction is only considered in the contact area of the clamp with the baseplate. All other interactions are modelled using a tie constraint.

Table 33: Surface-to-surface interactions

Master	Slave	Type
Hex flange nut	Steel stud	Tie
Backing plate	Steel stud	Tie
Hex flange nut	Step clamp	Tie
Step block	Step clamp	Tie
Backing plate	Step block	Tie
Backing plate	Baseplate	Tie
Step clamp	Baseplate	Contact

The contact property is defined using normal behaviour and tangential behaviour. The normal behaviour is set to "Hard Contact". Since no static coefficient of friction for dry conditions is found for the material pairing steel-titanium, the tangential contact behaviour is defined in a first step as frictionless. Then a value of 0.20 is applied which is a typical value for steel/steel dry contact [63]. At last, the friction coefficient is set to 0.36 which corresponds to a Ti-6Al-4V/Ti-6Al-4V contact pair [64].

A finite element mesh with a total number of 179,399 nodes and a total number of 157,700 elements (144,745 linear hexahedral elements of type C3D8R, 5,284 linear wedge elements of type C3D6 and 7,671 quadratic tetrahedral elements of type C3D10) is used. After the finite element model is solved, the average contact pressure at the baseplate of the surface in contact with the step clamp is determined. The average contact pressure is multiplied by the area of the surface to get the initial force applied on the baseplate.

Table 34: Contact force estimation

Friction-coefficient [-]	Mean contact pressure [MPa]	Contact surface area [mm²]	Mean contact force [kN]
frictionless	435.764	159.515	69.511
$\mu = 0.20$	424.001	159.515	67.635
$\mu = 0.36$	413.601	159.515	65.976

Table 34 shows the difference between frictionless and frictional contact. Since the baseplates have been machined prior to the PMD process and therefore have a good surface quality, the friction coefficient of 0.20 is used to calculate the contact force.

The definition of a clamping boundary condition in Simufact Welding is now complete. The clamping movement can be controlled by "Stiffness & Force" with a constant stiffness of 3,837 N/mm and a constant contact force of 67,635 kN.